Cryo-Electron Microscopy Studies of Dynamical Features of Ribosomes during the Translation Process

Ming Sun

Submitted in partial fulfillment of the
requirements for the degree of
Doctor of Philosophy
in the Graduate School of Arts and Sciences

COLUMBIA UNIVERSITY

2016

ABSTRACT

Cryo-Electron Microscopy Studies of Dynamical Features of Ribosomes during the Translation Process

Ming Sun

Cryo-electron microscopy (cryo-EM) is a structural biology technique that determines the structure of proteins and macromolecular complexes using the transmission electron microscope under cryogenic conditions. In my Ph.D. studies, I took advantage of this technique, in the study of dynamical features of ribosomes in both eukaryotes and prokaryotes.

In **Chapter 2**, I report my graduate research on the investigation of ribosomes from the human malaria parasite, *Plasmodium falciparum*, using single-particle cryo-EM. In collaboration with Dr. Jeffrey Dvorin at Harvard Medical School, we obtained five cryo-EM reconstructions of ribosomes purified from *P. falciparum* blood-stage schizonts, and discovered structural and dynamical features that differentiate the ribosomes of *P. falciparum* from those of the mammalian system. Moreover, we discovered that RACK1, a necessary ribosomal protein in eukaryotes, does not specifically co-purify with the 80S fraction in the *P. falciparum* schizonts stage and would mainly function in a ribosome-unbound, free state during the blood-stage. More extensive studies, using cryo-EM methodology, of translation in the parasite, will provide structural knowledge that could help in the design of effective anti-malaria drugs.

In **Chapter 3**, I describe the cryo-EM studies of the *Saccharomyces cerevisiae* ribosome in response to a carbon source switch. In collaboration with Dr. Andrew Link at Vanderbilt

University, we obtained reconstructions of the 80S ribosomes at selected time points after the glucose-to-glycerol carbon source shift, and observed that a fraction of ribosomes lacked densities for r-proteins, mainly eS1 (yeast rpS1) on the 40S subunit and uL16 (yeast rpL10) on the 60S subunit. We found that the binding ratio of eS1 and uL16 to ribosomes changed as a function of time, consistent with the change in translational activities as gauged by polysome profiling. On the basis of these observations, along with previous structural and genetics studies, we propose that rapid control of translation is exerted through the dissociation of r-protein eS1/rpS1 and uL16/rpL10 from the ribosome. Our studies thus open a new venue on the exploration of *S. cerevisiae*'s rapid adaption to carbon source shifts at the level of translation.

In **Chapter 4**, I have documented a collaborative work on the development and application of a new technique, time-resolved cryo-EM, which can be used to study processes involving two reaction partners on a sub-second time scale. With my colleagues at the Frank and Gonzalez labs at Columbia University, we successfully applied this method to study the process of *E. coli* ribosomal subunits association. By mixing and reacting the two subunits for 60 ms and 140 ms, we captured the association reaction in a pre-equilibrium state, and detected different conformations of *E. coli* 70S ribosomes. With the current capability of this mixing-spraying method to visualize multiple states of molecules in a sub-second reaction, we expect to be able to standardize this method and apply it to more challenging biological processes, such as translation recycling and initiation processes.

TABLE OF CONTENTS

List of Figures

List of Tables

List of abbreviations and acronyms

Å	Angstrom, 1 A = 10^{-10} M
A Site	Aminoacyl-tRNA Binding Site
aa	Amino Acid
aa-tRNA	Aminoacyl-tRNA
ASL	Anticodon Stem-Loop of tRNA
CC	Cross-Correlation
CCD	Charge-Coupled Device
CMOS	Complementary Metal-Oxide Semiconductor
Cryo-EM	Cryogenic Electron Microscopy
CTF	Contrast Transfer Function
Da	Dalton
DDD	Direct Detector Device
E Site	tRNA Exit Site
FEG	Field Emission Gun
fMet-tRNA^{fMet}	N-formylmethionyl Initiator tRNA^{fMet}
FRET	Fluorescence Resonance Energy Transfer
FSC	Fourier Shell Correlation
GAC	GTPase-Associated Center
GDP	Guanosine Diphosphate
GMP-PNP	Guanylyl Iminodiphosphate
GTP	Guanosine Triphosphate

H (In H69 etc.)	Ribosomal RNA Helix
HEPES	4-(2-Hydroxyethyl)-1-Piperazineethanesulfonic Acid
IC	Initiation Complex
IF	Initiation Factor
MAP	*Maximum a Posteriori*
ML	Maximum-Likelihood
mRNA	Messenger RNA
ms	Millisecond
NMR	Nuclear Magnetic Resonance
OD	Optical Density
P Site	Peptidyl- tRNA Binding Site
PDB	Protein Data Bank
POST-state	Post translocational state
PRE-state	Pre translocational state
PSF	Point Spread Function
Psi	Pounds Per Square Inch, 1 Psi = 6,895 Pascal
PTC	Peptidyl-Transferase Center
RELION	REgularized LikeLihood OptimizatioN
RNA	Ribonucleic Acid
r-Protein	Ribosomal Protein
rRNA	Ribosomal RNA
smFRET	Single-Molecule Fluorescence Resonance Energy Transfer
SNR	Signal-To-Noise Ratio

SPIDER	System for Processing of Image Data from Electron Microscopy and Related Fields
Tris	2-Amino-2-Hydroxymethyl-Propane-1,3-Diol
tRNA	Transfer RNA

Acknowledgements

This thesis would not have been accomplished without the support and encouragement of a large number of people. First and foremost, I would like to express my sincere thanks to Dr. Joachim Frank, my graduate advisor, for his guidance and mentorship throughout my years at Columbia University. He is a true scientist and always strives for the best. It has been a great privilege to work with him for the past years. I would also like to thank my undergraduate research advisors, Dr. Ning Gao, Dr. Jianlin Lei and Dr. Haixiao Gao. They led me into the field of cryo-EM and are instrumental in my progression at Columbia University.

I would also like to express my deep gratitude to all my committee members: Dr. Ruben L. Gonzalez, Dr. Wayne Hendrickson, Dr. Bridget Carragher and Dr. Jeffrey D. Dvorin, for their valuable instruction and continuing support throughout my Ph.D. studies.

For support in science and beyond, I would like to thank my coworkers on various projects. Karin Blomqvist at Dvorin's lab gave me strong support on the *Plasmodium* project. She has been a great collaborator and a great friend! Oliver Clarke at Hendrickson's lab spent so much time discussing latest improvements in the field of cryo-EM and X-ray crystallography. Parimal Samir and Chris Browne at Link's lab provided their insightful comments on the project of yeast ribosomes' adaption to the carbon source switch. Jia Wei at Tong's lab gave me guidance on *T. cruzi* model building and refinement. Kelvin Caban at Gonzalez's lab provided support on the series of time-resolved projects. Xiangsong Feng at Lin's lab taught me about mixing-spraying chip design. Robert Washburn, and Shivalika Saxena in the Gottesman lab helped me with my rotation project, transcription and translation coupling event.

For a wonderful environment, I thank all the current and former members of the Frank lab. Specifically, I would like thank Wen Li, for her great patience for all my questions and the many helpful suggestions on my science work. I would also like to thank Robert Grassucci, Yaser Hashem, Amedee des Georges, Bingxin Shen, Bo Chen, Harry Kao, Robert Langlois, Marcus Fislage, Sandip Kaledhonkar, Ziao Fu, Zheng Liu, Hstau Liao, Masgan Saidi, Cheri Hampton, Drew Kennedy, Melissa Thomas-Baum, Sanchaita Das, Gyanesh Sharma, Nadia Severina, Amy Jobe, Danny Nam Ho, and Nima Yousefi, for their great help over the past years.

On a more personal note, I would like to thank my best friends Chang Liu, Ju Yang and Xinying Liu, with whom I have shared all the ups and downs throughout my graduate career. I would like to thank all the people from whom I received tremendous help at one time or another during my graduate career. I would like to particularly thank my outside great “mentors”, Yifan Cheng, Maofu Liao, Xueming Li, Sjors Scheres and Xiaochen Bai. Your inspiration and passion for science have had a great impact on my career selection. And I must thank my friends, Juan Du, Chia-Hsueh Lee, Yu-rui Wang, Yanxin Liu, Qiang Guo, Boya Feng, Yixiao Zhang, Shuaiyi Liang and Mao Mao, for your help and support.

Last but not least, I would like to thank my parents. I am more grateful than I can express for their enduring love and encouragement. And I am so proud to dedicate this thesis to my mother and my late father.

To My Mother, Weilin Wan,

And

My Father, Yan Yin (1958 – 2012)

Chapter 1 Single-particle cryo-electron microscopy

Cryogenic electron microscopy (cryo-EM) and single-particle reconstruction is the ideal approach for studying flexible and functionally active macromolecules. Its development has taken place over the past five decades and it has recently undergone a leap in its achievable resolution and its applicability to challenging biological systems. Table 1.1 summarizes a number of key landmarks in the development of cryo-EM.

In this chapter, I outline some principles of single particle cryo-EM analysis, and the epochal changes that occurred during my work toward my Ph.D. thesis.

Year	Key Authors and Publications	Landmarks
1968	De Rosier and Klug (1)	The first 3D reconstruction of the bacteriophage T4 tail
1975	Unwin and Henderson (2)	Visualization of glucose-embedded 2D crystals of bacteriorhodopsin
1976	Taylor and Glaeser (3)	First demonstration that high-resolution structure information of biological samples could be obtained under cryogenic conditions
1981	Frank *et al* (4)	A demonstration of 2D averaging applying the newly minted SPIDER software on images of 40S ribosomal subunits
1981	Van Heel and Frank (5)	Multivariate statistical analysis and classification of aligned images
1982	Dubochet *et al* (6)	Sample vitrification method
1987	Radermacher, Frank *et al* (7)	Single particle – random conical tilt method

1990	Henderson *et al* (8)	The first atomic structure using electron crystallography method
1994	Penczek, Frank *et al* (9)	Single particle – projection matching method
1995	Berriman and Unwin (10)	Time-resolved cryo-EM method applied to the study of acetylcholine receptor
1995	Frank *et al* (11)	25Å cryo-EM structure of the 70S ribosome
1997	Bottcher, Crowther *et al* (12)	<10Å cryo-EM structure of Hepatitis B virus, breaking the 10Å barrier
1998	Sigworth (13)	2D maximum-likelihood method
2005	Gonen, Walz, Harrison *et al.* (14)	1.9Å cryo-EM structure of aquaporin (AQPO), using 2D electron crystallography method
2007	Scheres *et al* (15)	3D maximum likelihood method
2008	Zhou Group (16)	The first atomic structure of a cytoplasmic polyhedrosis virus
2012	Brilot, Campbell, Grigorieff *et al* (17,18)	Direct electron detection cameras used for motion correction
2013	Bai, Scheres *et al* (19-21)	RELION; Near-atomic maps of 30K ribosome particles
2013	Liao, Cao, Yifan *et al* (22)	First near-atomic resolution membrane protein structure determined by single particle cryo-EM
2015	Bai, Scheres *et al* (23)	De novo tracing <200kDa molecules
2015	Campbell, Carragher, Potter *et al* (24)	Breaking 3Å barrier, 2.8Å cryo-EM reconstruction of 20S proteasome
2016	Subramaniam Group (25)	1.8Å resolution cryo-EM reconstruction of a 334 kDa glutamate dehydrogenase; 3.8 Å resolution cryo-EM reconstruction of a 93kDa isocitrate dehydrogenase

Table 1.1 Key landmarks in the evolution of cryo-EM in the past decades.

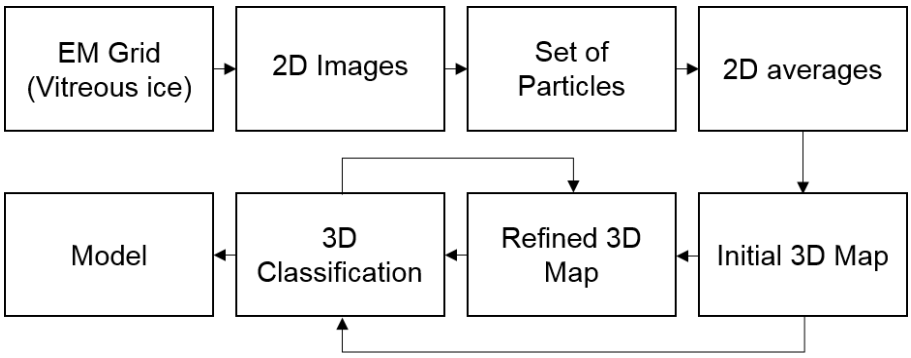

Figure 1.1 General steps involved in structure determination by single-particle cryo-EM. A single-particle cryo-EM project usually starts from sample purification and cryo-EM grid preparation (Section 1.1). 2D images are acquired using transmission electron microscopes (Section 1.2), usually equipped with cryo-holder and digital detectors. Particles are extracted, aligned and averaged for subsequent imaging processing (Section 1.3). An initial 3D map is first constructed. This map will then be iteratively refined and validated using image processing software. Due to the inherent heterogeneity of biological samples, computational algorithms such as regularized likelihood optimization, or so called *maximum a posteriori* (MAP) estimation implemented in RELION, are used to classify heterogeneous data sets into structurally homogeneous subsets for further refinement and interpretation (Section 1.3 and 1.4).

1.1. Specimen preparation for single-particle cryo-EM

For detailed procedures of specimen preparation, please see the "Materials and Methods" sections in Chapters 2, 3 and 4. For an in-depth review of general cryo-EM sample preparation the reader is referred to (26-29). Following is a general introduction to single particle cryo-EM specimen preparation.

A single-particle cryo-EM experiment begins with a purified specimen, which is usually in aqueous solution at a concentration of 0.5nmol/L to 2 μmol/L The solution is applied to an EM grid, typically consisting of perforated carbon film supported by a metal frame, and blotted with filter paper to remove the excess solution. The grid will then be immediately plunged into liquid ethane (-180°C) cooled by liquid nitrogen (-196°C) (26). The rapid freezing step traps biological molecules in their native, hydrated state without dehydration or ice crystallization and the cryogenic temperature greatly slows the effects of radiation damage sustained in the TEM.

A perfectly vitrified specimen is characterized by an amorphous ice layer of sufficient thickness to accommodate the particles (but ideally not much thicker so that particles are clearly visible), and particles that are well distributed across the field of view and adopt a wide range of orientations. In practice, several parameters often require optimization to achieve these conditions.

One consideration in the specimen preparation is the supporting structure of the EM grids. The most commonly used is a copper grid, covered by either a continuous carbon film, typically used to prepare negatively stained samples, or holey carbon film, typically used to prepare vitrified specimens. Holey carbon grids can be either home-made, with irregular holes, or nanofabricated with regularly arranged holes (e.g. Quantifoil grids from Quantifoil Micro Tools GmbH, and C-flat grids from Protochips Inc): the latter are particularly suitable for automated EM data collection. Recently, alternative grid designs have been explored, such as replacing carbon film with graphene (30,31), and replacing both grid support and carbon film with a single material, gold (32,33).

Another important practical issue in specimen preparation is obtaining a very thin, evenly distributed ice layer. A thin ice layer will result in high contrast between the molecule and the surrounding ice layer, and minimized defocus spread arising from different heights of the molecules in the ice layer, which hamper the determination of high-resolution structures. The two

key parameters that affect ice thickness are blotting time and the subsequent time the grid is allowed to dry before it is plunge-frozen. Although these parameters can be controlled with commercially available plungers, such as Vitrobot (FEI) and Cryo-plunge (Gatan), the user's heuristic optimization is necessary and essential. Other factors that affect ice thickness are the type of sample support structure, the particular batch of grids, and the hydrophilicity of the support film.

1.2. Data collection for single-particle cryo-EM

1.2.1. Image formation in the transmission electron microscope

For in-depth details of the principle and theory of scattering and image formation, and the many applications of the transmission electron microscope, please see (34,35) and (36). The following will make reference to a schematic diagram of a typical transmission electron to explain the essential elements, and the relevant practical issues (Figure 1.2).

Cryo-electron microscopy (cryo-EM) is a form of transmission electron microscopy (TEM) where the sample is studied at cryogenic temperatures (generally liquid nitrogen temperature). A typical TEM has several essential components, including an electron source, a series of electromagnetic lenses and an image detecting system. Electrons have the properties of tiny mass, negative charge and capability of being manipulated by a magnetic field. Electrons in electron microscopy have a very short wavelength, about 0.025 Å at 200 kV and 0.0197 Å at 300 kV. However, the imperfections of electromagnetic lenses (see details following paragraphs) prevent resolution from reaching these theoretical limits.

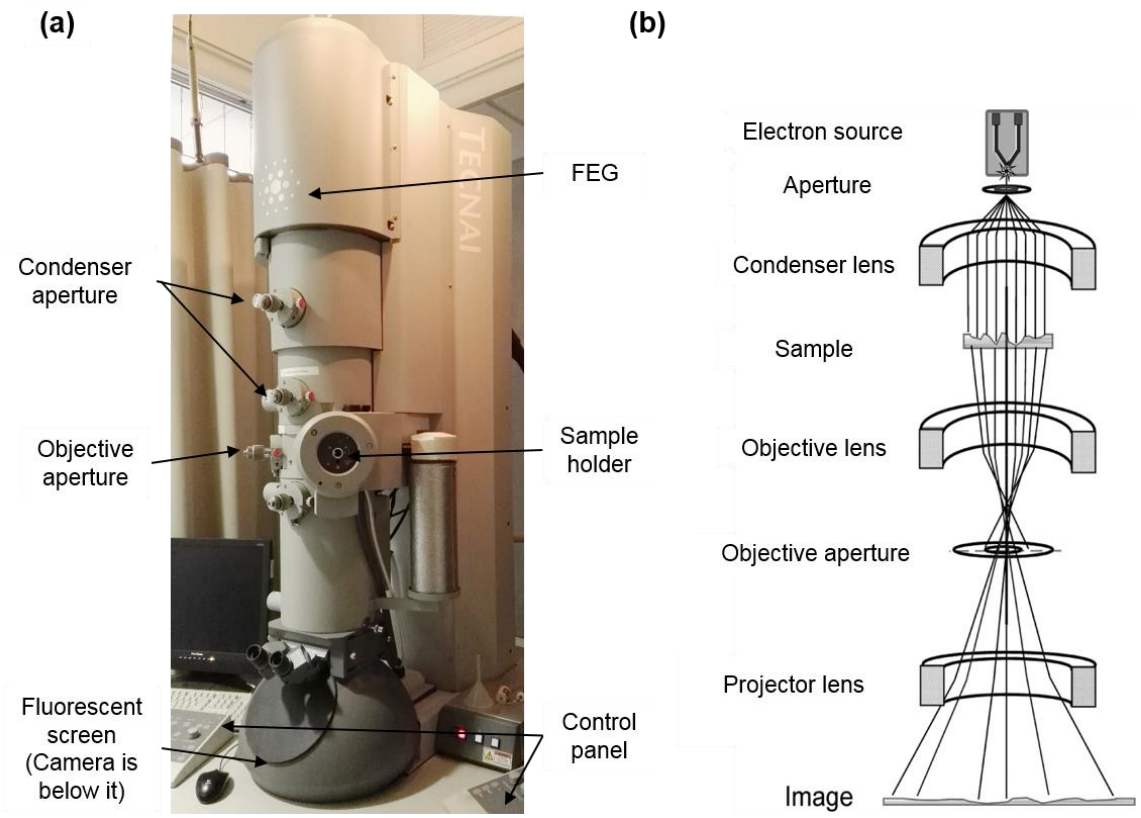

Figure 1.2 A transmission electron microscope (TEM). (**a**) Photograph of the TEM, FEI TF20 in the Frank lab. (**b**) Image formation in the TEM. (b) was adapted from (37).

The ***electron sources*** available include the heated tungsten filament, the LaB_6 crystal, and field emission gun (FEG). The FEG, by far the most advanced and widely used electron source, emits coherent, near-monochromatic and high-current density electrons. As in light microscopy, the typical electromagnetic lens system is mainly composed of condenser, objective, intermediate and projector lenses. The ***condenser lenses*** determine the size reduction of the electron source onto the specimen and how strongly the beam is focused onto the specimen and with what convergence angle of the beam. The ***condenser lens apertures***, situated below the condenser lens, remove electrons with a large angular spread from the beam and thus improve beam coherence.

The ***objective lens*** forms the initial image and determines the quality of the image. Variation in the field strength is the primary means of adjusting focus of the image on the viewing screen. The ***objective lens aperture,*** the first aperture situated below the specimen plane, is used to increase contrast of the image, because is excludes widely scattered electrons. The ***intermediate and projector lens*** system is used to further magnify the image before the electrons arrive at the detector (27,35). In practice, we can change the spot size, indexed from 1 to 11 in FEI microscopes, to adjust beam intensity falling on the specimen and thus the overall brightness of the image. Typically, we collect data at spot sizes 5 or 6. By adjusting the "focus knob", we can change the objective lens current, and thus set the targeted focus values.

Problems with electromagnetic lenses. There are many defects of electromagnetic lenses, but here we focus on those that limit microscope performance in substantial ways. These are spherical, chromatic, and astigmatic aberrations. ***Spherical aberration*** is the type of aberration that is most significant in defining the performance of the objective lens. It is an image distortion due to the dependence of the focal length on the distance of the ray from the optical axis. The further off-axis the electron beam is, the more strongly it is bent back toward the axis. As a consequence, the image of a point becomes a blurred disk. This aberration can be partially compensated by operating the lens in underfocus. ***Chromatic aberration*** becomes important when electrons vary in energy. Electrons that have longer wavelength will be focused more strongly by the lens, so that part of the image is formed in a plane closer to the object. ***Axial astigmatism*** can be understood as an "unroundness" of the lens, which results in the image of a point becoming the shape of an ellipse. Fortunately, axial astigmatism can be compensated with special corrector elements that are situated under the objective lens.

Image formation in the electron microscope. The basis of image formation in the electron microscope is the interaction of electrons with the object. Electrons may either pass through the specimen unimpeded, be scattered without loss of energy (elastic scattering), or be scattered with an exchange of energy between the electron beam and the specimen (inelastic scattering). Elastically scattered electrons contribute to the image intensity, through the mechanism of phase contrast.

Biological samples consist of light atoms, H, O, N and C and can be described as weak phase objects. According to the weak-phase object approximation (38), the contrast of an image of the biological sample is approximately proportional to the projected object potential. Considering imperfections of the lens, the relationship between the Fourier transform of the image contrast $I(\mathbf{k})$ and the Fourier transform of the object's projection $O(\mathbf{k})$ can be described by a function $H(\mathbf{k})$, known as contrast transfer function (CTF).

$$I(k) = O(k)H(k)$$

The function $H(k)$ is represented by the product of two terms, $A(k)\ \sin\gamma(k)$. $A(k)$ is the aperture stop function. $\gamma(k)$ is the wave aberration function, where spherical aberration, wave length (defined by accelerating voltage) and defocus value are the major contributors. In practice, the CTF function $H(k)$ is modified by an envelope function $E(\mathbf{k})$, which results from the partial coherence of the illumination and the energy spread of the electrons. Because of the characteristics of the CTF, namely the phase-flip and crossovers at certain spatial frequencies, a correction of the CTF is needed in reconstruction procedures.

1.2.2. Image recording and acquisition

The three main detector technologies used in cryo-EM are photographic films, charge-coupled devices (CCD) and direct detector devices (DDD). ***Photographic film*** is a strip or sheet of transparent film base coated with photographic emulsion containing microscopically small light-sensitive silver halide crystals. It has the advantages of fine pixels and large image detection area, and has been used over many years in EM. However, the data are not immediately available to the users due to the need for a number of steps, development in the darkroom and digitization of optical densities by a scanner.

The ***Charge-coupled device (CCD)*** contains a scintillator, fiber optics, and a photo sensor. "Charge-coupled" refers to the readout mechanism, in which charges are transferred between neighboring pixels to a readout register, and then amplified and converted to a digital signal (39). Compared with conventional photographic films, the CCD camera has the advantage of real-time readout, linear response, large dynamic range, and the capability of automated data collection. However, the problem with the CCD camera is that its signal is the result of two conversions, electron to photon, then photon to electron, and the spatial resolution is reduced as light undergoes from multiple scattering within the phosphor or at the optical interface.

Consequently, detectors are needed based on more direct detection, thus avoiding the intermediate light conversion step required for CCDs. A Direct Detection Device (DDD) can be directly exposed to the high energy electron beam, and converts the electrons into voltage signals, rather than producing a signal proportional to the accumulated charges (Figure 1.3). Moreover, in combination with CMOS (complementary metal-oxide-semiconductor) design, these DDDs convert charges to voltage signals locally, resulting in a faster read-out speed. The first commercially available CMOS-based DDD camera for cryo-EM single particle application was

the DE-12 camera from Direct Electron, LP (San Diego, CA) (40,41). The other two popular commercially available DDD are the K2 Summit™ from Gatan, Inc. (Pleasanton, CA), and Falcon camera from FEI (Hillsboro, OR). Please see section 1.4.1 for more details of DDD cameras and their application in single particle cryo-EM.

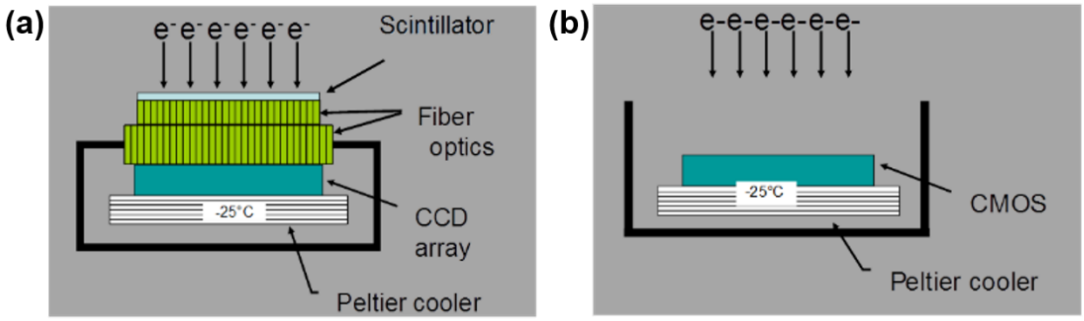

Figure 1.3 Schematic representation of a CCD detector and a CMOS-based DDD detector for EM. **(a)** CCD: multiple conversion steps. Fiber optics transmit the image to the CCD sensor where photons generate electrical charge, and the charge is accumulated in parallel registers. **(b)** CMOS-based DDD: direct conversion. High-energy electrons are directly counted and converted to voltage signals. (Figures were adopted from FEI datasheets).

1.3. Single-particle 3D reconstruction

In the single-particle 3D reconstruction method, the 3D electron density map of the molecule is computed from a set of single-particle images, representing projections of molecules lying in different orientations. The main steps include CTF estimation and correction, particle picking and selection, two-dimensional alignment and averaging, initial three-dimensional reconstruction and refinement of the reconstructed density map.

1.3.1. CTF estimation and correction

In section 1.2.1, we have seen that the observed image is not a faithful representation of the original structures. It is degraded by the effects of the CTF. An accurate determination and correction of the CTF is a critical requirement in determination of high-resolution cryo-EM structures.

The CTF models the linear image formation process in the transmission electron microscope. The key parameters that are required for CTF estimation are acceleration voltage, spherical aberration constant, defocus, amount and direction of axial astigmatism, and percentage of amplitude contrast. Acceleration voltage and spherical aberration coefficient are instrument parameters, and the percentage of amplitude contrast is empirically estimated, typically assumed as 5% –10% for cryo-EM images (27). The defocus value is set to a nominal value during data collection. However, this setting is only approximate. More accurate values for defocus and astigmatism are obtained by subsequent measurements. CTF determination involves using a least-squared fitting method, to find the set of parameters that minimize the discrepancy between the calculated CTF model and the observed radially averaged power spectrum.

Several software packages capable of CTF correction are currently available, for instance, SPIDER (42), EMAN (43), CTFFIND3 (44), CTFFIND4 (45) and GCTF (46). In our studies, we used CTFFIND3 software (44) for CTF estimation and correction. CTFFIND3 is a fully automated software that showed the best results using real datasets in a recent benchmark competition (47). It determines both defocus and astigmatism values in untilted images with high accuracy. The general workflow of CTTFIND is (1) computing an amplitude spectrum from the input micrograph, (2) estimating and subtracting the background from the original spectrum, (3) evaluating the correlation between the calculated two-dimensional CTF functions and the background-subtracted

power spectrum, and (4) adjusting the parameters for the theoretical CTF until the cross-correlation is maximized, thus yielding an estimate of the microscope's defocus and astigmatism parameters. For more details the reader is referred to (44).

1.3.2. Particle picking and selection

Once data have been collected and good micrographs have been selected, particles representing the true biological molecules need to be selected and extracted for the subsequent image analysis. The particle selection problem can be broken down into two main steps, (1) candidate particles are selected from micrographs, which will include false selected particles, e.g. contaminants, ice blobs or noise, and (2) 'good' particles, representing true biological molecules, are identified from candidate particles.

Many automated or semi-automated particle picking software packages are currently available, including EMAN2 (48), SIGNATURE (49), DOGPICKER (50), XMIPP (51), ARACHNID (52) and RELION (53). Based on the underlying algorithms, these approaches can be broadly divided into two groups: reference-based and reference-free. In the reference-based approach, the reference can come from projections of a known 3D structure of the complex or the class average of particles selected from micrographs (49,54,55). In the reference-free approach, different characteristics (e.g. edges, shapes) of the particles are expressed in some numerical manner as a vector (feature), and features calculated from local areas in the micrographs are compared to a set of expected features.

In our cryo-EM studies of eukaryotic (Chapter 2 and 3) and prokaryotic ribosomes (Chapter 4), we used an in-house built particle-picking program called AutoPicker developed in the Frank lab (52). The AutoPicker algorithm uses a modified reference-based procedure to identify windows

that contain candidate particle images in a micrograph, and an unsupervised machine learning procedure to reject high contrast contamination and noise. The template is usually a disk with a radius corresponding to the particle size and its edge is softened with a Gaussian (52). Besides our ribosomes studies, AutoPicker has been employed in other studies resulting in publication-quality density maps, such as *T. thermophiles* V/A-ATPase (52), 70S *E. coli* ribosomes (52), 43S preinitiation complex bound to the DHX29 protein and 40S ribosomal complex containing eIF3 and the CSFV IRES (56,57).

1.3.3. Two-dimensional clustering and averaging

Two-dimensional clustering and averaging is performed for the following reasons: (1) It can eliminate artifacts or invalid particles from the above particle picking and extraction step; (2) It presents a fast way of quantitatively measuring data quality, such as the angular distribution of particle views, and estimating the potential resolution; (3) It provides high signal-to-noise-ratio (SNR) class averages, which can be scrutinized for quality before moving on to the subsequent 3D structure determination.

Various strategies are available for 2D alignment and clustering. Supervised methods group data sets according to the degree of their similarity to a reference, and are primarily used for the case of homogenous data sets. Unsupervised methods, in contrast, do not require a reference and can find any groups of images that may have a common origin. (For an in-depth description of supervised and unsupervised classification approaches, as well as the theory underlying each approach see Frank, J. 2006 (27)).

The 2D clustering and averaging strategy that is often used currently is fundamentally rooted in an un-supervised method, K-means clustering. The data set is successively divided into

a predefined number of classes K. Initialization of the K templates can either come from K randomly selected images from the entire data set, or the average computed within K randomly assigned groups. Given the initial set of K templates, the algorithm proceeds in an iterative way by alternating two steps, (1) distance between the K templates and each individual image is computed and each image is assigned to the closest (most similar) template, (2) based on the previous assignments, new class averages are computed and used as the template for the next round of assignments.

The key limitation of K-means clustering is that the choice of distance measure may affect the convergence, and achieving the global optimum is not guaranteed. However, these problems can be improved by a 'soft assignment', in which an image can be a member of several classes with weighting factors. This method can be formalized using the Maximum Likelihood methodology (58), with estimation of other statistical properties of the image.

1.3.4. Three-dimensional reconstruction techniques

Reconstruction of a 3D object from its 2D projection images can be performed in real space, using methods such as weighted back-projection and iterative algebraic reconstruction techniques, or in Fourier space. The fundamental theorem underlying 3D reconstruction is the projection theorem, which states that each projection of an object furnishes a central section of the object's 3D Fourier transform (Figure 1.4). It follows from the theorem that a reconstruction can be obtained by 3D inverse Fourier transformation of this 3D Fourier domain which is filled in by data from the 2D Fourier sections. For an in-depth review please refer to (37) and (27).

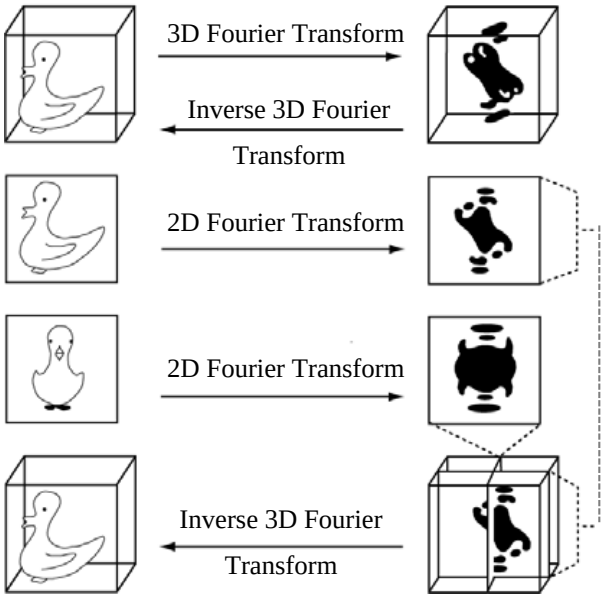

Figure 1.4 Illustration of the projection theorem and its use in 3D reconstruction. Reproduced from (27)

Weighted back-projection has been widely used because it is fast compared to iterative methods. As the term indicates, back-projection 'smears out' a 2D image into a 3D volume, ("back-projection body"). However, summation of these back-projection bodies yields a blurry object. The main reason is that, in Fourier space, the density of sampling points obtained by projections decreases as the spatial frequency increases. In other words, Fourier amplitudes at low spatial frequencies are overemphasized compared to those at high spatial frequencies. This problem is solved either by Fourier weighting of the projection prior to the back-projection step, or by weighting the 3D Fourier transform appropriately.

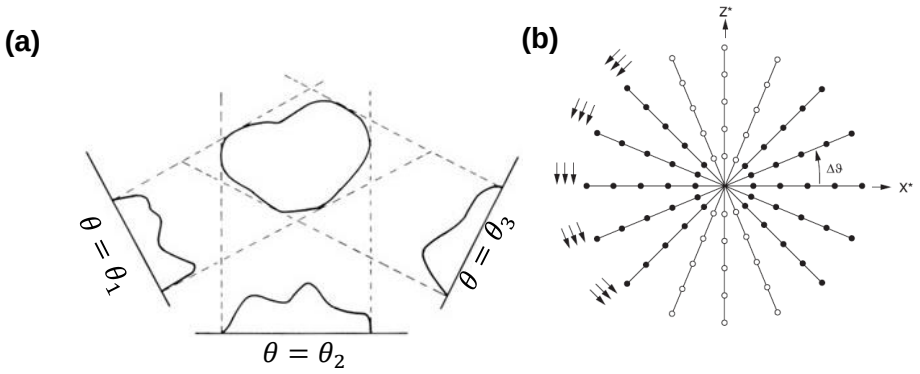

Figure 1.5 Illustration of back-projection method of 3D reconstruction. (**a**) The density distribution across a projection is "smeared out" in the original direction of projection, forming a "back-projection body". Summation of these back-projection bodies yields an approximation to the object (**b**) Analysis in Fourier space. Fourier amplitudes at low spatial frequencies are overemphasized in comparison with those higher spatial frequencies. Figures were reproduced from (27).

In ***iterative algebraic methods***, the relationship between the object and the set of projections can be formulated by a set of algebraic equations over a finite region. The Algebraic Reconstruction Technique (ART) and Simultaneous Iterative Reconstruction Technique (SIRT) are the two most often used techniques to find a 3D reconstruction such that its 2D projections are most similar to the input image. It starts from an initial estimation of the 3D density map and minimizes the discrepancy between the experimentally measured image and the calculated projection in an iterative fashion. Iterative algebraic methods, compared with weighted back-projection, are more accurate, flexible, and capable of incorporating additional constraints and considering the noise statistics. However, they require a much larger computational efforts and are extremely time-consuming for convergence to be reached.

Fourier reconstruction methods are intuitively close to approaches in X-ray or electron crystallography, where data are collected to fill Fourier space so that the inverse Fourier transform generate the map of the object in real space. In practice, the information is not complete and must be rebuilt by interpolation between the central sections. Several interpolation and inversion methods have been used (59-61).

Single-particle 3D reconstruction algorithms have been implemented in several software packages, such as IMAGIC (62), SPIDER (42,63), XMIPP (64) EMAN (48), FREALIGN (65), and RELION (19,20). In this study, SPIDER and RELION were used, with RELION is the one being used most extensively. A brief introduction to SPIDER is provided below, and details on RELION are described in section 1.4.

SPIDER, (System for Processing Image Data from Electron microscopy and Related fields), is a modular image processing system for electron image processing, developed in the Frank lab in 1981 (42). The distribution of SPIDER software package has two separate modules: SPIDER and JWEB. The SPIDER module is written in FORTRAN and used for mathematical manipulation of images and their contents. The JWEB module, added later on (66), is written in Java and used for visualization and interaction with images. The emphasis of the SPIDER system is single-particle averaging and reconstruction; however, a variety of other operations are also available, including contrast enhancement, Fourier filtration and alignment (42,66). Protocols of SPIDER for processing from a set of electron micrographs to the 3D reconstruction density map were described in (67). Two approaches are available to generate an *ab initio* structure (i) random-conical reconstruction and (ii) multiple common lines. Alternatively, if an initial 3D structure of the target or a structurally related assembly is already available, the approach of reference-based single-particle reconstruction can be used.

1.3.5. Structure refinement and resolution assessment

The initial 3D reconstruction is usually far from optimal and needs to be refined to obtain the final map. The refinement procedure alternates between the following two steps iteratively: (1) The experimental projection is compared with all reference projections, which are the re-projections of the current 3D reference structure. The orientation yielding the best match, in terms of cross-correlation value, denotes the desired projection direction. (2) Once the experimental projections have assigned updated parameters, an updated 3D reconstruction is computed and used as the new reference structure in the next iteration of the process.

To quantitatively evaluate the refined results, "resolution" is often used as a numerical indicator, which is a measure of the resolvability of object details reconstructed in the density map. Here, we evaluate the resolution using the 'gold standard' protocol with the FSC = 0.143 criterion. In this approach, the data are split into two equivalent halves, usually by separating even and odd numbered images, and each half-set is reconstructed and refined independently. The Fourier Shell Correlation (FSC), the cross-correlation coefficients over spatial frequency shells $(k, \Delta k)$ with increasing radius k between the Fourier transforms of the two independent reconstructions $(F_1(k), F_2(k))$, is computed (27,68):

$$FSC(k) = \frac{\sum_{k,\Delta k} F_1(k) F_2^*(k)}{\left| \sum_{k,\Delta k} |F_1(k)|^2 \sum_{k,\Delta k} |F_2(k)|^2 \right|^{1/2}}$$

The resolution is then derived according to the comparison between the measured FSC and an empirical threshold value (71-72), with FSC=0.143 being the most commonly used one. The FSC=0.143 criterion, proposed by Rosenthal and Henderson (72) is based on relating cryo-EM results to those in X-ray crystallography (72). It is also worth noting that, in practice, special care of the statistical independence of the two half-sets must be taken into consideration. (For the implementation of the "gold-standard" approach in RELION refinement, see (20).)

Additionally, for validation we also use structural features to help us confirm the resolution indicated by the FSC. A low-resolution map, >10Å, reveals the overall shape of the molecules and possibly the rough arrangements of the domains or subunits in a complex. An intermediate resolution map, ~4-10Å, reveals secondary structures such as α-helices and the relative arrangements of domains or subunits in a complex. A near-atomic resolution, <4Å, the map clearly resolves secondary structural features, such as β-strands and allows polypeptide backbone tracing.

1.4. Recent technological advances in single-particle cryo-EM

1.4.1. Improvements of the instruments

Although the quality of microscopes has been gradually improved, acquiring high quality images, i.e., images with high contrast and with sufficient resolution to answer the biological questions being asked, is still a challenging task. There are two main limiting factors, (i) the quality of the image-recording medium and (ii) the image blurring caused by motion induced by the electron beam and the mechanical instability of the specimen holder. The recent development of a new generation of direct electron detection cameras offers clear advantages over both photographic film and scintillator-based CCD cameras, and could overcome both limiting factors.

In terms of the quality of the image-recording medium, we use the detective quantum efficiency (DQE) to measure the quality of a detector. DQE is defined as the ratio of the square of the output signal-to-noise ratio $(S/N)_{out}$ to the square of the input signal-to-noise ratio $(S/N)_{in}$ (73):

$$DQE = (S/N)^2_{out}/(S/N)^2_{in}$$

It provides the measurement of the quality with which incident electrons are recorded. An ideal detector would detect all incident electron equally and so would have a DQE of 1, but a real detector has values less than 1. The new generation of direct electron detection cameras, as their

name suggest, can directly detect incoming electrons without the need for a scintillator, which produce high DQE at high electron energies. Direct Electron DE-20, FEI Falcon-2 and GATAN K2 Summit are the three most widely used commercially detectors, and they all have high DQEs in both low- and high-resolution regimes (74) (Figure 1.6).

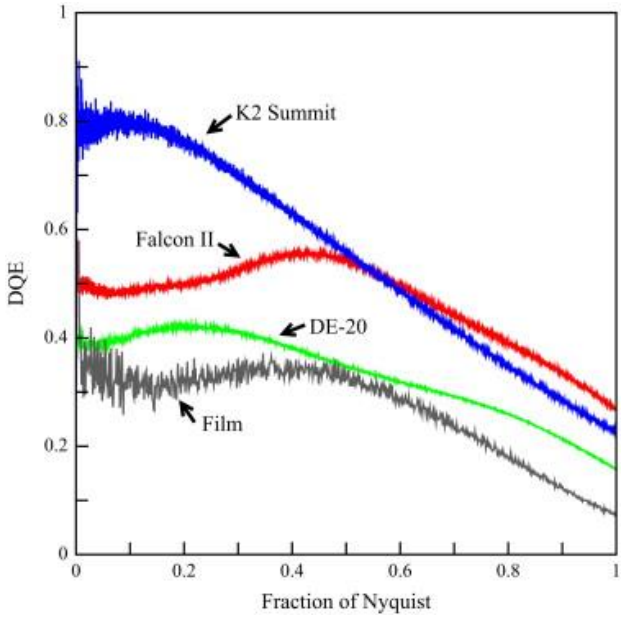

Figure 1.6 Measured DQE as a function of spatial frequency for the three DDD cameras. DE-20 (green), Falcon II (red) and K2 Summit (blue). The corresponding DQE of photographic film is given for the comparison and shown in black (74).

Image blurring, a major limiting factor to the improvement of attainable resolution, results from beam-induced movements of the molecules in the frozen-hydrated biological samples. In practice, such beam-induced motion is impossible to completely prevent. Here, the high frame rate (10–40 frames per second) of these new DDD cameras provides a means to correct for such image blurring by recording a 'movie' of multiple frames throughout the exposure. The total electron dose is fractionated into a series of image frames with sufficiently short duration such that the motion

can be reduced to an acceptable level. Later, these frames can be aligned using software packages to compensate for both global (MotionCorr (75), Unblur (76)) and local (77,78) specimen drift and beam-induced movements, thus reducing image blurring. In addition, the movie mode also offers the possibility of maximizing the image contrast by using a higher total dose. However, the later frames with the highest contrast have more accumulated electrons, and thus more radiation damages. These can be eliminated or properly down-weighted, so that the effect of radiation damage is minimized and the final averaged image is optimized (18,75,78).

In this study, we used a GATAN K2 Summit DDD camera to record dose-fractionated images, generally with a total specimen dose of ~20 to 50 electrons per $Å^2$, and a dose rate of ~5 to ~10 electron counts per physical pixel per second (79). The dose-fractionated image stacks are corrected for beam-induced movements using redundant measurements for a more accurate and self-consistent determination of image shifts (75). The corrected images with improved high-resolution information are used for subsequent reconstruction, classification and refinement.

1.4.2. Maximum likelihood-based classification

The major asset of cryo-EM is its ability to characterize the structures of molecules in their different functional states. However, it is always difficult to classify heterogeneous cryo-EM data sets into homogeneous subset. The variations come from two sources, the variation of molecule's orientation, and the variation of molecule's conformation and/or composition.

A breakthrough came with the development of the maximum-likelihood approach. It was first introduced into cryo-EM by Fred Sigworth for 2D averaging of projection (13). Whereas the conventional alignment approach is to find the unique optimal parameters (in-plane rotations and translations) for an image, the maximum-likelihood approach is to integrate over probability

distributions of all possible values and assign a number of in-plane orientation values to each image with proper weights.

This idea was later extended to 3D image classification and proved to be a particularly powerful tool for separating mixtures into structurally homogeneous subsets in both 2D (80) and 3D classification (15). Rather than a single class, the object is assigned to a member of several classes with probability weighting factors that are derived from the similarities between the object and the class averages. Application of the maximum likelihood method in 3D classification to a dataset of *E. coli 70S* ribosomes bound with EF-G provided the first indication that different structural states could be separated (15,81).

More recently, a variant of the maximum-likelihood approach was introduced in the form of an empirical Bayesian approach (19). The difference between the earlier maximum-likelihood approaches and this current Bayesian approach lies in a regularization term that expresses the prior knowledge about the 3D reconstruction:

$$P(\Theta|X,Y) \propto P(\mathrm{X}|\Theta,Y)\,P(\Theta|Y)$$

$P(\mathrm{X}|\Theta,Y)$ is the likelihood that quantifies the probability of observing the data given the model with parameter set Θ; $P(\Theta|Y)$ expresses how likely that parameter set Θ is, given the prior information. Optimizing the posterior distribution $P(\Theta|X,Y)$ is called maximum a posteriori estimation (MAP), whereas optimizing the likelihood $P(\mathrm{X}|\Theta,Y)$ is the maximum likelihood estimation.

Specifically, in the field of cryo-EM, our target is to find a solution for the 3D EM density distribution with parameter sets $\Theta = \{V_1, V_2, \dots, V_k\}$ based on the observed data $X = \{X_1, X_2, \dots X_N\}$, and the prior knowledge $P(\Theta|Y)$. N is the number total of particles, and K is the number of different structures. These structures$\{V_1, V_2, \dots, V_k\}$ differ from each other in terms of

composition and/or conformation. An experimental observed particle X_i is a 2D projection of one of the 3D structure V_{k_i}. The prior knowledge is the fact that the density of macromolecular structure is a smooth function.

More specifically, recall the weak-phase object approximation introduced in section 1.2.1, the observed data X_i can be expressed as following,

$$X_{ij} = CTF_{ij} \sum_{l=1}^{L} P_{jl}^{\varphi} V_l + N_{ij}$$

where:

- X_{ij} is the j-th component of the 2D Fourier transform of the observed 2D particle X_i. i=1,2,…N. j=1,2,…J and J=D^2. (D is the number of pixels in 1D).
- CTF_{ij} is the j-th component of the contrast transfer function (CTF) of X_i.
- $V_{k_i l}$ is the l-th component of the 3D Fourier transform of the 3D structure V_{k_i}, l=1,2,…L and L=D^3.
- N_{ij} is the noise in Fourier space, which follows the Gaussian distribution with mean value=0 and variance σ^2.

For the detailed solution of MAP see (58) and for its implementation details see (19,20). For a schematic interpretation of the Bayesian approach implemented in RELION, see Figure 1.7.

The Bayesian approach has the potential to yield clean, high-resolution reconstructions with a minimum of user intervention mainly because (i) the powers of noise and signal are inferred from the data, (ii) CTF (contrast transfer function) effects on both phases and amplitudes are corrected iteratively, and (iii) overfitting is monitored by the independent refinement of two separate halves of the data (82). The RELION software package has streamlined the whole image

processing workflow and provided the community a tool for high-resolution structure determination and the handling of structurally heterogeneous datasets with minimum user interference (19,20,53).

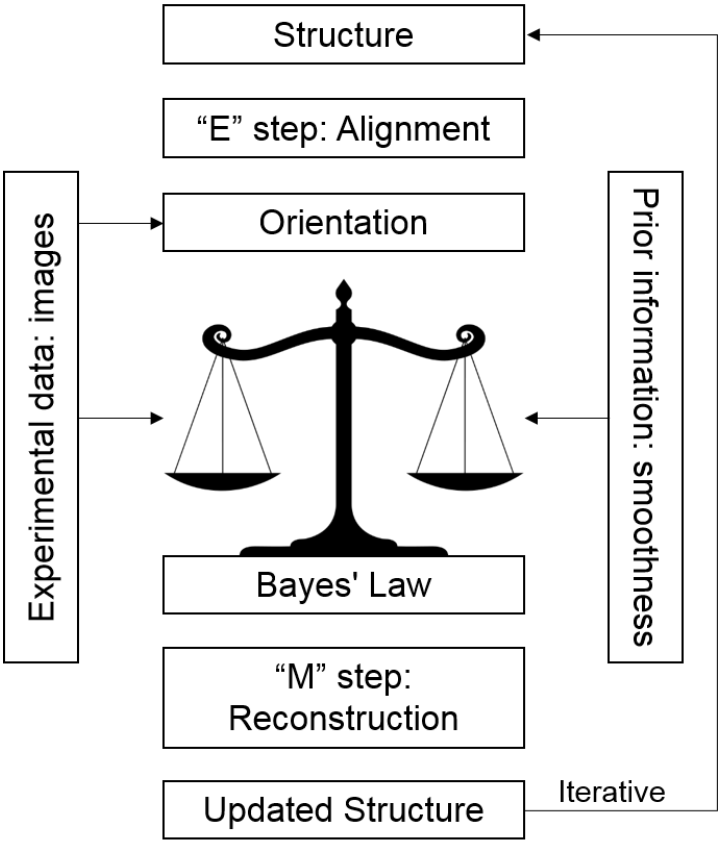

Figure 1.7 Schematic illustration of the Bayesian approach. The structure is iteratively refined through a two-step procedure. The first step, which is called Expectation in mathematical terms, has been labeled “E step: Alignment.” In this step, calculated projections of the structure are compared with the experimental images, resulting in information about the relative orientations of the images. Orientations are assigned in a probability distributions manner. The second step is called Maximization and has been labeled “M step: Reconstruction.” In this step, the

experimentally observed images are combined with the constructing prior information, smoothness, into a 3D reconstruction. The estimates for the powers of noise and signal in the data are also updated. The relative contributions of the experimental data and the prior to the reconstruction are dictated by Bayes' law and depend on the powers of noise and signal in the data. The new structure and the updated estimates for the powers of noise and signal are then used for the subsequent iteration. Iterations are typically stopped after a user-defined number or when the structures do not change significantly. Figure is adapted from (19).

1.4.3. Current availability of single-particle cryo-EM

Single-particle cryo-EM has evolved very dramatically since its first recorded application to T4 bacteriophage tail (1). A few years ago, single-particle cryo-EM was usually not the first choice for many biologists due to its limited resolution. Now, this method rivals conventional X-ray crystallography and has gained world-wide attention. The development of new instrumentation and image-processing methods, and as well as the advent of automation in data collection and analysis, have transformed cryo-EM, enabling understanding of complex structures and their functions at the near-atomic level.

Achieving crystallographic-resolution structures

The recent technological advances have led to a major breakthrough in achievable resolution, resulting in many 3 ~ 5 Å resolution structures of biological molecules, ranging from ribosomal particles to integral membrane proteins. Figure 1.8, Table 1.2 and Table 1.3 summarize part of the cryo-EM structures that were determined using a DDD to a resolution beyond 5Å (data were released on EMDB by June 2016). These structures serve as good illustrations of the opportunities that the new advanced technology has provided for structural biology research. Here

I would like to highlight the first three groups that obtained structures beyond 3.5 Å, at which most of the amino acid side chains were visible and the atomic model can be built *de novo*. The Cheng lab at UCSF solved the atomic structure of a transient receptor cation channel (TRPV1) channel using the GATAN K2 DDD camera in 2013 (22,83). In the year of 2014, the Kühlbrandt and Vonck groups at the Max Planck Institute in Frankfurt solved the structure of F420-reducing [NiFe] hydrogenase (FRH) at resolution of 3.4 Å (84) and the Ramakrishnan and Scheres groups at the MRC obtained the structure of the large subunit of the mitochondrial ribosome from yeast at a resolution of 3.2 Å (85).

At these resolutions, cryo-EM density maps of large macromolecular assemblies are comparable to those obtained by X-ray crystallography. Thus, the tools developed for the building and refinement of crystal structures could be adopted for cryo-EM. The models for the three structures mentioned above were built using COOT (86) and refined using REFMAC (87), the programs original designed for, and are widely used in, X-ray crystallography.

Working with heterogeneous specimens

One major asset for cryo-EM is that it can work on structurally heterogeneous samples. Complexes of ribosomes with different factors are good examples (Table 1.2). In the instance of the 80S ribosome in complex with eFI5B, the structurally most interesting state only represented 3% of the recorded particle images (88). Other ribosome examples are the *P. falciparum* 80S ribosomes (89), the mitochondrial *S. cerevisiae* large ribosomal subunit (85), the 80S ribosome bound with IRES (90) and CrPV IRES (91). In all these cases, a maximum likelihood-based 3D classification procedure was successfully used to separate particles corresponding to the structurally different states. For other complexes that are smaller than the ribosomes, or that contain continuously flexing domains, disentangling the structurally heterogeneity is more

difficult. For example, in the case of γ-secretase, 3D classification was used to enrich the data set with good particles, but density for the flexible transmembrane domain was poorly resolved. In order to tackle these problems, a modified focused classification and refinement method was used, which focuses on the target region of each experimental image after subtraction of the averaged signal. (Focused classification was originally developed by Penczek *et al* (94), and the signal subtraction idea has also been used in several different studies before (92-95).) Using the maximum-likelihood approach, the modified focused classification method has been able to visualize conformational dynamics of flexible regions that only differ in a few α-helices (97). Moreover, the implementation of this method into RELION software package makes it more easily assessable and applicable.

In addition, the use of automated data acquisition, such as Leginon (98), enables collecting large datasets in relatively short periods of time. With larger image datasets, it will be possible to classify particle images with very subtle conformational differences.

Working with smaller specimens

The quality of the cryo-EM map of a molecule depends on the accuracy with which the particle images can be aligned. Alignment works better for larger particles (99). Samples such as viruses or ribosomes are now being routinely pursued using cryo-EM, rather than X-ray crystallography. However, molecules with smaller size used to pose difficulties for achieving atomic-resolution structures, because of the low contrast images. Currently, the new camera technology, with a combination of rapid readout and nearly noiseless electron counting, can provide images with notable high contrast and high-resolution image information. Researchers at MRC-LMB and Tsinghua University obtained 3Å resolution for a small molecule, γ-secretase, which only has a total molecular weight of 170kDa (23,97,100). Moreover, at the time this chapter

is being edited, the Subramaniam group from NIH have reached the near-atomic resolution structure of an even smaller molecule, a 93 kDa enzyme (101). These exciting results show the tremendous promise of single-particle cryo-EM in the structural biology field.

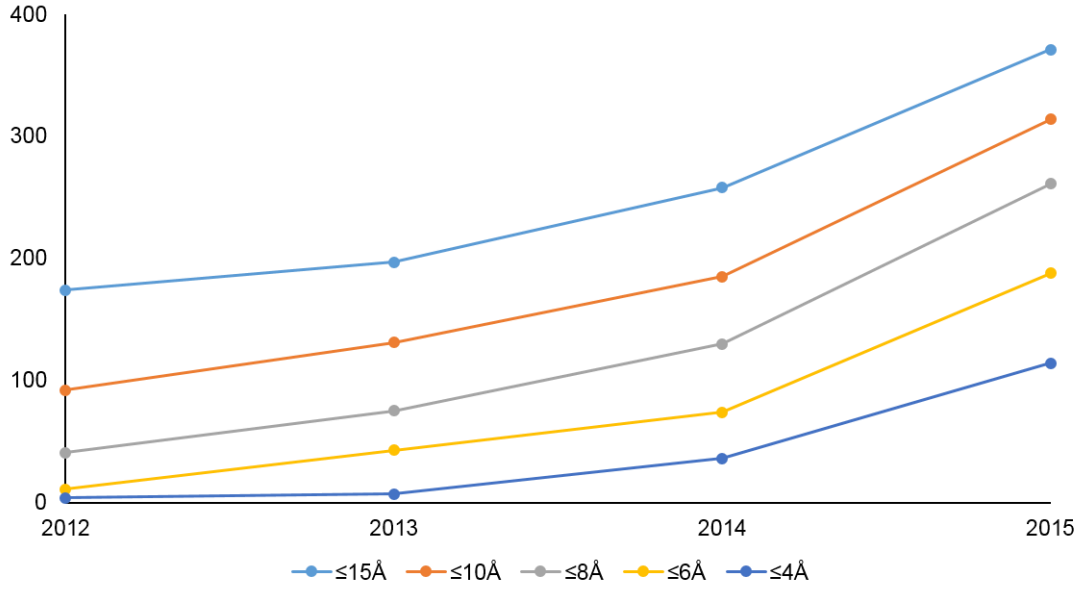

Figure 1.8 Number of maps achieving a given resolution in the years from 2012 to 2015. Y-axis represents the number of maps at a given resolution. Data was obtained from EMDB (https://www.ebi.ac.uk/pdbe/emdb/statistics_main.html).

Sample	Resolution	Detector	Software	EMDB
Yeast 60S subunit	2.9 Å	GATAN K2	FREALIGN	6478 (102)
P. falciparum 80S ribosome + emetine	3.2 Å	Falcon II	RELION	2660 (103)
Yeast 80S mitoribosome (LSU)	3.2 Å	Falcon II	RELION	2566 (85)
Human 80S mitoribosome (LSU)	3.3 Å	Falcon II	RELION	2879 (104)
D. discoideum 60S subunit + eIF6 + SBD	3.3 Å	Falcon II	RELION	3145 (105)
Human 80S ribosomes (POST state)	3.5 Å	Falcon II	SPIDER/SPARX	2875 (106)
E. coli 70S ribosome + EF-G	3.6 Å	Falcon II	RELION	6315 (107)
80S ribosome + CrPV-IRES	3.7 Å	Falcon II	RELION	2599 (91)
80S ribosome + eIF5B	4.3 Å	Falcon I	RELION	2421 (88)
Yeast 80S ribosome	4.5 Å	Falcon I	RELION	2275 (21)

Table 1.2. Recent cryo-EM single-particle reconstructions of ribosomes that were obtained using a DDD camera. Raw data was obtained from EMDB database (till April 2016).

Sample	Resolution	MW	Detector	Software	EMDB
Glutamate dehydrogenase	1.8 Å	0.3 MDa	K2 (XP-sensor)	FREALIGN	8194 (101)
β-galactosidase + PETG	2.2 Å	0.5 MDa	Falcon II	FREALIGN	2984 (108)
T20S proteasome	2.8 Å	0.7 MDa	K2	RELION	6287 (24)
TRPV1 + DkTx + RTX (by nanodiscs)	2.95 Å	0.3 MDa	K2	RELION	8117 (109)
TRPV1	3.3 Å	0.3 MDa	K2	RELION	5778 (22)
F420-reducing hydrogenase Frh	3.4 Å	1.2 MDa	Falcon II	RELION	2513 (84)
Zika virus	3.8 Å	10 MDa	Falcon II	EMAN	8139 (110)
TRPV1 + DkTx + RTX	3.8 Å	0.3 MDa	K2	RELION	5776 (83)
Human core-PIC	3.9 Å	0.9 MDa	K2	RELION	8136 (111)
Dengue virus	4.1 Å	50 MDa	Falcon I	EMAN	2485 (112)
Rotavirus	4.4 Å	35 MDa	DE -12	FREALIGN	5488 (18)
Human γ-secretase	4.5 Å	0.17 MDa	K2	RELION	2677 (100)
Sulfolobus turreted virus	4.5 Å	75 MDa	Falcon I	FREALIGN	5584 (113)

Table 1.3. High-resolution cryo-EM single-particle reconstructions that were obtained using a DDD camera. Data was obtained from EMDB (till May 2016)

1.5. References

1. De Rosier, D.J. and Klug, A. (1968) Reconstruction of Three Dimensional Structures from Electron Micrographs. *Nature*, **217**, 130-134.

2. Unwin, P.N.T. and Henderson, R. (1975) Molecular-Structure Determination by Electron-Microscopy of Unstained Crystalline Specimens. *Journal of Molecular Biology*, **94**, 425-&.

3. Taylor, K.A. and Glaeser, R.M. (1976) Electron-Microscopy of Frozen Hydrated Biological Specimens. *J Ultra Mol Struct R*, **55**, 448-456.

4. Frank, J., Verschoor, A. and Boublik, M. (1981) Computer Averaging of Electron-Micrographs of 40s Ribosomal-Subunits. *Science*, **214**, 1353-1355.

5. Van Heel, M. and Frank, J. (1981) Use of multivariate statistics in analysing the images of biological macromolecules. *Ultramicroscopy*, **6**, 187-194.

6. Dubochet, J., Lepault, J., Freeman, R., Berriman, J.A. and Homo, J.C. (1982) Electron-Microscopy of Frozen Water and Aqueous-Solutions. *J Microsc-Oxford*, **128**, 219-237.

7. Radermacher, M., Wagenknecht, T., Verschoor, A. and Frank, J. (1987) 3-Dimensional Reconstruction from a Single-Exposure, Random Conical Tilt Series Applied to the 50s-Ribosomal Subunit of Escherichia-Coli. *J Microsc-Oxford*, **146**, 113-136.

8. Henderson, R., Baldwin, J.M., Ceska, T.A., Zemlin, F., Beckmann, E. and Downing, K.H. (1990) Model for the Structure of Bacteriorhodopsin Based on High-Resolution Electron Cryomicroscopy. *Journal of Molecular Biology*, **213**, 899-929.

9. Penczek, P.A., Grassucci, R.A. and Frank, J. (1994) The Ribosome at Improved Resolution - New Techniques for Merging and Orientation Refinement in 3d Cryoelectron Microscopy of Biological Particles. *Ultramicroscopy*, **53**, 251-270.

10. Unwin, N. (1995) Acetylcholine receptor channel imaged in the open state. *Nature*, **373**, 37-43.

11. Frank, J., Zhu, J., Penczek, P., Li, Y.H., Srivastava, S., Verschoor, A., Radermacher, M., Grassucci, R., Lata, R.K. and Agrawal, R.K. (1995) A Model of Protein-Synthesis Based on Cryoelectron Microscopy of the E-Coli Ribosome. *Nature*, **376**, 441-444.

12. Bottcher, B., Wynne, S.A. and Crowther, R.A. (1997) Determination of the fold of the core protein of hepatitis B virus by electron cryomicroscopy. *Nature*, **386**, 88-91.

13. Sigworth, F.J. (1998) A maximum-likelihood approach to single-particle image refinement. *J Struct Biol*, **122**, 328-339.

14. Gonen, T., Cheng, Y.F., Sliz, P., Hiroaki, Y., Fujiyoshi, Y., Harrison, S.C. and Walz, T. (2005) Lipid-protein interactions in double-layered two-dimensional AQPO crystals. *Nature*, **438**, 633-638.

15. Scheres, S.H., Gao, H., Valle, M., Herman, G.T., Eggermont, P.P., Frank, J. and Carazo, J.M. (2007) Disentangling conformational states of macromolecules in 3D-EM through likelihood optimization. *Nat Methods*, **4**, 27-29.

16. Yu, X., Jin, L. and Zhou, Z.H. (2008) 3.88 A structure of cytoplasmic polyhedrosis virus by cryo-electron microscopy. *Nature*, **453**, 415-419.

17. Brilot, A.F., Chen, J.Z., Cheng, A., Pan, J., Harrison, S.C., Potter, C.S., Carragher, B., Henderson, R. and Grigorieff, N. (2012) Beam-induced motion of vitrified specimen on holey carbon film. *J Struct Biol*, **177**, 630-637.

18. Campbell, M.G., Cheng, A.C., Brilot, A.F., Moeller, A., Lyumkis, D., Veesler, D., Pan, J.H., Harrison, S.C., Potter, C.S., Carragher, B. *et al.* (2012) Movies of Ice-Embedded Particles Enhance Resolution in Electron Cryo-Microscopy. *Structure*, **20**, 1823-1828.

19. Scheres, S.H. (2012) A Bayesian view on cryo-EM structure determination. *J Mol Biol*, **415**, 406-418.

20. Scheres, S.H. (2012) RELION: implementation of a Bayesian approach to cryo-EM structure determination. *J Struct Biol*, **180**, 519-530.

21. Bai, X.C., Fernandez, I.S., McMullan, G. and Scheres, S.H. (2013) Ribosome structures to near-atomic resolution from thirty thousand cryo-EM particles. *Elife*, **2**, e00461.

22. Liao, M., Cao, E., Julius, D. and Cheng, Y. (2013) Structure of the TRPV1 ion channel determined by electron cryo-microscopy. *Nature*, **504**, 107-112.

23. Bai, X.C., Yan, C., Yang, G., Lu, P., Ma, D., Sun, L., Zhou, R., Scheres, S.H. and Shi, Y. (2015) An atomic structure of human gamma-secretase. *Nature*, **525**, 212-217.

24. Campbell, M.G., Veesler, D., Cheng, A.C., Potter, C.S. and Carragher, B. (2015) 2.8 angstrom resolution reconstruction of the Thermoplasma acidophilum 20S proteasome using cryo-electron microscopy. *Elife*, **4**.

25. Merk, A., Bartesaghi, A., Banerjee, S., Falconieri, V., Rao, P., Davis, M.I., Pragani, R., Boxer, M.B., Earl, Lesley A., Milne, Jacqueline L.S. *et al.* Breaking Cryo-EM Resolution Barriers to Facilitate Drug Discovery. *Cell*.

26. Dubochet, J., Adrian, M., Chang, J.J., Homo, J.C., Lepault, J., Mcdowall, A.W. and Schultz, P. (1988) Cryo-Electron Microscopy of Vitrified Specimens. *Q Rev Biophys*, **21**, 129-228.

27. Frank, J. (2006) *Three-dimensional electron microscopy of macromolecular assemblies : visualization of biological molecules in their native state*. [2nd ed. Oxford University Press, New York.

28. Glaeser, R.M. (1985) Electron Crystallography of Biological Macromolecules. *Annu Rev Phys Chem*, **36**, 243-275.

29. Nogales, E. and Chiu, W. (1999) Electron crystallography of biological macromolecules. *Journal of Structural Biology*, **128**, 1-2.

30. Pantelic, R.S., Suk, J.W., Magnuson, C.W., Meyer, J.C., Wachsmuth, P., Kaiser, U., Ruoff, R.S. and Stahlberg, H. (2011) Graphene: Substrate preparation and introduction. *Journal of Structural Biology*, **174**, 234-238.

31. Russo, C.J. and Passmore, L.A. (2014) Controlling protein adsorption on graphene for cryo-EM using low-energy hydrogen plasmas (vol 11, pg 649, 2014). *Nature Methods*, **11**, 773-773.

32. Russo, C.J. and Passmore, L.A. (2014) Electron microscopy: Ultrastable gold substrates for electron cryomicroscopy. *Science*, **346**, 1377-1380.

33. Russo, C.J. and Passmore, L.A. (2016) Ultrastable gold substrates: Properties of a support for high-resolution electron cryomicroscopy of biological specimens. *Journal of Structural Biology*, **193**, 33-44.

34. Reimer, L. (1992) Transmission Electron-Microscopy. *Diagnostics and Applications of Thin Films*, 1-20.

35. Reimer, L. and Kohl, H. (2008), *Springer series in optical sciences 36*. 5th ed. Springer,, New York, NY.

36. Spence, J.C.H. (1988) *Experimental high-resolution electron microscopy*. 2nd ed. Oxford University Press, New York.

37. Orlova, E.V. and Saibil, H.R. (2011) Structural Analysis of Macromolecular Assemblies by Electron Microscopy. *Chem Rev*, **111**, 7710-7748.

38. Wade, R.H. (1992) A brief look at imaging and contrast transfer. *Ultramicroscopy*, **46**, 145-156.

39. Faruqi, A.R. and Subramaniam, S. (2000) CCD detectors in high-resolution biological electron microscopy. *Q Rev Biophys*, **33**, 1-27.

40. Bammes, B.E., Rochat, R.H., Jakana, J., Chen, D.H. and Chiu, W. (2012) Direct electron detection yields cryo-EM reconstructions at resolutions beyond 3/4 Nyquist frequency. *J Struct Biol*, **177**, 589-601.

41. Milazzo, A.C., Cheng, A., Moeller, A., Lyumkis, D., Jacovetty, E., Polukas, J., Ellisman, M.H., Xuong, N.H., Carragher, B. and Potter, C.S. (2011) Initial evaluation of a direct detection device detector for single particle cryo-electron microscopy. *J Struct Biol*, **176**, 404-408.

42. Frank, J., Shimkin, B. and Dowse, H. (1981) Spider - a Modular Software System for Electron Image-Processing. *Ultramicroscopy*, **6**, 343-357.

43. Ludtke, S.J., Baldwin, P.R. and Chiu, W. (1999) EMAN: semiautomated software for high-resolution single-particle reconstructions. *J Struct Biol*, **128**, 82-97.

44. Mindell, J.A. and Grigorieff, N. (2003) Accurate determination of local defocus and specimen tilt in electron microscopy. *J Struct Biol*, **142**, 334-347.

45. Rohou, A. and Grigorieff, N. (2015) CTFFIND4: Fast and accurate defocus estimation from electron micrographs. *Journal of Structural Biology*, **192**, 216-221.

46. Zhang, K. (2016) Gctf: Real-time CTF determination and correction. *J Struct Biol*, **193**, 1-12.

47. Marabini, R., Carragher, B., Chen, S., Chen, J., Cheng, A., Downing, K.H., Frank, J., Grassucci, R.A., Bernard Heymann, J., Jiang, W. *et al.* (2015) CTF Challenge: Result summary. *J Struct Biol*, **190**, 348-359.

48. Tang, G., Peng, L., Baldwin, P.R., Mann, D.S., Jiang, W., Rees, I. and Ludtke, S.J. (2007) EMAN2: an extensible image processing suite for electron microscopy. *J Struct Biol*, **157**, 38-46.

49. Chen, J.Z. and Grigorieff, N. (2007) SIGNATURE: a single-particle selection system for molecular electron microscopy. *J Struct Biol*, **157**, 168-173.

50. Voss, N.R., Yoshioka, C.K., Radermacher, M., Potter, C.S. and Carragher, B. (2009) DoG Picker and TiltPicker: software tools to facilitate particle selection in single particle electron microscopy. *J Struct Biol*, **166**, 205-213.

51. Sorzano, C.O., Recarte, E., Alcorlo, M., Bilbao-Castro, J.R., San-Martin, C., Marabini, R. and Carazo, J.M. (2009) Automatic particle selection from electron micrographs using machine learning techniques. *J Struct Biol*, **167**, 252-260.

52. Langlois, R., Pallesen, J., Ash, J.T., Nam Ho, D., Rubinstein, J.L. and Frank, J. (2014) Automated particle picking for low-contrast macromolecules in cryo-electron microscopy. *J Struct Biol*, **186**, 1-7.

53. Scheres, S.H. (2015) Semi-automated selection of cryo-EM particles in RELION-1.3. *J Struct Biol*, **189**, 114-122.

54. Huang, Z. and Penczek, P.A. (2004) Application of template matching technique to particle detection in electron micrographs. *J Struct Biol*, **145**, 29-40.

55. Sigworth, F.J. (2004) Classical detection theory and the cryo-EM particle selection problem. *J Struct Biol*, **145**, 111-122.

56. Hashem, Y., des Georges, A., Dhote, V., Langlois, R., Liao, H.Y., Grassucci, R.A., Pestova, T.V., Hellen, C.U.T. and Frank, J. (2013) Hepatitis-C-virus-like internal ribosome entry sites displace eIF3 to gain access to the 40S subunit. *Nature*, **503**, 539-+.

57. Hashem, Y., Georges, A.D., Dhote, V., Langlois, R., Liao, H.Y., Grassucci, R.A., Hellen, C.U.T., Pestova, T.V. and Frank, J. (2013) Structure of the Mammalian Ribosomal 43S Preinitiation Complex Bound to the Scanning Factor DHX29. *Cell*, **153**, 1108-1119.

58. MacKay, D.J.C. (2003) *Information theory, inference, and learning algorithms*. Cambridge University Press, Cambridge, U.K. ; New York.

59. Lanzavecchia, S. and Bellon, P.L. (1996) Electron tomography in conical tilt geometry. The accuracy of a direct Fourier method (DFM) and the suppression of non-tomographic noise. *Ultramicroscopy*, **63**, 247-261.

60. Grigorieff, N. (1998) Three-dimensional structure of bovine NADH:ubiquinone oxidoreductase (complex I) at 22 A in ice. *J Mol Biol*, **277**, 1033-1046.

61. Penczek, P.A., Renka, R. and Schomberg, H. (2004) Gridding-based direct Fourier inversion of the three-dimensional ray transform. *J Opt Soc Am A Opt Image Sci Vis*, **21**, 499-509.

62. van Heel, M., Harauz, G., Orlova, E.V., Schmidt, R. and Schatz, M. (1996) A new generation of the IMAGIC image processing system. *J Struct Biol*, **116**, 17-24.

63. Shaikh, T.R., Gao, H.X., Baxter, W.T., Asturias, F.J., Boisset, N., Leith, A. and Frank, J. (2008) SPIDER image processing for single-particle reconstruction of biological macromolecules from electron micrographs. *Nature Protocols*, **3**, 1941-1974.

64. Sorzano, C.O., Marabini, R., Velazquez-Muriel, J., Bilbao-Castro, J.R., Scheres, S.H., Carazo, J.M. and Pascual-Montano, A. (2004) XMIPP: a new generation of an open-source image processing package for electron microscopy. *J Struct Biol*, **148**, 194-204.

65. Grigorieff, N. (2007) FREALIGN: high-resolution refinement of single particle structures. *J Struct Biol*, **157**, 117-125.

66. Frank, J., Radermacher, M., Penczek, P., Zhu, J., Li, Y., Ladjadj, M. and Leith, A. (1996) SPIDER and WEB: processing and visualization of images in 3D electron microscopy and related fields. *J Struct Biol*, **116**, 190-199.

67. Shaikh, T.R., Gao, H., Baxter, W.T., Asturias, F.J., Boisset, N., Leith, A. and Frank, J. (2008) SPIDER image processing for single-particle reconstruction of biological macromolecules from electron micrographs. *Nat Protoc*, **3**, 1941-1974.

68. Liao, H.Y. and Frank, J. (2010) Definition and Estimation of Resolution in Single-Particle Reconstructions. *Structure*, **18**, 768-775.

69. Orlova, E.V., Dube, P., Harris, J.R., Beckman, E., Zemlin, F., Markl, J. and vanHeel, M. (1997) Structure of keyhole limpet hemocyanin type 1 (KLH1) at 15 angstrom resolution by electron cryomicroscopy and angular reconstitution. *Journal of Molecular Biology*, **271**, 417-437.

70. Radermacher, M., Ruiz, T., Wieczorek, H. and Gruber, G. (2001) The structure of the V(1)-ATPase determined by three-dimensional electron microscopy of single particles. *J Struct Biol*, **135**, 26-37.

71. Bottcher, B., Wynne, S.A. and Crowther, R.A. (1997) Determination of the fold of the core protein of hepatitis B virus ky electron cryomicroscopy. *Nature*, **386**, 88-91.

72. Rosenthal, P.B. and Henderson, R. (2003) Optimal determination of particle orientation, absolute hand, and contrast loss in single-particle electron cryomicroscopy. *Journal of Molecular Biology*, **333**, 721-745.

73. McMullan, G., Chen, S., Henderson, R. and Faruqi, A.R. (2009) Detective quantum efficiency of electron area detectors in electron microscopy. *Ultramicroscopy*, **109**, 1126-1143.

74. McMullan, G., Faruqi, A.R., Clare, D. and Henderson, R. (2014) Comparison of optimal performance at 300keV of three direct electron detectors for use in low dose electron microscopy. *Ultramicroscopy*, **147**, 156-163.

75. Li, X., Mooney, P., Zheng, S., Booth, C.R., Braunfeld, M.B., Gubbens, S., Agard, D.A. and Cheng, Y. (2013) Electron counting and beam-induced motion correction enable near-atomic-resolution single-particle cryo-EM. *Nat Methods*, **10**, 584-590.

76. Grant, T. and Grigorieff, N. (2015) Measuring the optimal exposure for single particle cryo-EM using a 2.6 angstrom reconstruction of rotavirus VP6. *Elife*, **4**.

77. Rubinstein, J.L. and Brubaker, M.A. (2015) Alignment of cryo-EM movies of individual particles by optimization of image translations. *J Struct Biol*, **192**, 188-195.

78. Scheres, S.H. (2014) Beam-induced motion correction for sub-megadalton cryo-EM particles. *Elife*, **3**, e03665.

79. Li, X.M., Zheng, S.Q., Egami, K., Agard, D.A. and Cheng, Y.F. (2013) Influence of electron dose rate on electron counting images recorded with the K2 camera. *Journal of Structural Biology*, **184**, 251-260.

80. Scheres, S.H., Valle, M., Nunez, R., Sorzano, C.O., Marabini, R., Herman, G.T. and Carazo, J.M. (2005) Maximum-likelihood multi-reference refinement for electron microscopy images. *J Mol Biol*, **348**, 139-149.

81. Scheres, S.H.W., Nunez-Ramirez, R., Gomez-Llorente, Y., Martin, C.S., Eggermont, P.P.B. and Carazo, J.M. (2007) Modeling experimental image formation for likelihood-based classification of electron microscopy. *Structure*, **15**, 1167-1177.

82. Scheres, S.H.W. and Chen, S.X. (2012) Prevention of overfitting in cryo-EM structure determination. *Nature Methods*, **9**, 853-854.

83. Cao, E., Liao, M., Cheng, Y. and Julius, D. (2013) TRPV1 structures in distinct conformations reveal activation mechanisms. *Nature*, **504**, 113-118.

84. Allegretti, M., Mills, D.J., McMullan, G., Kuhlbrandt, W. and Vonck, J. (2014) Atomic model of the F420-reducing [NiFe] hydrogenase by electron cryo-microscopy using a direct electron detector. *Elife*, **3**, e01963.

85. Amunts, A., Brown, A., Bai, X.C., Llacer, J.L., Hussain, T., Emsley, P., Long, F., Murshudov, G., Scheres, S.H. and Ramakrishnan, V. (2014) Structure of the yeast mitochondrial large ribosomal subunit. *Science*, **343**, 1485-1489.

86. Emsley, P., Lohkamp, B., Scott, W.G. and Cowtan, K. (2010) Features and development of Coot. *Acta Crystallogr D*, **66**, 486-501.

87. Murshudov, G.N., Vagin, A.A. and Dodson, E.J. (1997) Refinement of macromolecular structures by the maximum-likelihood method. *Acta Crystallogr D*, **53**, 240-255.

88. Fernandez, I.S., Bai, X.C., Hussain, T., Kelley, A.C., Lorsch, J.R., Ramakrishnan, V. and Scheres, S.H. (2013) Molecular architecture of a eukaryotic translational initiation complex. *Science*, **342**, 1240585.

89. Sun, M., Li, W., Blomqvist, K., Das, S., Hashem, Y., Dvorin, J.D. and Frank, J. (2015) Dynamical features of the Plasmodium falciparum ribosome during translation. *Nucleic Acids Res*, **43**, 10515-10524.

90. Koh, C.S., Brilot, A.F., Grigorieff, N. and Korostelev, A.A. (2014) Taura syndrome virus IRES initiates translation by binding its tRNA-mRNA-like structural element in the ribosomal decoding center. *Proc Natl Acad Sci U S A*, **111**, 9139-9144.

91. Fernandez, I.S., Bai, X.C., Murshudov, G., Scheres, S.H. and Ramakrishnan, V. (2014) Initiation of translation by cricket paralysis virus IRES requires its translocation in the ribosome. *Cell*, **157**, 823-831.

92. Morais, M.C., Kanamaru, S., Badasso, M.O., Koti, J.S., Owen, B.A.L., McMurray, C.T., Anderson, D.L. and Rossmann, M.G. (2003) Bacteriophage phi 29 scaffolding protein gp7 before and after prohead assembly. *Nat Struct Biol*, **10**, 572-576.

93. Zhang, Y., Kostyuchenko, V.A. and Rossmann, M.G. (2007) Structural analysis of viral nucleocapsids by subtraction of partial projections. *Journal of Structural Biology*, **157**, 356-364.

94. Zhou, Q., Huang, X., Sun, S., Li, X.M., Wang, H.W. and Sui, S.F. (2015) Cryo-EM structure of SNAP-SNARE assembly in 20S particle. *Cell Research*, **25**, 551-560.

95. Park, E., Menetret, J.F., Gumbart, J.C., Ludtke, S.J., Li, W.K., Whynot, A., Rapoport, T.A. and Akey, C.W. (2014) Structure of the SecY channel during initiation of protein translocation. *Nature*, **506**, 102-+.

96. Penczek, P.A., Frank, J. and Spahn, C.M.T. (2006) A method of focused classification, based on the bootstrap 3D variance analysis, and its application to EF-G-dependent translocation. *Journal of Structural Biology*, **154**, 184-194.

97. Bai, X.C., Rajendra, E., Yang, G., Shi, Y. and Scheres, S.H. (2015) Sampling the conformational space of the catalytic subunit of human gamma-secretase. *Elife*, **4**.

98. Suloway, C., Pulokas, J., Fellmann, D., Cheng, A., Guerra, F., Quispe, J., Stagg, S., Potter, C.S. and Carragher, B. (2005) Automated molecular microscopy: the new Leginon system. *J Struct Biol*, **151**, 41-60.

99. Saxton, W.O. and Frank, J. (1977) Motif Detection in Quantum Noise-Limited Electron-Micrographs by Cross-Correlation. *Ultramicroscopy*, **2**, 219-227.

100. Lu, P., Bai, X.C., Ma, D., Xie, T., Yan, C., Sun, L., Yang, G., Zhao, Y., Zhou, R., Scheres, S.H. *et al.* (2014) Three-dimensional structure of human gamma-secretase. *Nature*, **512**, 166-170.

101. Merk, A., Bartesaghi, A., Banerjee, S., Falconieri, V., Rao, P., Davis, M.I., Pragani, R., Boxer, M.B., Earl, Lesley A., Milne, Jacqueline L.S. *et al.* (2016) Breaking Cryo-EM Resolution Barriers to Facilitate Drug Discovery. *Cell*.

102. Passos, D.O. and Lyumkis, D. (2015) Single-particle cryoEM analysis at near-atomic resolution from several thousand asymmetric subunits. *Journal of Structural Biology*, **192**, 235-244.

103. Wong, W., Bai, X.C., Brown, A., Fernandez, I.S., Hanssen, E., Condron, M., Tan, Y.H., Baum, J. and Scheres, S.H. (2014) Cryo-EM structure of the Plasmodium falciparum 80S ribosome bound to the anti-protozoan drug emetine. *Elife*, **3**.

104. Amunts, A., Brown, A., Toots, J., Scheres, S.H.W. and Ramakrishnan, V. (2015) The structure of the human mitochondrial ribosome. *Science*, **348**, 95-98.

105. Weis, F., Giudice, E., Churcher, M., Jin, L., Hilcenko, C., Wong, C.C., Traynor, D., Kay, R.R. and Warren, A.J. (2015) Mechanism of eIF6 release from the nascent 60S ribosomal subunit. *Nat Struct Mol Biol*, **22**, 914-919.

106. Behrmann, E., Loerke, J., Budkevich, T.V., Yamamoto, K., Schmidt, A., Penczek, P.A., Vos, M.R., Burger, J., Mielke, T., Scheerer, P. *et al.* (2015) Structural Snapshots of Actively Translating Human Ribosomes. *Cell*, **161**, 845-857.

107. Li, W., Liu, Z., Koripella, R.K., Langlois, R., Sanyal, S. and Frank, J. (2015) Activation of GTP hydrolysis in mRNA-tRNA translocation by elongation factor G. *Sci Adv*, **1**.

108. Bartesaghi, A., Merk, A., Banerjee, S., Matthies, D., Wu, X.W., Milne, J.L.S. and Subramaniam, S. (2015) 2.2 angstrom resolution cryo-EM structure of beta-galactosidase in complex with a cell-permeant inhibitor. *Science*, **348**, 1147-1151.

109. Gao, Y., Cao, E., Julius, D. and Cheng, Y. (2016) TRPV1 structures in nanodiscs reveal mechanisms of ligand and lipid action. *Nature*, advance online publication.

110. Kostyuchenko, V.A., Lim, E.X., Zhang, S., Fibriansah, G., Ng, T.S., Ooi, J.S., Shi, J. and Lok, S.M. (2016) Structure of the thermally stable Zika virus. *Nature*, **533**, 425-428.

111. He, Y., Yan, C., Fang, J., Inouye, C., Tjian, R., Ivanov, I. and Nogales, E. (2016) Near-atomic resolution visualization of human transcription promoter opening. *Nature*, **533**, 359-365.

112. Kostyuchenko, V.A., Chew, P.L., Ng, T.S. and Lok, S.M. (2014) Near-Atomic Resolution Cryo-Electron Microscopic Structure of Dengue Serotype 4 Virus. *J Virol*, **88**, 477-482.

113. Veesler, D., Ng, T.S., Sendamarai, A.K., Eilers, B.J., Lawrence, C.M., Lok, S.M., Young, M.J., Johnson, J.E. and Fu, C.Y. (2013) Atomic structure of the 75 MDa extremophile Sulfolobus turreted icosahedral virus determined by CryoEM and X-ray crystallography. *P Natl Acad Sci USA*, **110**, 5504-5509.

Chapter 2 Dynamical features of the *Plasmodium falciparum* ribosome during translation

This chapter is a paper published in *Nucleic Acids Research*, Ming Sun, Wen Li, Karin Blomqvist, Yaser Hashem, Sanchaita Das, Jeffrey Dvorin and Joachim Frank. “Dynamical features of the *Plasmodium falciparum* ribosome during translation”, *Nucleic Acids Res*. 2015 43: 10515-10524.

Published online 1 October 2015 *Nucleic Acids Research, 2015, Vol. 43, No. 21* ***10515–10524***
doi: 10.1093/nar/gkv991

Dynamical features of the *Plasmodium falciparum* ribosome during translation

Ming Sun[1], Wen Li[2], Karin Blomqvist[3,4,5], Sanchaita Das[6], Yaser Hashem[7], Jeffrey D. Dvorin[3,4,*] and Joachim Frank[1,2,8,*]

[1]Department of Biological Sciences, Columbia University, New York, NY 10027, USA, [2]Department of Biochemistry and Molecular Biophysics, Columbia University, New York, NY 10032, USA, [3]Division of Infectious Diseases, Boston Children's Hospital, Boston, MA 02115, USA, [4]Department of Pediatrics, Harvard Medical School, Boston, MA 02115, USA, [5]Department of Microbiology, Tumor and Cell Biology, Karolinska Institutet, 171 77 Stockholm, Sweden, [6]Program in Molecular Medicine, University of Massachusetts Medical School, Worcester, MA 01605, USA, [7]CNRS, Architecture et Réactivité de l'ARN, Université de Strasbourg, Strasbourg 67084, France and [8]Howard Hughes Medical Institute, Columbia University, New York, NY 10032, USA

Received July 24, 2015; Revised September 16, 2015; Accepted September 19, 2015

ABSTRACT

***Plasmodium falciparum*, the mosquito-transmitted *Apicomplexan* parasite, causes the most severe form of human malaria. In the asexual blood-stage, the parasite resides within erythrocytes where it proliferates, multiplies and finally spreads to new erythrocytes. Development of drugs targeting the ribosome, the site of protein synthesis, requires specific knowledge of its structure and work cycle, and, critically, the ways they differ from those in the human host. Here, we present five cryo-electron microscopy (cryo-EM) reconstructions of ribosomes purified from *P. falciparum* blood-stage schizonts at sub-nanometer resolution. Atomic models were built from these density maps by flexible fitting. Significantly, our study has taken advantage of new capabilities of cryo-EM, in visualizing several structures coexisting in the sample at once, at a resolution sufficient for building atomic models. We have discovered structural and dynamic features that differentiate the ribosomes of *P. falciparum* from those of mammalian system. Prompted by the absence of RACK1 on the ribosome in our and an earlier study we confirmed that RACK1 does not specifically co-purify with the 80S fraction in schizonts. More extensive studies, using cryo-EM methodology, of translation in the parasite will provide structural knowledge that may lead to development of novel anti-malarials.**

INTRODUCTION

Plasmodium falciparum is the mosquito-transmitted *Apicomplexan* parasite that causes the most severe form of human malaria. All of the human malaria species require two different hosts to complete their life cycle: humans and mosquitoes. Following inoculation of the human host by an infected mosquito, the parasite travels to the liver where it differentiates into the blood-invasive form. The exponential amplification of this asexual blood-stage form of the parasite results in all of the clinical symptoms of malaria. During the asexual blood-stage, the young parasites mature from the ring to the trophozoite stage, and then mature into schizonts, which eventually rupture and release 16–32 daughter merozoites. Some of the released merozoites will invade fresh erythrocytes, continuing the asexual life cycle, and some will differentiate into sexual transmission forms, that are taken up by a female mosquito during a blood meal (1).

There is an urgent need to identify novel drug targets and develop more effective antimalarial drugs. Resistance has developed in the parasite to all anti-malarials currently in large-scale clinical use. One promising avenue of research is suggested by the success of a few antibiotics which inhibit protein synthesis in the parasites. However, our knowledge of the *Plasmodium* ribosome, specifically as a target for antibiotics, remains incomplete.

The ribosome, a ribonucleoprotein complex formed by two subunits, has an overall conserved core structure consisting of the decoding center, the GTPase center and the peptidyl transferase center. It has three binding sites for tRNAs, the aminoacyl (A) site, peptidyl (P) site, and exit (E) site. The ribosome actively synthesizes proteins in multiple rounds of the translation elongation cycle as dictated by the

*To whom correspondence should be addressed. Tel: +1 212 305 9512; Fax: +1 212 305 9500; Email: jf2192@cumc.columbia.edu
Correspondence should also be addressed to Dr Jeffrey D. Dvorin. Tel: +1 617 919 2900; Fax: +1 617 730 0255; Email: jeffrey.dvorin@childrens.harvard.edu

mRNA, entailing the binding of aminoacyl-tRNA to the A site (decoding), transfer of the nascent peptide chain from the tRNA at the P site to the aminoacyl group on the A-site tRNA (peptide bond formation) and movement of tRNAs and mRNA by one codon (translocation). The process of translocation is facilitated by large-scale conformational changes in the ribosome, as it equilibrates between two conformations, termed 'rotated' and 'nonrotated', distinguished by a ≈5- to ≈9-degree rotation between the two subunits (intersubunit rotation) (2–4).

The recently published cryo-EM structure of *P. falciparum* schizont-stage ribosome (5) identified additional *P. falciparum*-specific ribosomal proteins, ribosomal RNA expansion segments, and *P. falciparum*-specific inter-subunit bridges, as compared with ribosomes from yeast and human. However, the dynamic behavior of *P. falciparum* ribosomes, of critical importance for understanding the molecular mechanism of parasite translation, has remained uncharacterized. Here, we used advanced techniques of cryo-EM to image schizont-stage *P. falciparum* 80S ribosome complexes in several conformational states. These different states are distinguished mainly by a combination of intersubunit rotation and differences in tRNA occupancies/positions. We were also able to provide complete models of tertiary structures of helix 16 and expansion segments ES10S and ES6BS, highly flexible regions in the ribosome of *P. falciparum*.

These findings provide rich insights into the dynamics of the *P. falciparum* ribosome during the schizont-stage translation elongation process and reveal important differences from the mammalian system. In addition, our results confirm the finding of Wong *et al.* (5) reporting the absence of RACK1. We performed co-purification experiments which indicated that indeed RACK1 does not specifically co-purify with the 80S fraction, suggesting that RACK1's presence on the ribosome is not essential for translation.

MATERIALS AND METHODS

Isolation and purification of *P. falciparum* ribosomes

P. falciparum parasites (3D7 strain) were cultured in human red blood cells under standard conditions (6). Schizont-stage parasites were released from host cells by treatment with 0.15% Saponin (Sigma). Purified parasites were re-suspended in lysis buffer (50 mM Tris–HCl, pH = 7.4; 100 mM KOAc; 7 mM $Mg(OAc)_2$; 380 mM sucrose; 6.5 mM β-mercaptoethanol; 0.14% vol/vol Triton X-100; 15 mM leupeptin and half a protease inhibitor cocktail tablet (Roche, EDTA-free)). Cells were disrupted using 0.5 mm glass beads (Sigma) and further clarified by short centrifugation. The ribosome-enriched pellets were obtained by overnight centrifugation (7) and further purified using 20K PEG precipitation methods described previously (7), with slight modifications. The final pellets were suspended in Buffer G (7) and kept at −80°C for further use.

Co-purification experiments

Ribosomes were isolated from late-stage *P. falciparum* according to the protocol published in Bunnik *et al.* (8). Immunoblot analysis of PfRACK1-HA was performed with αHA antibody (dilution 1:1000. Pierce). Immunoblot analysis of ribosome proteins were performed with αPfP0 (1E5F4) and αPfP2 (E2G12) monoclonals (dilution 1:500), generously provided by Dr Shobhona Sharma.

Electron microscopy

Four microliters of purified ribosomes were applied to holey carbon grids (carbon-coated Quantifoil R2/4 grid, Quantifoil Micro Tools, GmbH, Großlöbichau, Germany) containing an additional continuous thin layer of carbon, glow-discharged using Gatan Solarus 950 (9). Grids were blotted for 4 s at 4°C in 100% humidity and vitrified by plunging into liquid ethane cooled with liquid nitrogen, using the Mark IV Vitrobot (FEI, Hillsboro, Oregon) (10). Data were collected on a TF30 Polara electron microscope (FEI, Hillsboro, Oregon) operating at 300 kV, set up with a K2 Summit direct electron detection camera (Gatan, Warrendale, PA). Images were recorded using the automated data collection system Leginon (11) in counting mode, and taken at the nominal magnification of 23 000x, corresponding to a calibrated pixel size of 1.66 Å. The dose rate was nominally set to 8 electron counts per physical pixel per second (12) and the total exposure time was 8 s. Image stacks were collected in a defocus range of −1.5 μm to −3.5 μm, fractionated into 20 frames, each with an exposure time of 0.4 s.

Image processing

The dose-fractionated image stacks were first corrected for beam-induced motion, using the method of Li *et al.* (13), and averages of all 20 frames were used for image processing. A total number of 329K particles were automatically extracted from 5734 selected averaged images, using the ara-autopick and ara-crop tools in Arachnid (14), a python-encapsulated version of SPIDER. Contrast transfer function parameters were estimated using CTFFIND3 (15), and 3D classification was performed in RELION 1.2 (16), to discard defective particles and identify structurally homogeneous subsets.

Initial RELION 3D classification, with K = 10 classes and an angular sampling of 1.8°, yielded mainly three classes: rotated 80S ('rt80S' for brevity) with A/P and P/E tRNAs (22 793), slightly rotated 80S without tRNAs (27 158), and non-rotated 80S ribosomes (197 536). The largest class, of non-rotated ribosomes, was refined using the automated refinement procedure in RELION. This refinement resulted in a 4.4 Å ('gold standard' protocol with FSC = 0.143 criterion; b-factor of 176.1) density map, showing fragmented densities in the E-tRNA binding site, indicative of remaining heterogeneity. A subsequent second-stage RELION 3D classification was performed on this largest class, using K = 10 classes, a final angular sampling of 0.5° and combined local searches around the refined orientations. This classification resulted in four structurally distinct classes, non-rotated 80S ('nrt80S' for brevity) with E-tRNA (96 732), nrt80S with P-tRNA (14 696), nrt80S with P/P and E/E tRNAs (14 676), and nrt80S without any tRNAs (32 246). RELION auto-refinement was performed on each of these classes, as well as rt80S, yielding density maps of (i) rt80S with A/P-P/E tRNAs at average resolution of 5.8 Å

(b-factor 202.4), (ii) nrt80S with E-tRNA at 4.7 Å (b-factor 157.7), (iii) nrt80S with P-tRNA at 6.7 Å (b-factor 311.1), (iv) nrt80S with P/P and E/E tRNAs at 6.7 Å (b-factor 300.4), and (v) nrt80S without tRNAs at 5.1 Å (b-factor 184.1) (Supplementary Figure S1). To further improve the resolution and correct the local beam-induced movement, the RELION statistical movie processing method (17) was applied to the class of nrt80S with E-tRNA. It was run with averages of 5 movie frames; a standard deviation of 1° for the prior on the Euler angles; and a standard deviation of 1 pixel for the translation. This step yielded the density maps of nrt80S with E-tRNA to an average resolution of 4.2 Å (b-factor 264.1) (Supplementary Figure S1).

Additionally, focused refinements were performed on the class of nrt80S with E-tRNA, where either 40S subunit or 60S subunit was masked out. This step gave slightly improved density for the 40S subunit, with an average resolution of 4.9 Å, and the 60S subunit, with an average resolution of 4.6 Å. However, in terms of structural definition at the interface of the subunits, the gain was minimal. Thus, for further analysis, we focused on the five density maps from RELION auto-refinements and used Wong *et al.*'s maps (5) as the reference.

Resolutions reported were based throughout on the 'gold standard' protocol along with the FSC = 0.143 criterion, and involved soft masking and high-resolution noise substitution (19). For the final visualization, all density maps were corrected for the effects of a soft mask in RELION post-processing (16,18), and sharpened by application of an automatically estimated negative b-factor (18). Local resolutions were all measured using the ResMap software (19).

Model building by molecular dynamic flexible fitting

An atomic model was built for the nrt80S E-tRNA complex starting from the published models for the *P. falciparum* 40S and 60S ribosomal subunits (5) (PDB codes: 3J79, 3J7A). Since the published models of the *P. falciparum* 40S and 60S subunits were refined separately, their interface contains elements that violate stereochemistry. We found a large number of spatial clashes when we attempted to put the 40S and 60S models together as a full 80S model. We first resolved the clashes manually, and then applied MDFF flexible fitting to generate the complete structure of the 80S from *P. falciparum*. (For details on major clashes see Supplementary Figure S6 and Table S2).

More specifically, we fitted the structures of the 40S and the 60S subunits into the segmented maps of the nrt80S-E ribosome using the molecular dynamics flexible fitting program MDFF (20). The E-site tRNA from PDB 3J7A was also fitted into the segmented map. The initial system was prepared for MDFF (20) using Visual Molecular Dynamics (VMD) (21) and run in the NAMD program (22) for 0.5 ns of simulation time. Details of the simulation are as follows: Each of these fittings was run for a length of 0.5 ns, which stabilized the structures to closely match the maps. These runs removed most of the initial clashes, and the remaining ones were removed manually. The fitted structures of the 40S, 60S and E-site tRNA were then combined for a collective fitting of the map of the nrt80S E-tRNA complex. All of the runs used the generalized-Born implicit solvent model, as implemented in NAMD (22).

The above fitted structure for the nrt80S E-tRNA complex was used as the starting model for modeling for three maps: nrt80S-P, nrt80S, and rt80S-A/P-P/E. For the nrt80S P-tRNA complex, the X-ray structure of the P-tRNA (PDB 2WRI) was fitted into the current segmented map, then the fitted structure was combined with the structure of the 80S ribosome. For the map of the empty ribosome, the E-site tRNA was simply removed from the fitted structure for the nrt80S E-tRNA complex. For the rt80S-A/P-P/E complex, the structures for the two subunits had to be fitted separately, due to the large conformational changes relative to the nrt80S E-tRNA complex. Additionally, the density for the A/P tRNA is quite weak, and thus, at the current stage, we had to leave out the A/P tRNA in the MDFF modeling of the rt80S-A/P-P/E complex. The map for the P/E-site tRNA was fitted using the existing model (PDB 3J0Z), then the fitted P/E-site tRNA structure was combined with the fitted structure for the rotated 80S ribosome to generate the final structure of the rt80S-P/E complex. The final product fitting for each map ran 0.5 ns, which was followed by 5000 steps of energy minimization.

Modeling of RNA expansion segments

We used the 3dRNA webserver (http://biophy.hust.edu.cn/3dRNA/3dRNA.html) (23) to predict the three-dimensional structures of RNA expansion segments, ES10S and ES6BS of 40S subunit, and helix 16 (h16) of 18S rRNA.

The identification of ES10S, ES6BS and h16 sequences were based on Wong *et al.*'s work, PDB 3J7A (chain A) (5). The secondary structures were predicted using the RNAfold webserver (http://rna.tbi.univie.ac.at/cgi-bin/RNAfold.cgi) with default settings (24). RNAfold returned a minimum free-energy secondary structure and an optimal thermodynamic ensemble secondary structure. These two predictions led to the same secondary structure in our target regions, and match with the structure obtained by Wong *et al.* (5). Thus this secondary structure was deemed quite suitable as the input for tertiary structure building. Specifically, the inputs for ES10S were (i) the RNA sequence, UAUGCUUAUAUUUGUAUCUUUGAUGCUUAUAUUUUGCAUA, and (ii) the RNA secondary structure, ((((..((((..(((((…)))))..))))…)))))). The inputs for ES6BS were (i) the RNA sequence, AAAUCCCCACUUUUGCUUUUGCUUUUUUUGGGGAUUU, and (ii) the RNA secondary structure, (((((((((…..((….)).……))))))))). The inputs for h16 were, (i) RNA sequence, UGCAAGGCCAAUUUUUGGUUUUGUA, and (ii) the RNA secondary structure, ((((((((((…))))))))))).

The program 3dRNA generated ten models for each expansion segment. In order to select a good model for further analysis, we rigid-body fitted each of these models into the segmented map of nrt80S-P using UCSF Chimera (25), and chose the one that had the highest cross-correlation (CC) value (details see Supplementary Figure S5 and Table S1). In addition to the rigid-body fitting, we attempted to do flexible fitting using MDFF. However, since the density in

these regions is scattered, MDFF was not able to place the model into the map accurately.

For helix 16, the ten models generated by 3dRNA differed from one another only in the orientation of the hairpin tip region (for details, see Supplementary Figure S5). Rigid-body fitting the model into the map gave similar CC values, ranging from 0.82 to 0.835, and the one with highest CC value, 0.835, was selected. For ES6BS, the ten predicted models clustered into two major groups, differing in the orientation of the tip part: in one group the tip is bent outward to the 40S body, and in the other it is bent more inward (for details, see Supplementary Figure S5). The group that is closer to the 40S body has overall higher CC values, 0.76 to 0.77, as compared with 0.71 to 0.72 of the other group. The model with highest CC value, 0.77, was selected. For ES10S, due to the intrinsic flexibilities of ES10S and the 40S head region, the density is very weak and does not fully cover the predicted models. Hence the overall CC values are lower, as compared with ES6BS and h16, ranging from 0.56 to 0.66. The one with the highest CC, 0.66, was selected.

RESULTS

Cryo-EM reconstructions of schizont-stage *P. falciparum* 80S ribosomes

Synchronized *P. falciparum* parasites were harvested at the schizont-stage, the last stage of the erythrocytic cycle during which there is a proliferation of free ribosomes. To preserve the functional states as much as possible, we used a similar buffer as the one for an *in vitro* translation system (26), with relatively low salt concentration, and following standard ribosome purification procedures with slight modification (details described in 'Materials and Methods').

The purified sample was imaged using the TF30 Polara electron microscope (FEI, Hillsboro, Oregon), set up with a GATAN K2 Summit direct electron detector camera (Gatan, Warrendale, PA) in the single-electron counting mode. The dose-fractionated image stacks were first corrected for beam-induced motion, using the method of Li *et al.* (13). A total number of ≈329k particles were automatically extracted from 5734 selected averaged images. A two-step unsupervised 3D classification using RELION (16) was performed to discard defective particles and identify structurally homogeneous subsets, and auto-refinement was followed to further improve the resolution.

In the first step, we identified two main states of the 80S ribosomes, distinguished by intersubunit rotation and termed rotated (rt80S) and nonrotated (nrt80S). However, the reconstruction of the nrt80S still showed fragmented densities in the mRNA channel, indicative of remaining heterogeneity. A subsequent exhaustive 3D classification and 'focused' classification were performed to resolve this remaining heterogeneity.

In all, five major classes were identified: (i) rt80S bound with hybrid A/P and P/E tRNAs ('rt80S-A/P-P/E'), (ii) nrt80S bound with E-tRNA ('nrt80S-E'), (iii) nrt 80S bound with P-tRNA ('nrt80S-P'), (iv) nrt80S bound with P/P and E/E tRNAs ('nrt80S-P-E'), and (v) nrt80S without any tRNAs. The average resolutions of the density maps reconstructed from these classes ranged from 4.6 Å to 6.7 Å (FSC = 0.143; 'gold-standard' protocol) (Figure 1 and Supplementary Figure S1). Atomic models were built by flexible fitting based on the published structure of the *P. falciparum* ribosome (5). Specifically, for further biological analysis, we will discount complexes that contain no tRNAs (Figure 1D), as they would represent non-translating ribosomes.

As for the rotated *P. falciparum* 80S ribosome bound with two hybrid-state tRNAs, the 40S subunit displays a ≈9° counterclockwise rotation (when viewed from the solvent side of the 40S subunit) of the body relative to the 60S subunit (Figure 2C and D), and a moderate back-swiveling of the head (i.e. counterclockwise rotation when viewed from the top) by about 2 degrees, compared with the nrt80S-P state. Concurrent with the 40S subunits movements, we also observe that the L1 stalk, a mobile region of 60S subunit, moves inward by about 42° as it goes from nrt80S-P to rt80S-A/P-P/E (for details, see Supplementary Figure S2).

We then analyzed this rotated state by comparing it with mammalian rotated PRE-state ribosomes in earlier studies by Budkevich *et al.* (4,27). This comparison shows a good overall agreement, particularly with respect to the locations of the tRNA binding sites. Thus, the rt80S-A/P-P/E complex can be assumed to represent the pretranslocational (PRE) state of *P. falciparum*, a state after peptidyl-transfer but before translocation.

Of the three tRNA-containing non-rotated states, the nrt80S-P (Figure 1B), and the nrt80S-P-E (Figure 1C), complexes are candidates for POST states of the *P. falciparum* ribosome. Comparison of these maps with those of published mammalian POST 80S complexes containing classically configured P- and E-tRNAs (27,28), indeed reveals good overall structural agreement. In particular, the P-tRNAs in our nrt80S-P and nrt80S-P-E complexes have the same position and configuration as the one in mammalian systems (27,28). In addition, we can characterize the spatial relationship between the 40S subunit and the 80S ribosome by the former's 'rolling' position, in reference to a motion discovered by Budkevich *et al.* (27) in which the small subunit rotates around its long axis. In the *P. falciparum* P-tRNA-containing nrt80S complexes the 40S subunit has the same 'unrolled' configuration (Figure 2B) as the mammalian POST-state complex (27), when compared with the mammalian PRE-classical state complexes (27).

In addition to the nrt80S-P and nrt80S-P-E complexes, we have a third well-populated non-rotated class, the nrt80S-E state (Figure 1A). It has overall good structural similarities with *P. falciparum* POST-like nrt80S-P state; however, with several exceptions. Specifically, comparison with the nrt80S-P complex shows that, in the nrt80S-E complex, the 40S subunit head displays a ≈6 degree back-swiveling rotation, and the L1 stalk has rotated toward the E site on the large ribosomal subunit by ≈30 degrees.

Dynamics of *P. falciparum* small 40S subunits

The recent study of the *P. falciparum* ribosome, in a state comparable to our nrt80S-E, provided a detailed analysis of the *P. falciparum*- specific elements, including the large rRNA expansion segments (ESs) (5). Structurally, the rRNA ESs can be divided into two types. Expansion segments of one type are tightly associated with r-proteins or

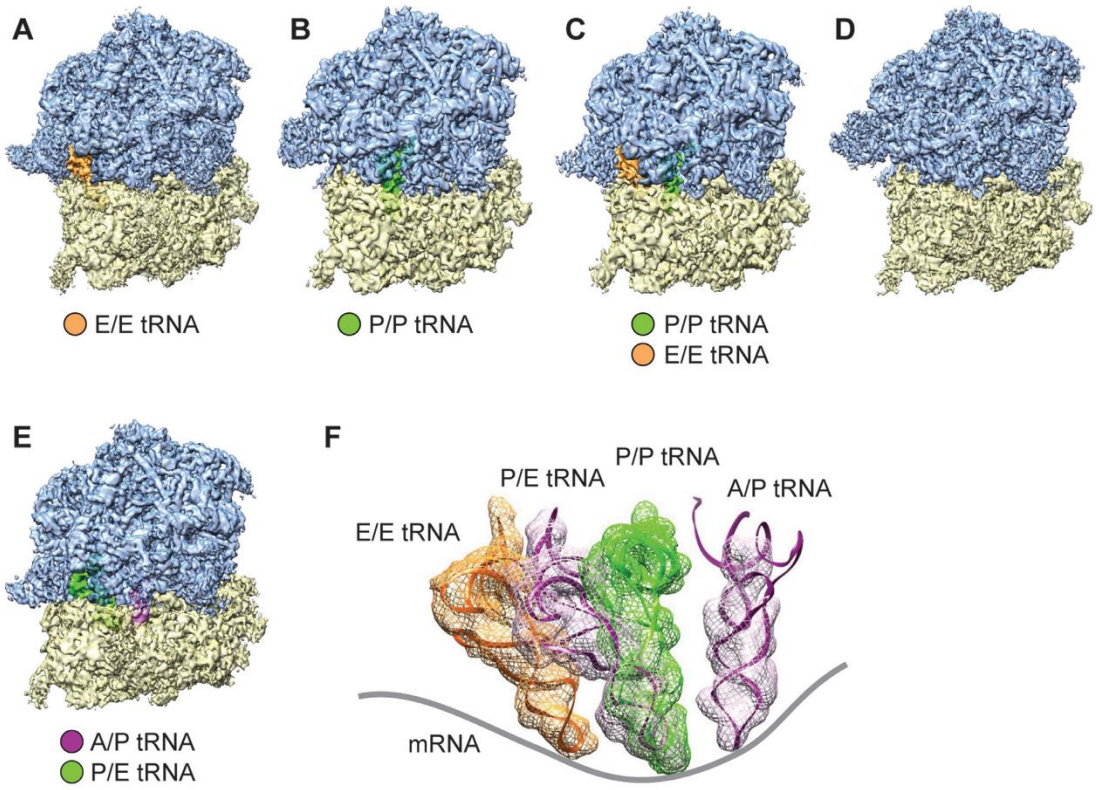

Figure 1. Cryo-EM reconstructions of *P. falciparum* 80S ribosomes obtained by classification. **(A–D)** Density maps of the *P. falciparum* 80S ribosome in non-rotated states (A) bound with E-tRNA (96 732 particles; 53.4%) at an average resolution of 4.7 Å; (B) bound with P-tRNA (14 696 particles; 8.1%) at 6.7 Å; (C) bound with P/P- and E/E-tRNAs (14 676 particles; 8.1%) at 6.7 Å; and (D) without tRNAs (32 246 particles; 17.8%) 5.1 Å. **(E)** rotated state (22 793 particles; 12.6%) at 5.8 Å resolution. 60S subunits are colored in blue and 40S subunits are in yellow. **(F)** Positions of tRNAs for all 80S complexes in (A)–(D). The structures of E-tRNA, P-tRNA and P/E-tRNA were obtained by MDFF fitting, and the structure of A/P-tRNA is from the existing model, PDB 3J0Z, rigid body-fitted into the segmented map in UCSF Chimera (25). Contours of cryo-EM densities are displayed in mesh; structures of tRNA are displayed as ribbons; and mRNA path has been added as cartoon.

other rRNA ESs, while the second type comprises long rRNA helices that are attached to the ribosome only at their bases, and the extended part can adopt different conformations, as in the case of ES10S and ES6S (for positions of the ESs on the *P. falciparum* 80S ribosome, see Supplementary Figure S3.).

Because of the intrinsic flexibilities of ES10S and ES6BS, their models were only partially built in the published structure (5) using model building tools adopted from X-ray crystallography. In our work we used a combination of different strategies to build complete models for ES10S and ES6BS. We identified the region of ES10S and ES6BS based on Wong *et al.*'s work (5) and used the 3dRNA software (23), an automated RNA tertiary structure-building program, to complete the tertiary structure of these components (for details, see Figure 3, Supplementary Figure S5 and 'Materials and Methods'). Both ES10S and ES6BS fulfill the requirements for application of the 3dRNA software as the length of these expansion segments is within the benchmarked length, and the secondary structures are known (5). Considering the good quality of cryo-EM map and the biologically functional meaning of the state, we chose to use the map of the nrt80S-P complex for further detailed analysis and model building.

ES10S. The most prominent *P. falciparum*-specific ES on 40S subunit is ES10S, which includes about 50 nucleotides and is located at the top of the 40S subunit head. (For details of modeling, see Figure 3C and Supplementary Figure S5 and 'Materials and Methods'). The optimal model was selected on account of its highest CC value against the segmented density. We attribute the fact that the tip part of the model is not fully covered by the density to the high flexibility of ES10S. A comparison between our nrt80S-P and rt80S-A/P-P/E density maps shows overall good agreement in the ES10S region (structural alignment on 40S subunits head region), indicating absence of significant conformational changes attributable to inter-subunit rotation.

Compared with some other well-known eukaryotes, *S. cerevisiae, T. brucei, T. cruzi, D. melanogaster and H. sapiens,* (7,29–31), the ES10S in *P. falciparum* is the largest one, both in terms of secondary structure and size of density visible in the cryo-EM density map. It is important to note that in *P. falciparum,* ES10S is expressed differently—in terms of length and secondary structures—at different life stages

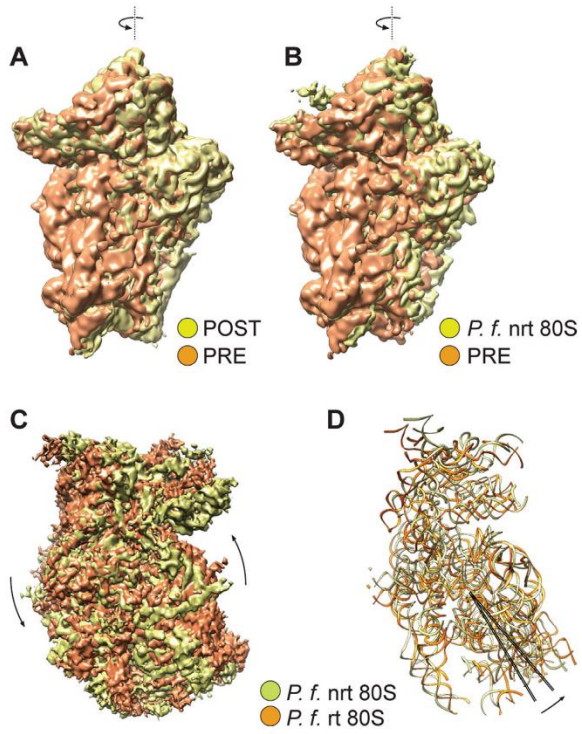

Figure 2. Global movements of *P. falciparum* 40S ribosomal subunits. **(A, B)** 'Subunit rolling' in POST states *P. falciparum* 80S. Comparison of the 40S subunit positions in POST state (yellow) (EMD 2621) with the PRE states (orange): (A) mammalian POST complex (data adapted from (27); EMD 2620), (B) *P. falciparum* P-tRNA bound POST 80S. **(C, D)** Inter-subunit rotation of 40S subunit in rotated PRE *P. falciparum* 80S ribosomes. (C) Cryo-EM maps of 40S subunit and (D) atomic models of 18S rRNA of 40S, in nrt80S-P (yellow) and rt80S-A/P-P/E (orange) states. The axes (black lines) were calculated in UCSF Chimera based on residues 1955–2033 of 18S rRNA (approximately h44 region). Crossing angle of the axes is ≈9°. Proteins are omitted for clarity. All comparisons were obtained by structural alignment on the 60S subunits of the 80S ribosomes using UCSF Chimera (25).

of the parasite, in mosquito and human hosts. This variation of ES10S in the parasite's different life stages and in different eukaryotes could indicate that ES10S possesses an extra *P. falciparum*-specific role in translation; for instance, it may recruit necessary translation factors via its long expanded helices. It is therefore quite likely ES10S has extra functions that are associated with the transition between two life stages in the development of the parasite.

ES6S. Another striking example of a large ES in *P. falciparum* is the ≈280 nucleotide long ES6S, which is located at the solvent side of the 40S subunit platform. According to the secondary-structure prediction (5), *P. falciparum* ES6S is formed by five helices, namely ES6AS, ES6BS, ES6CS, ES6DS and ES6ES. Particularly, ES6BS is located at the lower part of the 40S subunit body, close to left foot region. In this case, only the base region was modeled in Wong *et al.* (5), leaving a ≈40 nucleotides-long helix un-modeled. We completed the tertiary-structure model of ES6BS by using 3dRNA (23) (For details of modeling see Figure 3, Supplementary Figure S5, and 'Materials and Methods'). We rigid body-fitted the resulting models into the density map of nrt80S-P, and selected the one with highest cross-correlation value (for details, see Supplementary Figure S5). Still, the density is averaged out at the tip and does not fully cover the model, as a consequence of the flexibility of ES6BS. When going from the nrt80S-P to the rt80S-A/P-P/E state, ES6BS does not show conformational changes accompanying the inter-subunit rotation. In other words, ES6BS moves along rigidly with the 40S body region. For the other helices of ES6S, ES6AS, ES6CS, ES6DS and ES6ES, we used the Wong *et al.* model (5) to analyze the dynamics going from the nrt80S-P to the rt80S-A/P-P/E state, but we did not find significant local conformational changes in addition to the inter-subunit rotation.

It is tempting to speculate that the structural variation of ES6S reflects functional differences of eukaryotic translation among different species, and that the conformationally flexible regions may enable ES6S to recruit translation factors to the ribosome. In support of this idea, we note that the binding sites of eIF3 and eIF4G (31–33) to the 40S subunit are situated very close to the ES6S region

Helix 16. The helix16 (h16) of 18S rRNA is located between the 40S subunit's head and shoulder, and involved in the formation of the mRNA entry channel. Inspection of the sequences and structures of ribosomes from *S. cerevisiae* (PDB 4V88; ref 7), *P. falciparum* (PDB 3J79; ref 5), *D. melanogaster* (PDB 4V6W; ref 29) and *H. sapiens* (PDB 4V6X; ref 29) makes it highly likely that this helix is universally conserved among all eukaryotes. However, due to the intrinsic conformational flexibility, about 7 base pairs of h16 were not modeled in (5). Here, we have completed the modeling of h16 using 3dRNA (23) and rigid-body fitted the best model into our density map. Comparison among nrt80-P, nrt80S-E nrt80S-P-E and rt80S-A/P-P/E states shows that h16 in all these structures is bent toward protein uS3 in a similar manner without displaying additional conformation changes. Moreover, h16 adopts a similar conformation in Wong *et al.*'s study (5).

In addition, in the h16 area, we do not observe the stress-related protein stm1, which is often co-purified together with 80S ribosomes (7,29) and can inhibit translation. Stm1 binds to the head domain of the 40S subunit and prevents mRNA access by inserting an α-helix through the mRNA entry channel (7). The absence of stm1 in our present work supports the notion that the *P. falciparum* 80S complexes represent actively translating ribosomes.

The absence of RACK1 on *P. falciparum* 40S subunits

Another striking structural difference between the eukaryotic and parasite ribosome is the absence of RACK1 (receptor for activated kinase 1). RACK1, a key player in multiple signaling pathways (34), and a well-established component of the small ribosomal subunit in most eukaryotic ribosomes, is completely missing from its conserved binding sites. (For details see Supplementary Figure S4)

From yeast to mammalian ribosomes, RACK1 has a highly conserved binding site, interacting with ribosomal proteins eS17, uS3, and h39 and h40 of 18S rRNA (7,35–

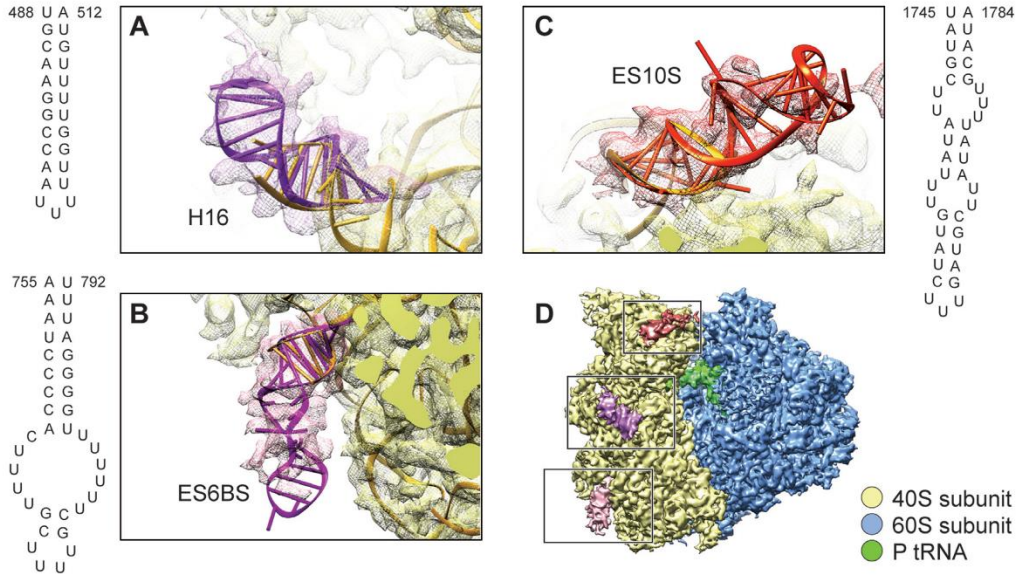

Figure 3. Predicted models of ES10S, ES6BS and helix 16 of *P. falciparum* 40S subunits using 3dRNA software. **(A–C)** Cryo-EM maps (meshed) and atomic models of **(A)** helix 16, **(B)** ES6BS and **(C)** ES10S. The secondary structures shown in (A-C) were predicted using RNAfold (24). The optimal tertiary structures shown in (A-C) were predicted using 3dRNA (23) and rigid-body fitted into density maps in UCSF Chimera (25). **(D)** Cryo-EM map of nrt80S-P. ES10S, ES6BS and h16 are highlighted in colors. 40S subunit is colored in yellow and 60S subunit is in blue.

38). Notably, both in our work and in Wong *et al.*'s results (5), RACK1 is completely missing in all maps, and its interacting partners in other species, proteins eS17 and uS3, exhibit weak densities, indicative of flexibility.

To further investigate the unusual behavior of RACK1 (PF3D7_0826700) in *P. falciparum*, we performed co-purification experiments to detect any physiological interaction between RACK1 and ribosomes. Our results show that RACK1 is expressed throughout the asexual life cycle, including the schizont stage. However RACK1 did not specifically co-purify in the fractions of isolated ribosomes from late-stage parasites and the majority of RACK1 was found in the unbound fractions (Figure 4). These results suggest that RACK1 mainly functions in a ribosome-unbound, free state in *P. falciparum* during the blood-stage, which would point to differences in translational regulation between the human host and the evolutionary divergent parasite (see Discussion for more details).

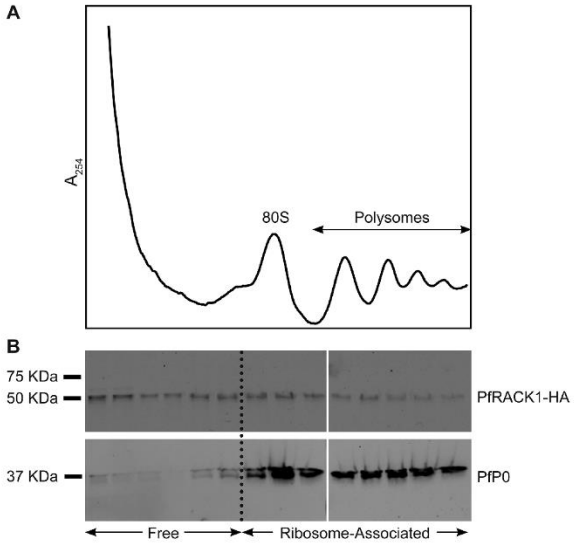

Figure 4. *P. falciparum* RACK1 does not specifically co-purify with isolated ribosomes from late-stage *P. falciparum* parasites. **(A)** Ribosome isolation profile, with monosome (80S) and polysome peaks indicated. **(B)** Western blots against PfRACK1-HA (50 kDa) and the ribosomal protein PfP0 (37 kDa) for the different fractions.

Structural rearrangements in the inter-subunit interface

The two ribosomal subunits are held together by a number of inter-subunit bridges, and the flexibility of these bridges facilitates the transition of the ribosome between the two main conformational states, rotated and nonrotated. As the dynamic behavior of the bridges is of great functional importance (3), we analyzed the way they are reconfigured during intersubunit rotation, in going from nrt80S-E (chosen for highest resolution) to rt80S-A/P-P/E in *P. falciparum*.

We found two distinct local movements which are effected by inter-subunit rearrangements. One involves the eukaryotic-specific inter-subunit bridge eB12, which is mainly formed by eL19 and ES6S (28,38), and the other is the *P. falciparum*-specific inter-subunit bridge which involves contacts between the C-terminal helix extension of protein eL8 and the C-terminal helix of protein eS1 (5) (for details see Figure 5).

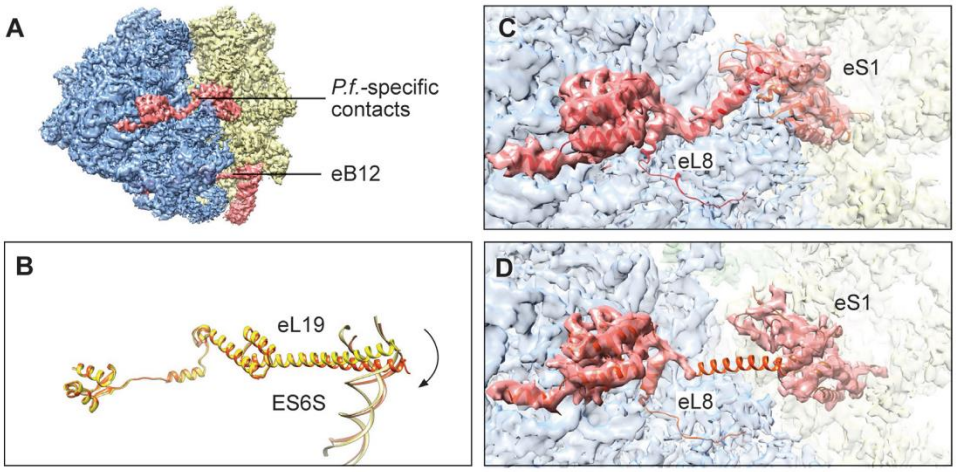

Figure 5. Structural re-arrangements of inter-subunit bridges. **(A)** Eukaryotic-specific bridge eB12 and *P. falciparum*-specific small bridge between eL8 and eS1 are shown in red. **(B)** The remarkably extended α-helix of eL19, in bridge eB12, is rotated by ≈17° in concert with the inter-subunit rotation (nonrotated state colored in yellow and rotated state in orange). Measurement was completed in UCSF Chimera (25). **(C, D)** The *P. falciparum*-specific small bridge is intact in nonrotated state (C), while it is broken in the rotated state (D). (In panels (C, D) density contours are displayed as transparency, and atomic models generated from MDFF are colored in red.)

Going from the *P. falciparum* nrt80S state to the rt80S-A/P-P/E state, the remarkably extended α-helix of eL19 (Figure 5A; B) rotates by ≈17° as it retains the integrity of the eB12 bridge. This persistency of eB12 in the dynamic ribosome was also observed in the human ribosome (28,38), indicating the evolutionary conservation of this feature between ribosomes from human malaria parasite and human host. Structural information on eB12 for any other eukaryotic ribosomes is not available at this time. The *P. falciparum*-specific bridge is found to be intact in all nrt80S complexes (nrt80S-E, nrt80S-P and nrt80S-P-E), but broken in the rt80S-A/P-P/E complex (for details, see Figure 5).

Besides the changes in the two inter-subunit bridges, we also noticed a lateral movement of h69 of 28S rRNA, which forms the core contacts in the interface area. Going from the POST nrt80S-P to the PRE rt80S-A/P-P/E state, h69 shifts as far as 6 Å toward to the E site, coupled with the inter-subunit rotation, such that bridge B2a stays intact. H69 has direct contacts with P-tRNA in the nrt80S complexes, but it loses these contacts when tRNA binds in the hybrid P/E site in the rt80S complexes. These movements are consistent with the one observed in the rotated 80S ribosome from yeast (2), but different from the one in the mammalian ribosome (27).

DISCUSSION

Structural models of the *P. falciparum* ribosome in different states

In our study of ribosomes purified from *Plasmodium falciparum* in the schizont stage, we found five subpopulations distinguished both by conformation and composition. In terms of conformation, we observe two main degrees of freedom, namely inter-subunit rotation and 40S head swivel movement. In terms of composition, we see tRNA in several combinations and binding positions. The resolution of the density maps reconstructed from these subpopulations was sufficient to obtain detailed atomic models of the ribosomal complexes based on recently published atomic models of the two ribosomal subunits. Importantly, we generated a full, stereochemically sound 80S ribosome model for each different state, by reconciling the special clashes of at subunit interface area and fitting the model into the map using MDFF.

At this point a general comment is in order. In cryo-EM of multi-component complexes such as the ribosome, which are subject to local conformational heterogeneity, the highest resolution can be often be gained by separate refinement of the individual components. It is inevitable that the individual structures obtained from these refinements are inconsistent along their interfaces. If the stated objective of these studies is the determination of the full structure, which will be of use for a large community of scholars who are not necessarily structural biologists, publication of separate structures of the individual components without reconciliation would seem to fall short of this objective, and 'repairs' of the kind we have undertaken here should not be necessary.

We also complemented the published atomic model by furnishing portions of the rRNA expansion segments ES6S and ES10S as well as h16 that were left incomplete. In the following discussion we first focus on the tRNA binding and the ribosomal movement. We then move on to a discussion of RACK1 and the possible significance of its absence on the *P. falciparum* ribosome.

Propensity for 40S head swiveling is dependent on the presence of P-site tRNA

We found a head swiveling movement that is dependent on the presence or absence of P-tRNA, but independent of

intersubunit rotation. Compared with the nrt80S-P complex, the 40S subunit head domain in the nrt80S-E complex is in the back-swiveled position. A similar movement was also observed by comparing nrt80S-P-E and nrt80S-E complexes. We analyzed the interaction between P-tRNA and the ribosome in detail. In the nrt80S-P complex, the P-tRNA has a direct interaction with uL5 P-site loop in its T-stem loop region, and has an additional tentative contact with protein eL44 of the 60S subunit. Also, there is a direct interaction of the P-tRNA acceptor stem and the PTC regions, especially around A3178, A3179, G2958 and G2959 regions (PDB 5AJ0, POST-state human ribosome (28), numbering A4358, A4359, G4158 and G4159 respectively). Thus, it is very likely that it is the extensive interactions between P-tRNA and ribosomal subunits which helps stabilizing the 40S subunit head region. Hence, while the presence of P-tRNA stabilizes the subunit head, its absence apparently enables the spontaneous (i.e. thermally driven) change of the head's position, independent of the intersubunit rotation.

The absence of RACK1

Many studies have established RACK1 as a key player in multiple signaling pathways, some of which connect signaling with the translation machinery (34,35,39–42). Surprisingly, RACK1 displays a dramatically different behavior in *P. falciparum* than other species, such as yeast and mammalian cells. From yeast (7,35,43) to mammalian cells (29,37), RACK1 or its counterpart cpc2 is a well-established component of the small ribosomal subunits. In contrast, it is absent from its conserved binding site on the small 40S subunit head in cryo-EM reconstructions both in our work and previous work (5), even at low density threshold settings (data not shown).

Early studies pointed out that RACK1 has both ribosome localization-dependent and -independent functions *in vivo* (34). Indeed, in *P. falciparum*, RACK1 is constitutively expressed throughout the asexual stage (44). Our co-purification experiments show that RACK1 is not specifically co-purified with the isolated ribosomes from late-stage parasites. The majority of RACK1 was detected in the unbound fractions, but some amount was also detected in the polysome fractions. One possibility is that it is the presence of RACK1, but not its strong and direct interaction with the ribosome, that is important for RACK1-mediated translation regulation in late blood-stage *P. falciparum*. Another possibility is that, on the contrary, its localization on the ribosome is necessary for translation regulation, but that at this life-stage of the organism the ratio of ribosome-bound to ribosome-unbound RACK1 could be modulated in response to the environmental changes, as reported for yeast (34). In this context it is also interesting that no typical Protein Kinase C ortholog, an important substrate of RACK1 in other systems, has been identified in *P. falciparum* (45).

In conclusion, we have confirmed that RACK1's absence on the ribosome is not a consequence of EM specimen preparation, but a reflection of weak binding on the 40S subunit in the late blood-stage of the organism. The implications of this finding for translation control at this stage warrant further exploration.

ACCESSION NUMBERS

The cryo-EM maps for rt80S-A/P-P/E, nrt80S-P and nrt80S-E have been deposited with the accession numbers EMD-6452, EMD-6456 and EMD-6454, respectively. The MDFF-fitted atomic models of rt80S-P/E, nrt80S-P and nrt80S-E have been deposited with the accession numbers 3JBO, 3JBN and 3JBP, respectively.

SUPPLEMENTARY DATA

Supplementary Data are available at NAR Online.

ACKNOWLEDGEMENTS

We thank Robert A. Grassucci for assistance with the data collection and Melissa Thomas-Baum for assistance with the preparation of the illustrations. We would like to thank Sjors Scheres and colleagues for making a preprint and coordinates of their structure available prior to publication of their paper (5). We thank Shobhona Sharma, Department of Biological Sciences, TIFR, Mumbai, India for sharing the anti-PfP0 and anti-PfP2 antibodies. We are also indebted to other members of the Frank lab for help and discussions, in particular Amedee des Georges, Harry Kao, Robert Langlois, and Danny Nam Ho.
Author contributions: M.S., Y.H., J.F. and J.D. designed the experiments. K.B. and J.D. prepared the biological samples and the co-purification experiments. M.S. and S.D. purified ribosomes. M.S. performed cryo-EM experiments, classification, 3D reconstructions, and refinement. W.L. and M.S. performed modeling and fitting. M.S., W.L., K.B., Y.H., J.F. and J.D. interpreted the results. M.S., J.D. and J.F. wrote the manuscript.

FUNDING

Howard Hughes Medical Institute and National Institutes of Health [R01 GM29169 to J.F.]; National Institutes of Health [R01 AI102907, DP2 AI112219 to J.D.]; Swedish Research Council: dnr 2013-367 [to K.B.]; LABEX: ANR-10-LABX-0036_NETRNA and the ANR grant @RAction program 'ANR CryoEM80S' [to Y.H.]. Funding for open access charge: Howard Hughes Medical Institute.
Conflict of interest statement. None declared.

REFERENCES

1. Haldar,K., Murphy,S.C., Milner,D.A. and Taylor,T.E. (2007) Malaria: Mechanisms of erythrocytic infection and pathological correlates of severe disease. *Annu. Rev. Pathol.-Mech.*, **2**, 217–249.
2. Svidritskiy,E., Brilot,A.F., Koh,C.S., Grigorieff,N. and Korostelev,A.A. (2014) Structures of yeast 80S ribosome-tRNA complexes in the rotated and nonrotated conformations. *Structure*, **22**, 1210–1218.
3. Spahn,C.M., Gomez-Lorenzo,M.G., Grassucci,R.A., Jorgensen,R., Andersen,G.R., Beckmann,R., Penczek,P.A., Ballesta,J.P. and Frank,J. (2004) Domain movements of elongation factor eEF2 and the eukaryotic 80S ribosome facilitate tRNA translocation. *EMBO J.*, **23**, 1008–1019.
4. Budkevich,T., Giesebrecht,J., Altman,R.B., Munro,J.B., Mielke,T., Nierhaus,K.H., Blanchard,S.C. and Spahn,C.M. (2011) Structure and dynamics of the mammalian ribosomal pretranslocation complex. *Mol. Cell*, **44**, 214–224.

5. Wong,W., Bai,X.C., Brown,A., Fernandez,I.S., Hanssen,E., Condron,M., Tan,Y.H., Baum,J. and Scheres,S.H. (2014) Cryo-EM structure of the *Plasmodium falciparum* 80S ribosome bound to the anti-protozoan drug emetine. *eLife*, **3**, e03080.
6. Trager,W. and Jensen,J.B. (2005) Human malaria parasites in continuous culture. *J. Parasitol.*, **91**, 484–486.
7. Ben-Shem,A., Garreau de Loubresse,N., Melnikov,S., Jenner,L., Yusupova,G. and Yusupov,M. (2011) The structure of the eukaryotic ribosome at 3.0 A resolution. *Science*, **334**, 1524–1529.
8. Bunnik,E.M., Chung,D.W.D., Hamilton,M., Ponts,N., Saraf,A., Prudhomme,J., Florens,L. and Le Roch,K.G. (2013) Polysome profiling reveals translational control of gene expression in the human malaria parasite *Plasmodium falciparum*. ,*Genome Biol.*, **14**, R128.
9. Grassucci,R.A., Taylor,D.J. and Frank,J. (2007) Preparation of macromolecular complexes for cryo-electron microscopy. *Nat. Protoc.*, **2**, 3239–3246.
10. Dubochet,J., Adrian,M., Chang,J.J., Homo,J.C., Lepault,J., Mcdowall,A.W. and Schultz,P. (1988) Cryo-Electron Microscopy of Vitrified Specimens. *Q. Rev. Biophys.*, **21**, 129–228.
11. Suloway,C., Pulokas,J., Fellmann,D., Cheng,A., Guerra,F., Quispe,J., Stagg,S., Potter,C.S. and Carragher,B. (2005) Automated molecular microscopy: the new Leginon system. *J. Struct. Biol.*, **151**, 41–60.
12. Liao,M.F., Cao,E.H., Julius,D. and Cheng,Y.F. (2013) Structure of the TRPV1 ion channel determined by electron cryo-microscopy. *Nature*, **504**, 107–112.
13. Li,X.M., Mooney,P., Zheng,S., Booth,C.R., Braunfeld,M.B., Gubbens,S., Agard,D.A. and Cheng,Y.F. (2013) Electron counting and beam-induced motion correction enable near-atomic-resolution single-particle cryo-EM. *Nat. Methods*, **10**, 584–590.
14. Langlois,R., Pallesen,J., Ash,J.T., Ho,D.N., Rubinstein,J.L. and Frank,J. (2014) Automated particle picking for low-contrast macromolecules in cryo-electron microscopy. *J. Struct. Biol.*, **186**, 1–7.
15. Mindell,J.A. and Grigorieff,N. (2003) Accurate determination of local defocus and specimen tilt in electron microscopy. *J. Struct. Biol.*, **142**, 334–347.
16. Scheres,S.H.W. (2012) RELION: Implementation of a Bayesian approach to cryo-EM structure determination. *J. Struct. Biol.*, **180**, 519–530.
17. Bai,X.C., Fernandez,I.S., McMullan,G. and Scheres,S.H.W. (2013) Ribosome structures to near-atomic resolution from thirty thousand cryo-EM particles. *eLife*, **2**, e00461.
18. Chen,S.X., McMullan,G., Faruqi,A.R., Murshudov,G.N., Short,J.M., Scheres,S.H.W. and Henderson,R. (2013) High-resolution noise substitution to measure overfitting and validate resolution in 3D structure determination by single particle electron cryomicroscopy. *Ultramicroscopy*, **135**, 24–35.
19. Kucukelbir,A., Sigworth,F.J. and Tagare,H.D. (2014) Quantifying the local resolution of cryo-EM density maps. *Nat. Methods*, **11**, 63–65.
20. Trabuco,L.G., Villa,E., Mitra,K., Frank,J. and Schulten,K. (2008) Flexible fitting of atomic structures into electron microscopy maps using molecular dynamics. *Structure*, **16**, 673–683.
21. Humphrey,W., Dalke,A. and Schulten,K. (1996) VMD: Visual molecular dynamics. *J. Mol. Graph. Model.*, **14**, 33–38.
22. Phillips,J.C., Braun,R., Wang,W., Gumbart,J., Tajkhorshid,E., Villa,E., Chipot,C., Skeel,R.D., Kale,L. and Schulten,K. (2005) Scalable molecular dynamics with NAMD. *J. Comput. Chem.*, **26**, 1781–1802.
23. Zhao,Y.J., Huang,Y.Y., Gong,Z., Wang,Y.J., Man,J.F. and Xiao,Y. (2012) Automated and fast building of three-dimensional RNA structures. *Sci Rep-Uk*, **2**, 734.
24. Lorenz,R., Bernhart,S.H., Honer Zu Siederdissen,C., Tafer,H., Flamm,C., Stadler,P.F. and Hofacker,I.L. (2011) ViennaRNA Package 2.0. *Algorithms Mol. Biol.*, **6**, 26.
25. Pettersen,E.F., Goddard,T.D., Huang,C.C., Couch,G.S., Greenblatt,D.M., Meng,E.C. and Ferrin,T.E. (2004) UCSF chimera - A visualization system for exploratory research and analysis. *J. Comput. Chem.*, **25**, 1605–1612.
26. Ferreras,A., Triana,L., Correia,H., Sanchez,E. and Herrera,F. (2000) An *in vitro* system from *Plasmodium falciparum* active in endogenous mRNA translation. *Mem. Inst Oswaldo Cruz*, **95**, 231–235.
27. Budkevich,T.V., Giesebrecht,J., Behrmann,E., Loerke,J., Ramrath,D.J., Mielke,T., Ismer,J., Hildebrand,P.W., Tung,C.S., Nierhaus,K.H. *et al.* (2014) Regulation of the mammalian elongation cycle by subunit rolling: a eukaryotic-specific ribosome rearrangement. *Cell*, **158**, 121–131.
28. Behrmann,E., Loerke,J., Budkevich,T.V., Yamamoto,K., Schmidt,A., Penczek,P.A., Vos,M.R., Burger,J., Mielke,T., Scheerer,P. *et al.* (2015) Structural snapshots of actively translating human ribosomes. *Cell*, **161**, 845–857.
29. Anger,A.M., Armache,J.P., Berninghausen,O., Habeck,M., Subklewe,M., Wilson,D.N. and Beckmann,R. (2013) Structures of the human and Drosophila 80S ribosome. *Nature*, **497**, 80–85.
30. Gao,H.X., Ayub,M.J., Levin,M.J. and Frank,J. (2005) The structure of the 80S ribosome from *Trypanosoma cruzi* reveals unique rRNA components. *Proc. Natl. Acad. Sci. U.S.A.*, **102**, 10206–10211.
31. Hashem,Y., des Georges,A., Fu,J., Buss,S.N., Jossinet,F., Jobe,A., Zhang,Q., Liao,H.Y., Grassucci,R.A., Bajaj,C. *et al.* (2013) High-resolution cryo-electron microscopy structure of the *Trypanosoma brucei* ribosome. *Nature*, **494**, 385–389.
32. Hashem,Y., des Georges,A., Dhote,V., Langlois,R., Liao,H.Y., Grassucci,R.A., Pestova,T.V., Hellen,C.U.T. and Frank,J. (2013) Hepatitis-C-virus-like internal ribosome entry sites displace eIF3 to gain access to the 40S subunit. *Nature*, **503**, 539–543.
33. Siridechadilok,B., Fraser,C.S., Hall,R.J., Doudna,J.A. and Nogales,E. (2005) Structural roles for human translation factor eIF3 in initiation of protein synthesis. *Science*, **310**, 1513–1515.
34. Coyle,S.M., Gilbert,W.V. and Doudna,J.A. (2009) Direct link between RACK1 function and localization at the ribosome *in vivo*. *Mol. Cell. Biol.*, **29**, 1626–1634.
35. Nilsson,J., Sengupta,J., Frank,J. and Nissen,P. (2004) Regulation of eukaryotic translation by the RACK1 protein: a platform for signalling molecules on the ribosome. *EMBO Rep.*, **5**, 1137–1141.
36. Adams,D.R., Ron,D. and Kiely,P.A. (2011) RACK1, A multifaceted scaffolding protein: Structure and function. *Cell Commun. Signal.*, **9**, 22.
37. Chandramouli,P., Topf,M., Menetret,J.F., Eswar,N., Cannone,J.J., Gutell,R.R., Sali,A. and Akey,C.W. (2008) Structure of the mammalian 80S ribosome at 8.7 angstrom resolution. *Structure*, **16**, 535–548.
38. Khatter,H., Myasnikov,A.G., Natchiar,S.K. and Klaholz,B.P. (2015) Structure of the human 80S ribosome. *Nature*, **520**, 640–645.
39. McLeod,M., Shor,B., Caporaso,A., Wang,W., Chen,H. and Hu,L. (2000) Cpc2, a fission yeast homologue of mammalian RACK1 protein, interacts with Ran1 (Pat1) kinase to regulate cell cycle progression and meiotic development. *Mol. Cell. Biol.*, **20**, 4016–4027.
40. Lu,H.C., Swindell,E.C., Sierralta,W.D., Eichele,G. and Thaller,C. (2001) Evidence for a role of protein kinase C in FGF signal transduction in the developing chick limb bud. *Development*, **128**, 2451–2460.
41. McCahill,A., Warwicker,J., Bolger,G.B., Houslay,M.D. and Yarwood,S.J. (2002) The RACK1 scaffold protein: A dynamic cog in cell response mechanisms. *Mol. Pharmacol.*, **62**, 1261–1273.
42. Ron,D. and Mochlyrosen,D. (1994) Agonists and antagonists of protein-kinase-C function, derived from its binding-proteins. *J. Biol. Chem.*, **269**, 21395–21398.
43. Yusupova,G. and Yusupov,M. (2014) High-resolution structure of the eukaryotic 80S ribosome. *Annu. Rev. Biochem.*, **83**, 467–486.
44. Madeira,L., DeMarco,R., Gazarini,M.L., Verjovski-Almeida,S. and Garcia,C.R.S. (2003) Human malaria parasites display a receptor for activated C kinase ortholog. *Biochem. Biophys. Res. Commun.*, **306**, 995–1001.
45. Sartorello,R., Amaya,M.J., Nathanson,M.H. and Garcia,C.R.S. (2009) The *plasmodium* receptor for activated C kinase protein inhibits Ca^{2+} signaling in mammalian cells. *Biochem. Biophys. Res. Commun.*, **389**, 586–592.

SUPPLEMENTARY

This file contains six supplementary figures and two supplementary tables.

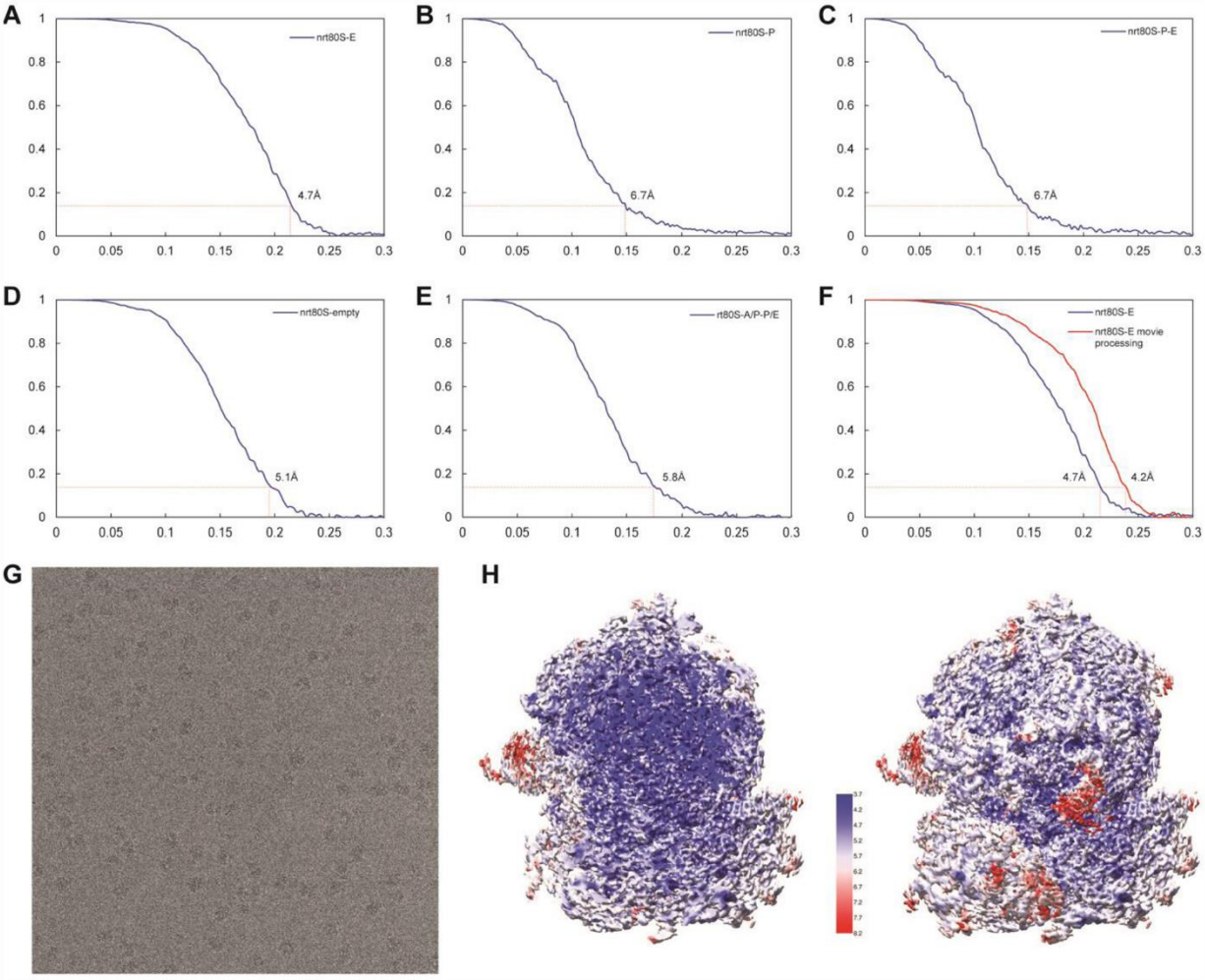

Supplementary figure 1. cryo-EM reconstruction of *P. falciparum* 80S complexes, related to Figure 1 (A-E) FSC curves for (A) nrt80S-E, (B) nrt80S-P, (C) nrt80S-P-E, (D) nrt80S-empty, and (E) rt80S-A/P-P/E state respectively. (F) FSC curves for nrt80S-E state complex, using RELION auto-refinement (blue) and statistical movie processing (red) methods. Resolutions reported were based on the "gold standard" protocol along with the FSC=0.143 criterion, and involved soft masking and high-resolution noise substitution (18). (G) Representative electron micrograph showing *P. falciparum* 80S particles. (H) Density map of nrt80S-E state after further statistical movie processing. Map is colored according to local resolution calculated from ResMap (19). Shown are the central slice and the front view of the map.

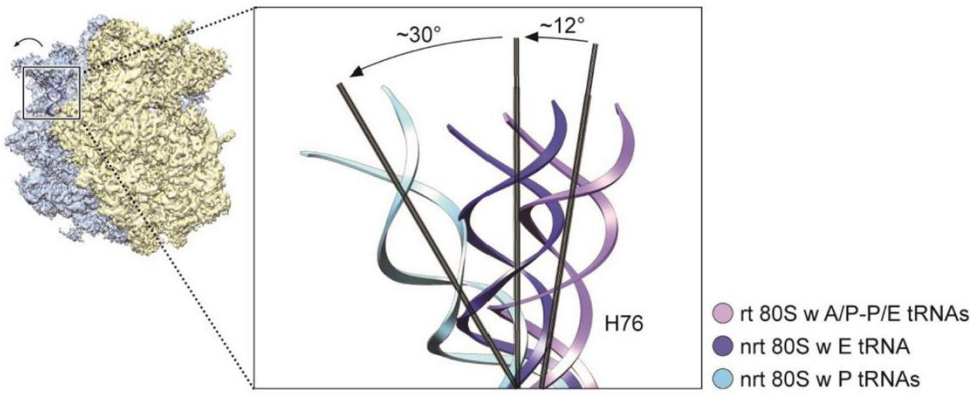

Supplementary figure 2. Movements of L1 stalk regions. A close-up view of the region boxed on the 80S ribosome (left) shows the relative movements of L1 stalk among the following states: (i) rt80S-A/P-P/E (purple), (ii) nrt80S-E (blue), and (iii) nrt80S-P (cyan). The model of each state was generated by using MDFF. Angles of rotation from (i) to (ii) and from (ii) to (iii) are indicated by arrows. The movements were measured by using UCSF Chimera (25), based on residues 2732-2747 and 2801-2817 of 28S rRNA (approximately H76, L1 stalk 318 region).

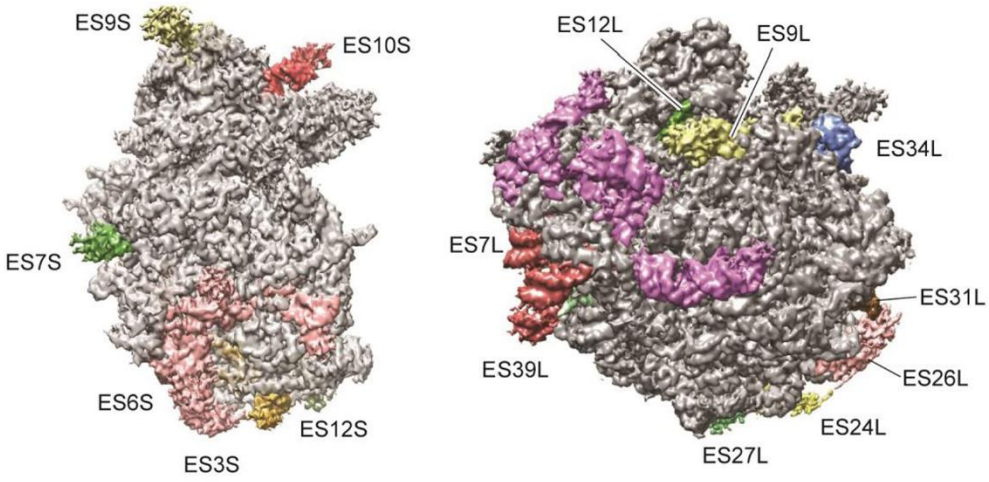

Supplementary figure 3. Positions of rRNA expansion segments on solvent sides of *P. falciparum* 40S (left) and 60S (right) subunits. The largest rRNA expansion segments (painted in various colors) were identified according to the most recent published models.

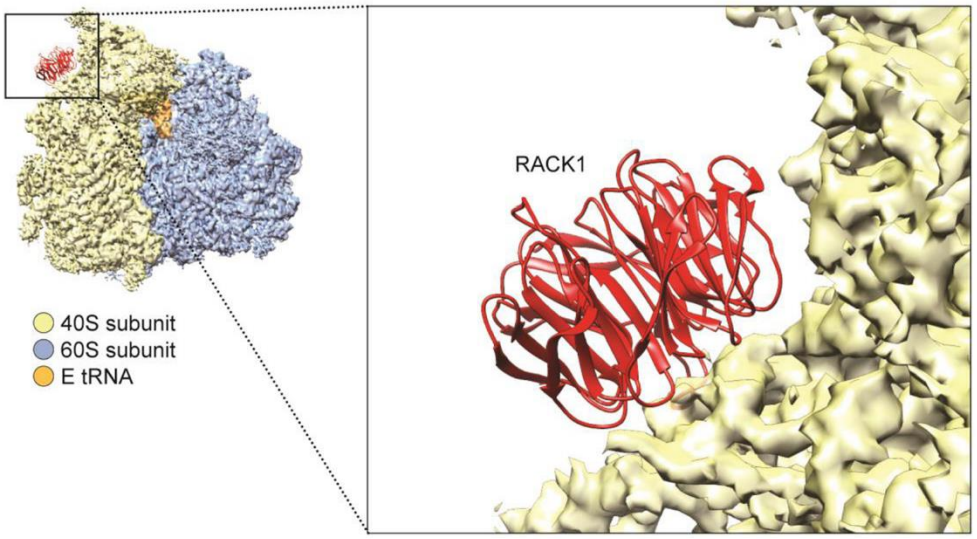

Supplementary figure 4. Absence of RACK1 on *P. falciparum* 40S subunits. Homology models of 40S crystal structure (PDB ID: 3U5B, 3U5C) (7) were rigid-body fitted using UCSF Chimera (25). Missing RACK1 protein is shown in red. 40S subunit is painted in yellow, 60S subunit in blue.

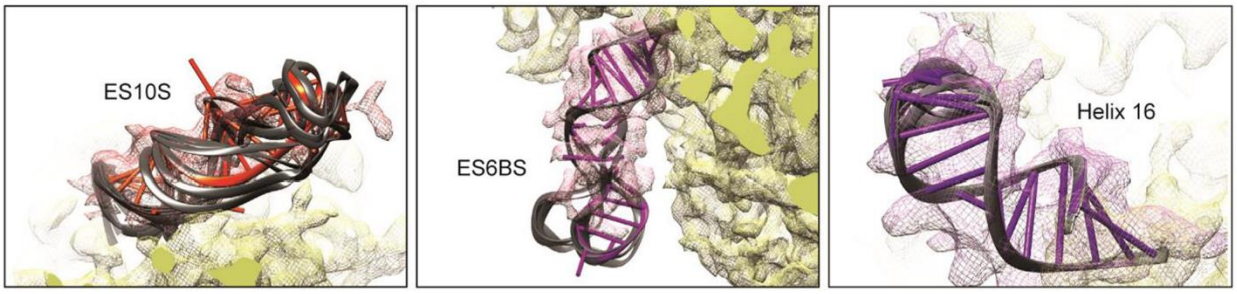

Supplementary figure 5. Predicted models for ES10S, ES6BS and helix 16 using the 3dRNA software. 10 predicted models generated from 3dRNA (26) were rigid fitted into nrt80S-P map (shows as mesh) using UCSF Chimera (25). The one with highest cross-correlation is highlighted in color: (A) ES10S, orange, (B) ES6BS, pink and (C) helix 16, purple. Lower-CC models are colored in grey.

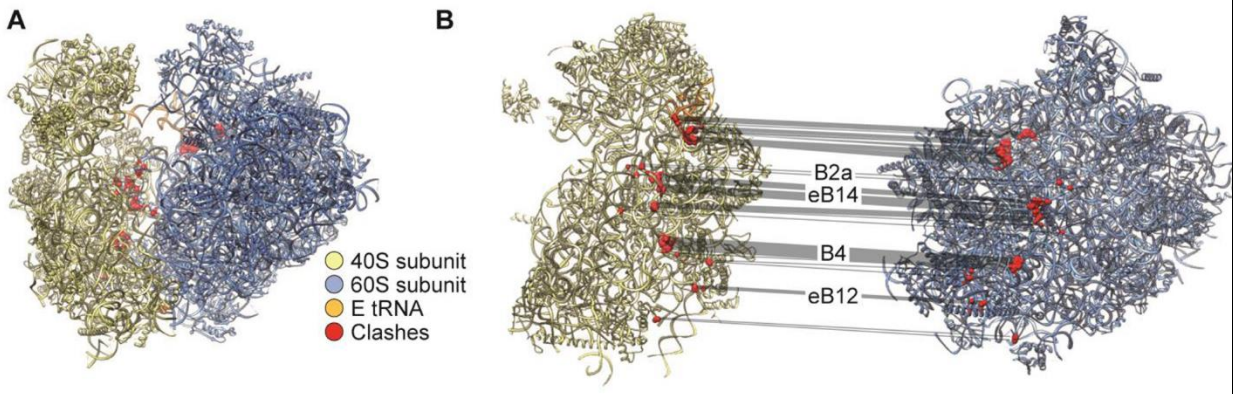

Supplementary figure 6. Major clashes at the inter-subunit interface of the published *P. falciparum* ribosome subunit models (5). The published models, PDB 3J79 and 3J7A, were saved as a single combined 80S molecule (no hydrogen atoms included) and then evaluated in UCSF Chimera (25). The identification of major clashes was based on VDW radii, using the default criteria in the 'Find Clashes/Contacts' function in UCSF Chimera, with cutoff value 0.6Å and allowance value 0.4Å. (A) Clash atoms at the interface are shown as spheres and colored in red. (B) Most of the contact atoms are clustered at the tRNA CCA end, bridge B2a, B4, and regions of eukaryotic-specific bridges eB14 and eB12 (see Suppl. Table 2). Pseudo-bonds between these contact atoms are colored in light grey. The inter-subunit bridges assignments are based on Ben-Shem *el al's* work (7).

Model number	ES10S	ES6BS	Helix 16
1	0.60	0.71	0.83
2	0.60	0.72	0.83
3	0.61	0.72	0.83
4	0.56	0.73	0.83
5	0.57	0.76	0.83
6	0.66	0.77	0.83
7	**0.66**	0.77	**0.84**
8	0.65	0.76	0.83
9	0.57	0.77	0.83
10	0.57	**0.77**	0.82

Supplementary table 1. Cross-correlations between 3dRNA-predicted and experimental cryo-EM density map for nrt80S-P. The predicted models were rigid-body fitted into the individual domains of the segmented nrt80S-P density map. The segmentation of nrt80S-P density map and measurement of cross-correlation (CC) were both done in UCSF Chimera (25). The highest CC values are highlighted in bold.

40S subunit (PDB 3J7A)	60S subunit (PDB 3J79)
18S rRNA (h20)	28S rRNA (h34)
18S rRNA (ES6ES)	eL19
18S rRNA (h27)	eL41
18S rRNA (h44)	28S rRNA (h69)
18S rRNA (h44)	eL41
18S rRNA (h45)	28S rRNA (h69)
18S rRNA (h45)	eL41
E-tRNA (CCA end)	28S rRNA (h68)
E-tRNA (CCA end)	28S rRNA (H88)
E-tRNA (CCA end)	eL44
uS15	28S rRNA (h34)
uS15	eL30
eS8	28S rRNA (h63)

Supplementary table 2. Major clashes at the inter-subunit interface of the published *P. falciparum* ribosome subunit models (5). The 256 contact atoms between the published *P. falciparum* 40S subunit and 60S subunit can be grouped into certain rRNA helices and proteins. For the identification of the contacts/clashes see Suppl. fig. 6. Zero contacts were found in the MDFF-fitted nrt80S-E, nrt80S-P and rt80S-P/E models. The assignment of the helices is based on the secondary structure in Wong *et al.*'s work (5).

Chapter 3 Changes in the structure of *Saccharomyces cerevisiae* ribosomes in response to carbon source shift

This chapter is a manuscript under preparation. Sun, M., Shen, B., Li, W., Samir, P., Link, A. and Frank, J. (2016). "Cryo-EM study of *S. cerevisiae* ribosomes in response to change in carbon source" (in-preparation).

3.1 Introduction

One of the fundamental challenges for cell physiology is understanding how balanced growth is achieved in the face of a complex and fluctuating environment which includes, for instance, fluctuations in temperature, nutrient availability, and physical forces (1). Unicellular organisms such as the yeast *Saccharomyces cerevisiae* have evolved autonomous mechanisms for adapting to drastic environmental changes. These mechanisms sense and respond to external changes through multiple interconnected signaling pathways, which often bring about changes in gene expression (2).

Nutrients, being among the most important environmental stimuli, can control the growth of cells at the level of both transcription and translation (3). Starvation for amino acids or purines is known to cause a general inhibition of translation as well as an activation of many genes involved in amino acid biosynthesis (4). Starvation for macro-nutrients, such as glucose, nitrogen or phosphorous, can cause cells to arrest growth and become quiescent, with reduced transcription and translation activities, and increased tolerance to stress (5). It has been shown that upon nutrient

repletion, yeast can immediately return to growth and division. Expression-profiling analysis of quiescent *S. cerevisiae* cells showed that at least 2,500 genes respond to glucose repletion within 5-10 min (6,7). Many of these glucose repletion-induced genes are involved in protein synthesis, post-translational modification, and mitochondrial functions (6,7).

In our studies, we are particularly interested in glucose since it is the preferred carbon source for *S. cerevisiae* growth and is an activator of numerous signaling pathways and changes in gene expression (8). Several well characterized signaling pathways have been previously identified, including the target of rapamycin (TOR), hexose transporter (HXT) induction, and the protein kinase A (PKA) pathways (4). These translationally mediated networks in *S. cerevisiae* collectively sense the level of glucose and initiate the cellular responses. On the molecular level, run-on transcription assays revealed that depletion of glucose induced reduction in the rates of transcription and the degradation of mRNAs (8). However, the majority of these responses appeared to regulate gene expressions at the transcriptional level.

Recent findings have showed that changes in the translational control occurs after nutrient changes. Ashe and coworkers performed polysome profiling experiments to investigate the effect of glucose depletion on translation activities (4). The authors found that glucose withdrawal results in a loss of polysomes and an increase in the abundance of 80S monosomes. This change in polysome profile was rapid and reversible. They also found that the cell's nutritional status altered the translational activity without affecting transcription (4).

The ribosome a macromolecular assembly composed of ribosomal proteins (r-proteins) and RNAs (rRNAs) performs protein synthesis in all living cells. It translates genetic information carried by mRNAs into polypeptide chains, which then folds into functional proteins. In eukaryotes, the ribosome is formed by two subunits 40S and 60S. The small eukaryotic 40S subunit consists

of the 18S rRNA and 32 r-proteins. It contains the messenger decoding center, which facilitates and monitors base-pairing between a codon of mRNA and the anticodon of the cognate tRNA (9). The large 60S subunit is comprised of three rRNAs, 28S rRNA, 5.8S rRNA and 5S rRNA, and 46 r-proteins. Its main functions are to catalyze peptide bond formation, provide the binding sites for the elongation factors and to serve as the conduit (exit tunnel) for the nascent peptide chain.

Traditionally, the ribosome has been considered a defined structure, capable of precisely accomplishing all steps of protein synthesis. However, evidence of ribosome heterogeneity at the level of ribosomal components and post-translational modifications, has been found across a variety of species (10-12). In bacteria, ribosomes that contain sequence-specific rRNAs facilitate the selective translation of leaderless mRNAs in stress response (13). In vertebrates, ribosomal proteins have been found to exhibit tissue-specific expression patterns (14,15). In *S. cerevisiae*, mass spectrometry analysis has shown the stoichiometry of r-proteins to be dependent on the source of carbon (16).

We have conducted studies on the yeast cell's adaption to different carbon sources. We replaced glucose, a fermentable carbon source, with glycerol, a non-fermentable carbon source, to induce a less optimal condition in the cell. Isobaric Tag for Relative and Absolute Quantitation (iTRAQ) methods, followed by multi-dimensional protein identification technology (MudPIT), were used to quantitatively monitor the steady-state proteome after the carbon source shift. A total of 379 proteins, many related to protein synthesis and translational control pathways, were found to be differentially expressed in response to a shift from glucose to glycerol (1).

To directly visualize the effect of carbon source switch on ribosomal compositions, we performed cryo-electron microscopy (cryo-EM) experiments on purified ribosomes in a time series. Notably, we obtained reconstructions of the 80S ribosomes at selected time points after the shift,

and observed that a fraction of ribosomes lacked densities for r-proteins, mainly eS1 (yeast rpS1) on the 40S subunit and uL16 (yeast rpL10) on the 60S subunit. We found that the binding of ratio of eS1 and uL16 to other ribosomal proteins also changed as a function of time, consistent with the change in translational activities as gauged by polysome profiling. On the basis of these observations, along with previous structural and genetics studies of the roles of eS1 (17) and uL16 (18), we propose that rapid control of translation is exerted through the dissociation of r-protein eS1/rpS1 and uL16/rpL10 from the ribosome. Our studies thus open a new venue on the exploration of *S. cerevisiae*'s rapid adaption to carbon source shifts at the level of translation.

3.2 Results

Yeast cell consumes fermentable carbon sources in preference to other carbon sources (3). In this study, *S. cerevisiae* cells were first grown in the rich medium with glucose (YP) to the mid-log phase and then shifted to rich medium with glycerol (YPG). Cells were harvested at the different time points after the shift, 0, 30, 120, 240, 450, and 1440 minutes and ribosomes were purified using standard methods. The T=0 min time point sample was harvested at the mid-log phase in glucose based on OD660 measurements.

Cryo-EM reconstructions of *S. cerevisiae* ribosomes

Initial cryo-EM study. Cryo-EM experiments were performed on the purified ribosomes after shifting yeast cells from glucose to glycerol, using an FEI Tecnai F20 electron microscope (FEI, Portland, OR) at 200 kV, equipped with a 4k x 4k CCD camera (Gatan, Pleasanton, CA). A total of ~121k particles were selected from 2,661 micrographs from the six time-resolved sample sets. Hierarchical classification was performed using the RELION program (19), in conjunction

with a quantitative analysis of convergence (20). To further explore the result quantitatively, we used a new classification scheme, which tracks the shifts of sub-populations and ensures the maximum number of particles for the reconstruction of each of ribosome classes (Shen, B, Sun, M., Li, W., Samir, P., Link, A. and Frank, J., in-preparation) (flowchart, see Supplementary Figure S3.1).

The majority of the cryo-EM ribosome images were complete 80S ribosomes, bound with P/E-tRNA, A/P-P/E-tRNAs or P-E-tRNAs, strongly suggesting they were biologically functional. However after shifting from glucose to glycerol, we noticed a considerable fraction of 80S ribosomes that lacked the density for r-proteins eS1 (yeast rpS1) and uL16 (yeast rpL10) along with their interaction partners (Supplementary Figure S3.2).

Full-scale cryo-EM study. Prompted by the observation of the change in r-proteins composition of 80S ribosomes, we used an FEI Polara TF30 electron microscope operating at 300kV, equipped with GATAN K2 Summit direct detector camera (Gatan, Pleasanton, CA), to collect a larger dataset in an attempt to improve the resolution. A total number of ~291k particles were selected from 6576 micrographs from the six time-resolved sample sets. The six data sets were pooled together for further classification and refinement (for details of the data processing procedure, see Supplementary Figure S3.1).

The first tier in the hierarchical unsupervised classification revealed two major populations, namely 80S ribosomes that are complete, and 80S ribosomes that lack density for uL16 r-protein and/or eS1 r-protein. Since reconstructions from both populations showed fragmented densities, we performed a second tier of exhaustive unsupervised classification.

For the population of complete 80S ribosome, we found five major subpopulations, differing in the occupancies with tRNAs and the presence or absence of intersubunit rotation

(Supplementary Figure S3.1 and Supplementary Table S3.1). The five complete ribosome subpopulations were (i-iii) rotated 80S bound with hybrid P/E tRNA, (denoted as rt80-P/E). These three classes differed from each other in the extent of their head movements; (iv) non-rotated 80S bound with classically configured P- and E-tRNAs (denoted as nrt80S-P-E); (v) non-rotated 80S without tRNAs (denoted as nrt80S-empty). The resolutions of the density maps reconstructed from these classes ranged from 5.6Å to 7.6Å (FSC=0.143, following 'gold-standard' protocol).

For the population of incomplete 80S ribosomes, subsequent classification revealed five different subpopulations, distinguished by presence or absence of r-proteins (Supplementary Figure S3.1 and Supplementary Table S3.1): (i) 80S lacking density for uL16 (Figure 3.1A); (ii-iii) 80S ribosomes lacking densities for both uL16 and eS1 (Figure 3.1B and C); (iv-v) 80S ribosomes lacking densities for both uL16 and eS1, as well as densities for small fragments of rRNA (Figure 3.1D and E). The resolution of these density maps ranged from 6.15Å to 9.8Å (FSC=0.143, following 'gold-standard' protocol).

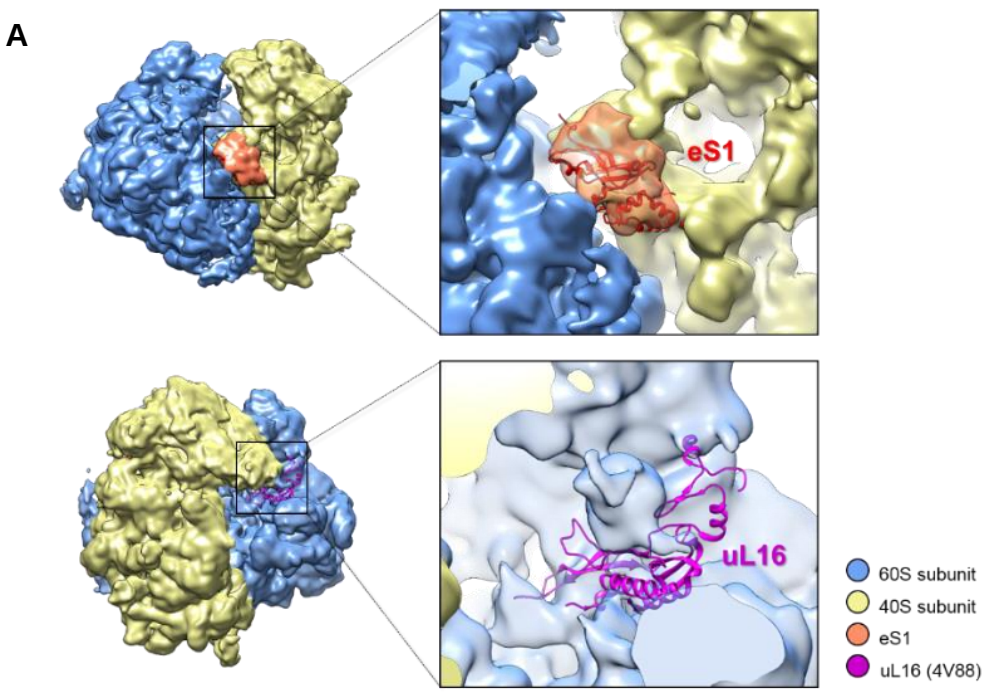

Figure 3.1 (A). Cryo-EM reconstruction of *S. cerevisiae* 80S ribosomes altered in response to glucose-to-glycerol switch. Shown above is a map reconstructed from the sub-population of incomplete 80S ribosome that lacks only the density for uL16 protein (class 1, in Supplementary Table S3.2). In the right zoomed-in panels, cryo-EM densities are shown in transparency. The X-ray structure of *S. cerevisiae* (PDB 4V88) 40S and 60S subunits were separately rigid-body fitted into cryo-EM densities using UCSF Chimera (21).

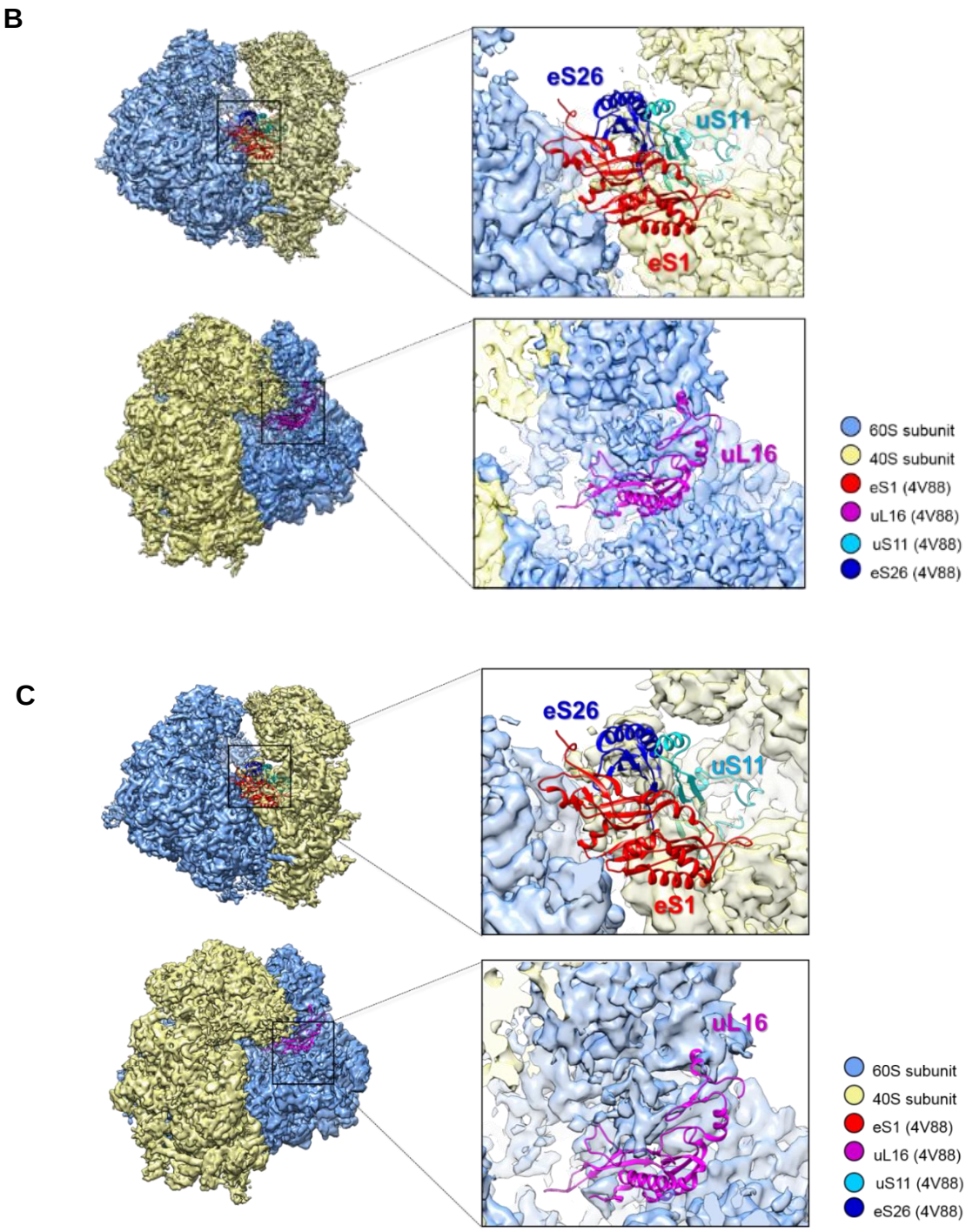
B
eS26
uS11
eS1
uL16
60S subunit
40S subunit
eS1 (4V88)
uL16 (4V88)
uS11 (4V88)
eS26 (4V88)
C
eS26
uS11
eS1
uL16
60S subunit
40S subunit
eS1 (4V88)
uL16 (4V88)
uS11 (4V88)
eS26 (4V88)

Figure 3.1 (B) (C). Cryo-EM reconstructions of *S. cerevisiae* 80S ribosomes altered in response to glucose-to-glycerol switch. Shown above is a map reconstructed from the sub-population of incomplete 80S ribosomes lacking the density for both eS1 and uL16 r-proteins. The interacting partners of eS1, eS26 and uS11 are missing as whole. (B) Rotated incomplete 80S ribosomes (Class2). (C) Non-rotated incomplete 80S ribosomes (Class 3) (class assignment is defined in Supplementary Table S3.2). In the zoomed-in panels, cryo-EM densities are shown in transparency. The X-ray structure of *S. cerevisiae* (PDB 4V88) 40S and 60S subunits were separately rigid body-fitted into cryo-EM densities using UCSF Chimera (21).

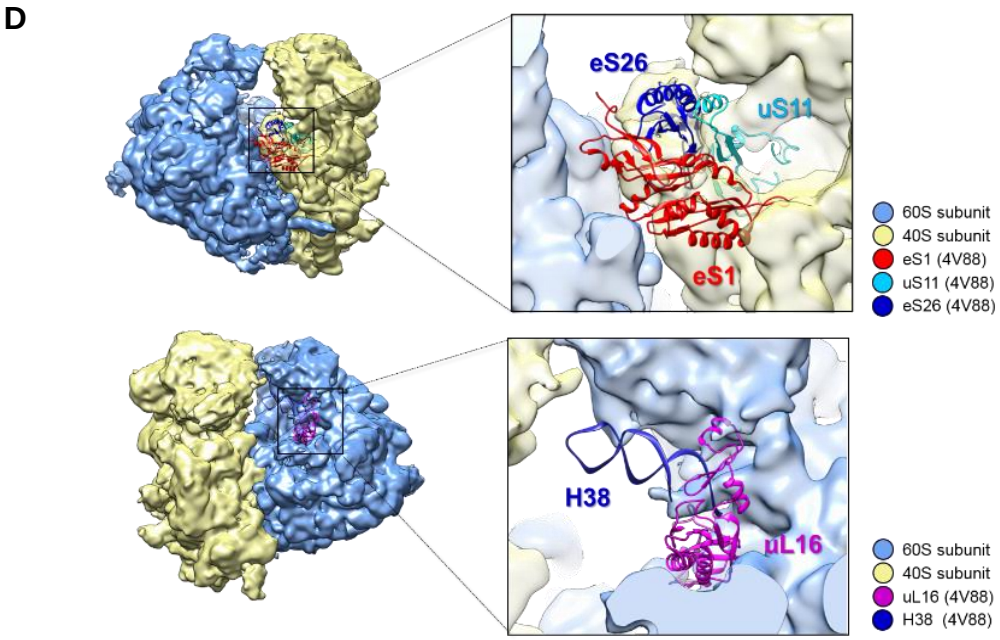

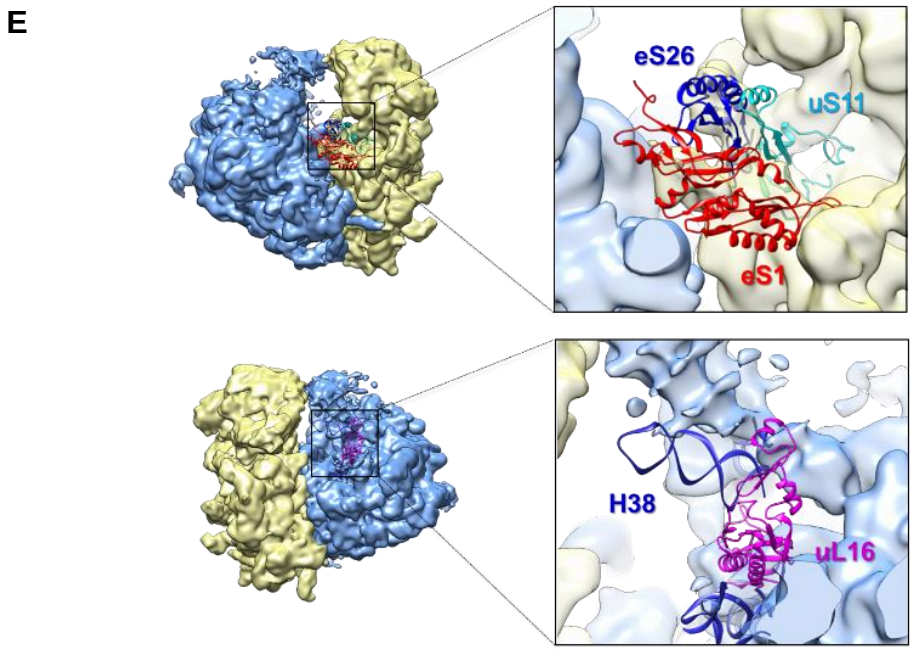

Figure 3.1 (D) (E). Cryo-EM reconstructions of *S. cerevisiae* 80S ribosomes altered in response to glucose-to-glycerol switch. Shown above is a map reconstructed from the sub-populations of incomplete 80S ribosomes lacking the densities for both eS1 and uL16 proteins, as well as H38 of 28S rRNA. The interacting partners of eS1, eS26 and uS11 are missing as whole. **(D-Class 4, E-Class5)** (class assignment is defined in Supplementary Table S3.2). In the zoomed-in panels, cryo-EM densities are shown in transparency. The X-ray structure of *S. cerevisiae* (PDB 4V88) 40S and 60S subunits were separately rigid-body fitted into cryo-EM densities using UCSF Chimera (21).

Global conformational changes of 'incomplete' 80S ribosomes

We also analyzed the conformational changes of the 80S ribosomes after the shift from glucose to glycerol. We observe two main degrees of freedom, namely inter-subunit rotation (22) and swivel movement of the 40S subunit head (23). Compared with the nrt80S-P-E class, which resembles the post-translocational state in the translation elongation process, the class of incomplete 80S ribosomes (class iii) that lacks both uL16 and eS1 r-proteins was found in the non-rotated state. The class that lacks uL16 but has eS1 bound (class i) displayed a ~9 degree counter-clockwise inter-subunit rotation (seen from 40S subunit solvent side). We found no tRNAs in these incomplete classes, indicating these ribosome were not actively translating (Figure 3.2A).

Additionally, maps reconstructed from the incomplete 80S ribosome classes all display unusually large 40S subunit head back-swiveling rotations, ranging from ~13 to ~18 degrees (Figure 3.2B). By comparison, these rotations are limited to ~4 degrees in eEF2-bound yeast (24), ~6 degrees in mammalian ribosomes (25) and ~4 degrees in RRF-bound *E. coli* 70S ribosomes (26)).

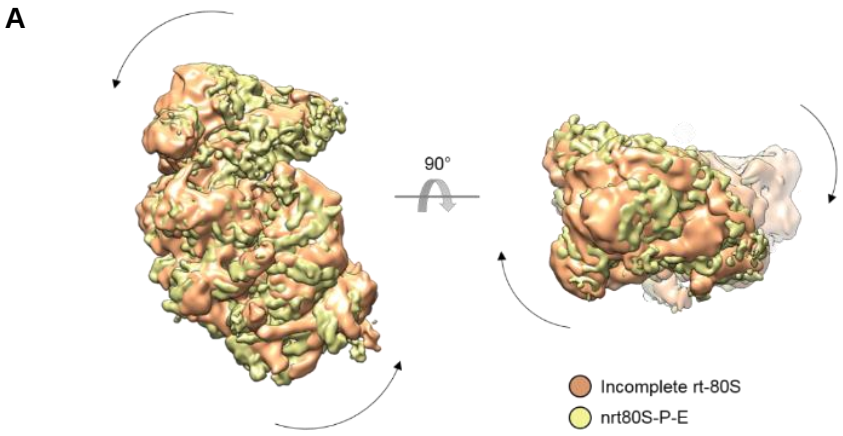

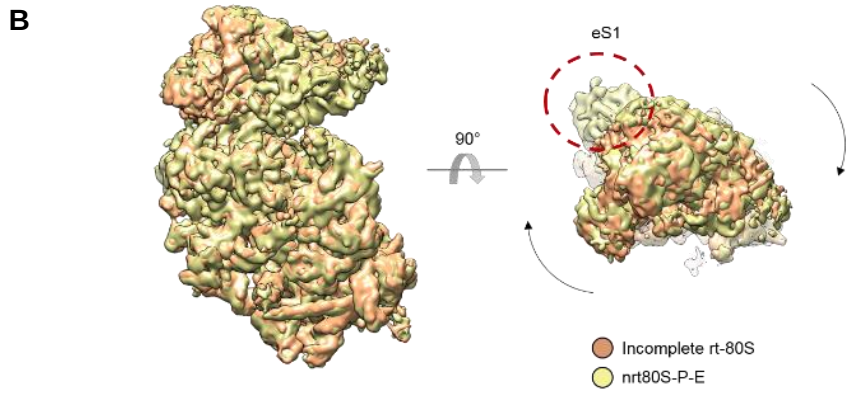

Figure 3.2. Global conformational changes of incomplete 80S ribosomes. (A) Inter-subunit rotation and 40S subunit head-swiveling movements in incomplete 80S (class 1). Comparison of the 40S subunit positions in nrt80S-P-E state (yellow) and the incomplete 80S (class 1) (orange). **(B)** Head-swiveling movements in incomplete 80S (class 3). The position of eS1 on nrt80S-P-E state is highlighted by a red circle. Comparisons were obtained by structural alignment on the 60S subunits of the 80S ribosomes using UCSF Chimera (21).

The binding of uL16 and eS1 and their interacting partners

The most notable finding in our study is the absence of eS1 from 40S subunits and uL16 from 60S subunits. Small-subunit r-protein eS1 is located at the mRNA exit tunnel, and has direct contacts with helix 26 (H26) of the 18S rRNA and the uS11 and eS26 proteins. In the class of incomplete 80S ribosomes lacking eS1, we also found that uS11 and eS26 either displayed scattered densities or were completely absent from the ribosome, suggesting weak binding affinity to the 40S subunits (Figure 3.1).

The large subunit's r-protein uL16 is located in the inter-subunit corridor where aminoacyl-tRNAs (aa-tRNAs) move during the process of accommodation. It has contacts with several key

functionally important sites via its C-terminal region (P-loop), including the peptidyl-transferase center (PTC), H38 of the 28S rRNA (also known as A-site finger), and the elongation factor binding site. It also has interactions with 5S rRNA via its C-terminus and with H69 of the 28S rRNA via its conserved internal loop (18). In the population of incomplete 80S ribosomes, we also found that H38 of the 28S rRNA and its neighboring helices displayed scattered densities. (Figure 3.1D and E, and Supplementary Table S3.2). Such flexibility is not commonly observed in any of our group's 80S ribosome structural studies or other published studies. It suggests that the binding of uL16 to 60S subunits may aid in the stabilization or the correct folding of H38.

The binding of eS1 and uL16 to 80S ribosomes altered upon carbon source switch

To quantitatively investigate the binding behavior of eS1 and uL16 to ribosomes, we monitored the numbers of ribosomal particles that were assigned to the population of 'complete 80S' and 'incomplete 80S' at different time points, T = 0, 30, 120, 240, 450, and 1440 min using our previously described classification strategy (Shen, B., *et al* 2016).

In order to test random experimental variation, we performed the same pooling and tracking strategy in two independent cryo-EM experiments. In both studies, the quantity of particles assigned to the 'incomplete 80S' population increased in the first 30 min after shifting from glucose to glycerol. After the glucose-to-glycerol switch, the binding ratio of uL16 and eS1 to 80S ribosomes decreased in the first 30 min (Figure 3.3).

During this time, the binding ratio of uL16 and eS1 to 80S ribosomes decreased from ~83% to ~66%, and it remained relatively stable: ~64% at T=120 min and ~62% at T=240 min. After incubation in glycerol for 450 min, the binding of uL16 and eS1 in 80S ribosome recovered from 62% to ~71% at T=450 min and stabilized at ~71% at T=1440 min (24 hours) (Figure 3.3).

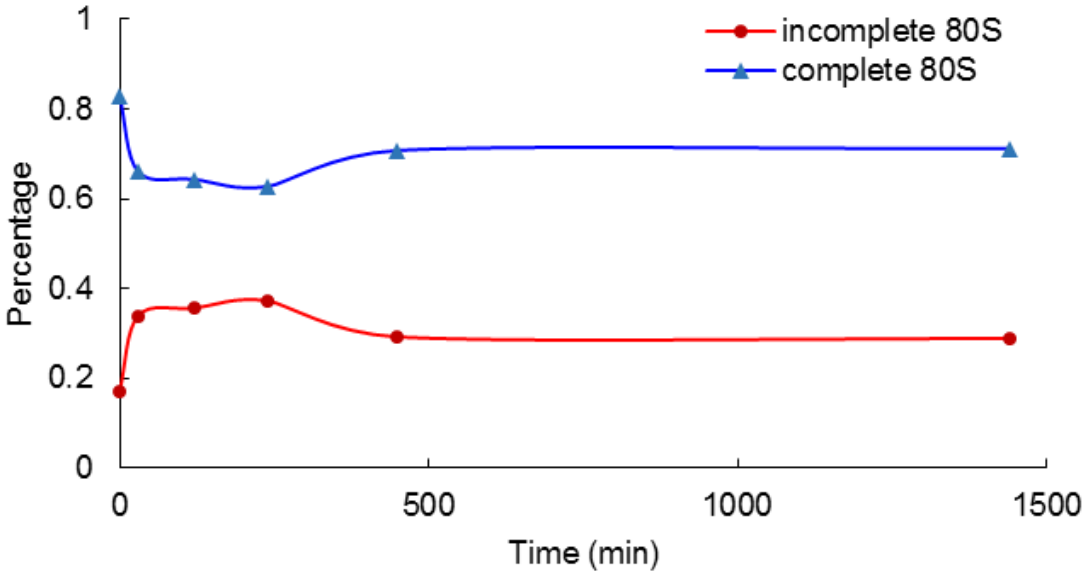

Figure 3.3. Structural inventory as a function of time. "Incomplete 80S" (red) refers to ribosomes that lack eS1 and/or uL16. The x axis represents the time (min) that cells were incubated at glycerol conditions. The y axis represents the percentage of incomplete 80S and complete 80S ribosomes. Generally, percentage of complete 80S ribosomes per each sample set decreased upon onset of glucose-to-glycerol switch. It reflects the decrease of general binding ratio of eS1 and uL16 to 80S ribosomes upon onset of glucose-to-glycerol switch.

Change of polysomal fractions in response to carbon source switch

Since we found that the percentage of complete 80S ribosome decreased following the carbon source switch, we speculated whether global translational activities would also display a similar change. We performed polysome profiling experiments on the time series. Our polysome profiling revealed a re-distribution of polysome into the 80S peak after the 30 min cells shifted from glucose to glycerol (Figure 3.4). After 240 min incubation, the polysomal fractions recovered to a similar level seen in the 450 min samples (Figure 3.4). A similar re-distribution of polysomal fractions to 80S fraction was also observed after cells were shifted from glucose to glycerol for 10 min (27).

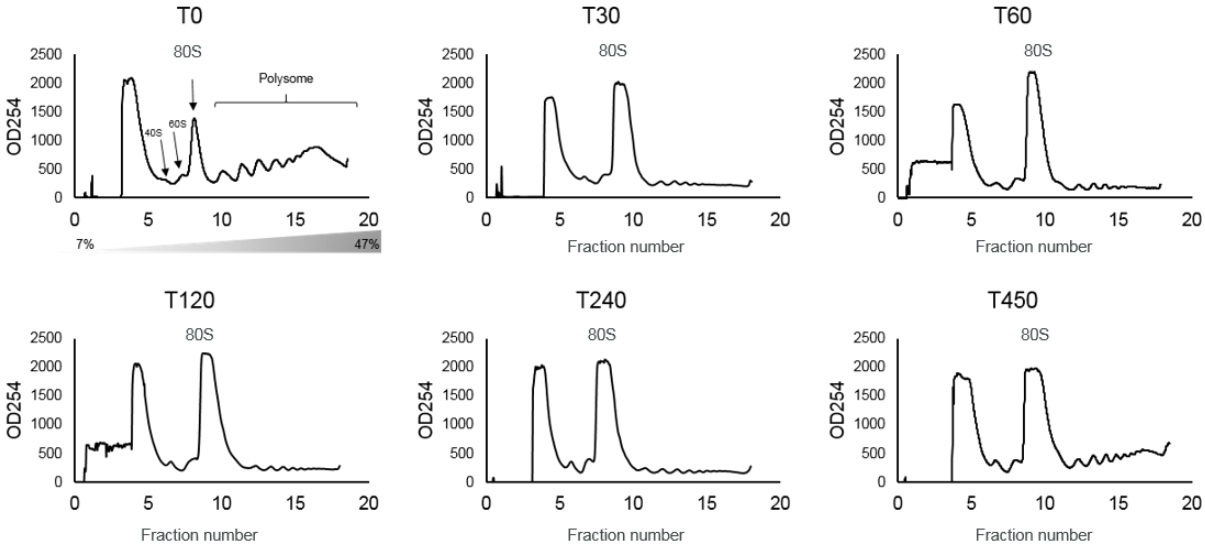

Figure 3.4. The carbon source switch from glucose to glycerol inhibits translation activities. Polyribosome traces from the wild-type strain. Yeast was grown in complete medium containing glucose and re-suspended in medium containing glycerol for the indicated times (minutes). Polyribosomes were analyzed as described in 'Materials and Methods'. The peaks that contain the

small ribosomal subunit (40S), the large ribosomal subunit (60S), and both subunits (80S) are indicated by arrows. The polysome peaks are bracketed.

3.3 Discussion

Rapid response to carbon source switch affected by release of two r-proteins

One of the simplest and fastest ways to modify or abolish the function of a multi-subunit assembly is to alter the relative abundance of individual components that are crucial for its function (28). Proteomic studies on eukaryotic ribosomes have revealed that the cell can alter the stoichiometry of core r-proteins and thereby alter the translational efficacy of distinct mRNAs (16,29). Our studies revealed that the binding of eS1 and uL16 proteins to ribosomes changes rapidly in response to glucose-to-glycerol switch. Considering the time required for ribosome biogenesis, we must attribute this observed change in r-protein composition to release of proteins bound to the ribosome after the carbon source switch, rather than a failure or active inhibition of their incorporation during ribosome biogenesis. Ribosome biogenesis is a time- and energy-consuming process that requires hours to complete (30,31). Considerations of parsimony in energy consumption alone would not favor this mode of regulation. With this in mind, the role of eS1 and uL16 in ribosome is expected to play a crucial role.

The absence of eS1 on the 40S subunit and polysome formation

Depletion of eS1 is known to moderate reduce cell growth (32). Structural studies have shown that the mammalian eukaryotic polysome complex is arranged in a left-handed supra-molecular helix, in the core region of which 80S ribosome are closely packed (17). There are three

main clusters of inter-ribosome contact sites within the core region. The r-protein eS1 along with its neighbors, uS11, eS26, h16, contribute to one of these clusters (17).

In our study, the binding ratio of eS1 and its neighbors to 80S ribosomes decreased as a function of time during the shift from glucose to glycerol (Figure 3.3). Moreover, the polysomal fractions also decreased within 30 min, which indicates that the general translation activities were reduced during this time span. In addition to our observation on eS1, cDNA microarray results also showed that the presence of eS1 and formation of polysomes is correlated. They found that eS1 mRNA relocalizes from the polysomal fractions to the 80S fractions in response to glucose-to-glycerol switch (27). Given these observations and results, the polysome formation is likely to be regulated by the presence or absence of eS1 from the ribosome. However, understanding the exact structural effects of eS1, relative to the other inter-ribosomal "glue" components, on the entire polysome formation requires further study.

The absence of uL16 on the 60S subunit and inhibition of translation

Unlike eS1, r-protein uL16 (rpL10 in yeast) is an essential protein and its null mutation is required for cell growth (33). The uL16 loop mutants (S104D) showed differences in peptidyltransferase activity and translational fidelity compared to wild-type ribosomes (18). In terms of ribosomal conformations, the S104D mutant drives the ribosome toward the rotated state, while a second uL16 mutant, A106R, causes vacant ribosomes to shift toward the non-rotated state (18). In our cryo-EM reconstructions of incomplete 80S subpopulations, we found that four classes lack both r-proteins uL16 and eS1, while one class lacks only uL16. Moreover, the subpopulation of incomplete 80S ribosomes did not show any preference of rotated versus non-rotated conformations (rotated 80S: non-rotated 80S ~ 1:1), while the subpopulation of complete 80S

ribosomes strongly favored the rotated conformation (rotated 80S: non-rotated 80S ~2.8:1). In summary, release of essential protein uL16/rpL10 is expected to completely disable translation on the ribosome.

3.4 Conclusions

Understanding the regulation and structure of ribosomes is essential to understanding their role in the cell's adaption to environmental changes at the translation level. Here, we performed a time series of cryo-electron microscopy experiments on purified 80S ribosomes to characterize the global changes in ribosomal proteins that accompany the adaptation of *Saccharomyces cerevisiae* switched from a fermentable to a non-fermentable carbon source. The most notable observation is the release of r-protein eS1 and uL16 from the ribosomes to which they are bound, and the resulting decrease in the binding ratio of the proteins as a function of time. In addition, our polysome profiling data showed a reduction in general translational upon carbon source switch. Taken together, these findings suggest the existence of a mechanism for rapid control of translation that is exerted through the release of specific ribosomal proteins, and provide additional support to the view that r-protein composition serves as a means to remodel the translational machinery upon environmental change. Because of the complexity of this regulatory mechanism, there is a great need for in-depth studies to gain comprehensive insight into the functional reprogramming of the ribosome. Among the unsolved questions are the molecular mechanisms causing the release of eS1 and uL16, the impact of the presence/absence of these proteins on the formation of polysome, and the stoichiometry of r-proteins in response to other types of environmental changes.

3.5 Materials and Methods

Strains and media

All experiments used the diploid *S. cerevisiae* strain BY4743, which has been previously described (34). Cells were grown using standard techniques (35).

Ribosome isolation and purification

S. cerevisiae cells were grown in YPD (1% yeast extract, 2% peptone, 2 % glucose) media and shifted to YPG (1% yeast extract, 2% peptone, 3% glycerol) at the following time points, 0min, 30min, 120min, 240min and 450min. Ribosomes were isolated and purified as described following.

Cells were first centrifuged at 2000 rpm for 5 min at 4℃ using a Sorvall HLR6/H600A/HBB6 rotor in Sorvall RC-3B centrifuge and washed with ice cold deionized H_2O. The pellets were resuspended in 1 mL ice cold wash buffer (10 mM Tris pH 8, 5 mM β-mercaptoethanol, 500 mM ammonium chloride, 100 mM magnesium acetate) and lysed at 4℃ using glass beads and a Bead Beater (BioSpec, Inc) for 10 min as previously described (36). Cell suspension was clarified centrifugation at 20,000g for 15 min at 4℃. The pellet was discarded and the supernatant was overlaid onto a 5-20% discontinuous sucrose gradient prepared in wash buffer. The gradients were centrifuged at 28,000 rpm using a SW-41 swinging bucket rotor for 18 h at 4℃. The ribosome-enriched pellet was resuspended in ice cold 1 mL standard buffer (10 mM Tris pH 8, 5 mM β-mercaptoethanol, 50 mM ammonium chloride, 5 mM magnesium acetate) and centrifuged for 10 min at 10,000g at 4℃. The pellet was discarded and the ribosome suspension was stored at -80℃.

Polysome profiling

Polysome profiling was modified from previous methods (36). *S. cerevisiae* cells were grown in YPD to mid-log phase. Strains were then transferred to YPG and allowed to continue to

grow. At 30 min, 120 min, 240 min and 450 min, cells were collected and lysed as previously described. Protein concentration was layered on top 7% - 47% sucrose gradients and centrifuged.

Cryo-electron microscopy

Four microliters of purified ribosomes were applied to holey carbon grids (carbon-coated Quantifoil R2/4 grid, Quantifoil Micro Tools, GmbH, Großlöbichau, Germany) containing an additional continuous thin layer of carbon, glow-discharged using Gatan Solarus 950 (37). Grids were blotted for 4 s at 4°C in 100% humidity and vitrified by plunging into liquid ethane cooled with liquid nitrogen, using the Mark IV Vitrobot (FEI, Hillsboro, Oregon) (38).

For the initial studies, six data sets, T=0 min, 30 min, 120 min, 240 min, 450 min and 1440 min, were collected on a FEI Tecnai F20 electron microscope (FEI, Hillsboro, Oregon) operating at 200 kV, equipped with a 4k x 4k CCD camera (Gatan, Pleasanton, CA). Images were recorded using the automated data collection system Leginon (39), and taken at the magnification of 5,000 x, corresponding to a calibrated pixel size of 2.245 Å.

For the full-scale study, data (T=0, 30, 120, 240, 450 and 1440 min) were collected on a TF30 Polara electron microscope (FEI, Hillsboro, Oregon) operating at 300 kV, set up with a K2 Summit direct electron detection camera (Gatan, Warrendale, PA). Images were recorded using the automated data collection system Leginon (39) in counting mode, and taken at the nominal magnification of 23,000 x, corresponding to a calibrated pixel size of 1.66 Å. The dose rate was nominally set to 8 electron counts per physical pixel per second (40) and the total exposure time was 8 seconds. Image stacks were collected in a defocus range of −1.5 μm to −3.5 μm, fractionated into 20 frames, each with an exposure time of 0.4 seconds.

Image processing

Six time-resolved sample sets, T=0, 30, 120, 240, 450 and 1440 min, were pooled and processed together. Frist the dose-fractionated image stacks were corrected for beam-induced motion, using the method of Li ***et al***. (41), and averages of all 20 frames were used for image processing. A total number of ~291k particles were extracted from 6576 selected averaged images. Particle picking was using the ara-autopick and ara-crop tools in Arachnid, and contrast transfer function parameters were estimated using the sp-defocus tool in Arachnid (42). 3D classification was performed to discard defective particles and identify structurally homogeneous subsets, using RELION (version 1.2) software (43).

Initial RELION 3D classification, with K = 10 classes and an angular sampling of 1.8°, revealed two major populations, namely 80S ribosomes that are complete, and 80S ribosomes that lack densities for uL16 r-protein and/or eS1 r-protein, (denoted in the following as 'complete 80S' and 'incomplete 80S', respectively). Since reconstructions from both populations showed fragmented densities, we performed a second tier of exhaustive 3D classification to further explore the heterogeneity. We quantitatively and qualitatively analyzed the classification result, by (1) quantitative jumper analysis (20), and (2) prior structural knowledge of *S. cerevisiae* 80S ribosomes. In such way, we re-grouped classes which have are conformational and compositional similar, and performed RELION auto-refinement on each class. (Supplementary Figure S3.1).

In total, we found ten major subpopulations, five complete 80S populations and five incomplete 80S populations. For the population of complete 80S ribosomes, we have (1) rotated 80S bound with P/E tRNA, with an average resolution of ~5.6Å, (2) rotated 80S with P/E tRNA, ~6.3Å, (3) rotated 80S with P/E tRNA, ~7.6Å. (4) non-rotated 80S with P/P- and E/E- tRNAs, ~6.5Å, (5) non-rotated 80S without any tRNAs, ~6.4Å. The first three rotated 80S classes are

different from each other by the degree of inter-subunit rotation and head movements, comparison with class 4, nrt80S-P-E (Supplementary Figure S3.1).

For the population of incomplete 80S ribosomes, we have (1) rotated 80S, lacking only the density for uL16, with an average resolution of ~9.4Å, (2) rotated 80S, lacking densities for both uL16 and eS1, ~6.1Å, (3) non-rotated 80S lacking densities for both uL16 and eS1, ~6.5Å, (4) non-rotated 80S lacking densities for both uL16 and eS1, as well as densities for small fragments of rRNA, ~9.2Å, (5) non-rotated 80S lacking densities for both uL16 and eS1, as well as densities for small fragments of rRNA, ~9.8Å (Figure 3.1 and Supplementary Figure S3.1).

Resolutions reported were based throughout on the 'gold standard' protocol along with the FSC = 0.143 criterion, and involved soft masking and high-resolution noise substitution (44). For the final visualization, all density maps were corrected for the effects of a soft mask in RELION post-processing (43,44), and sharpened by application of an automatically estimated negative b-factor (43).

3.6 Supplementary Materials

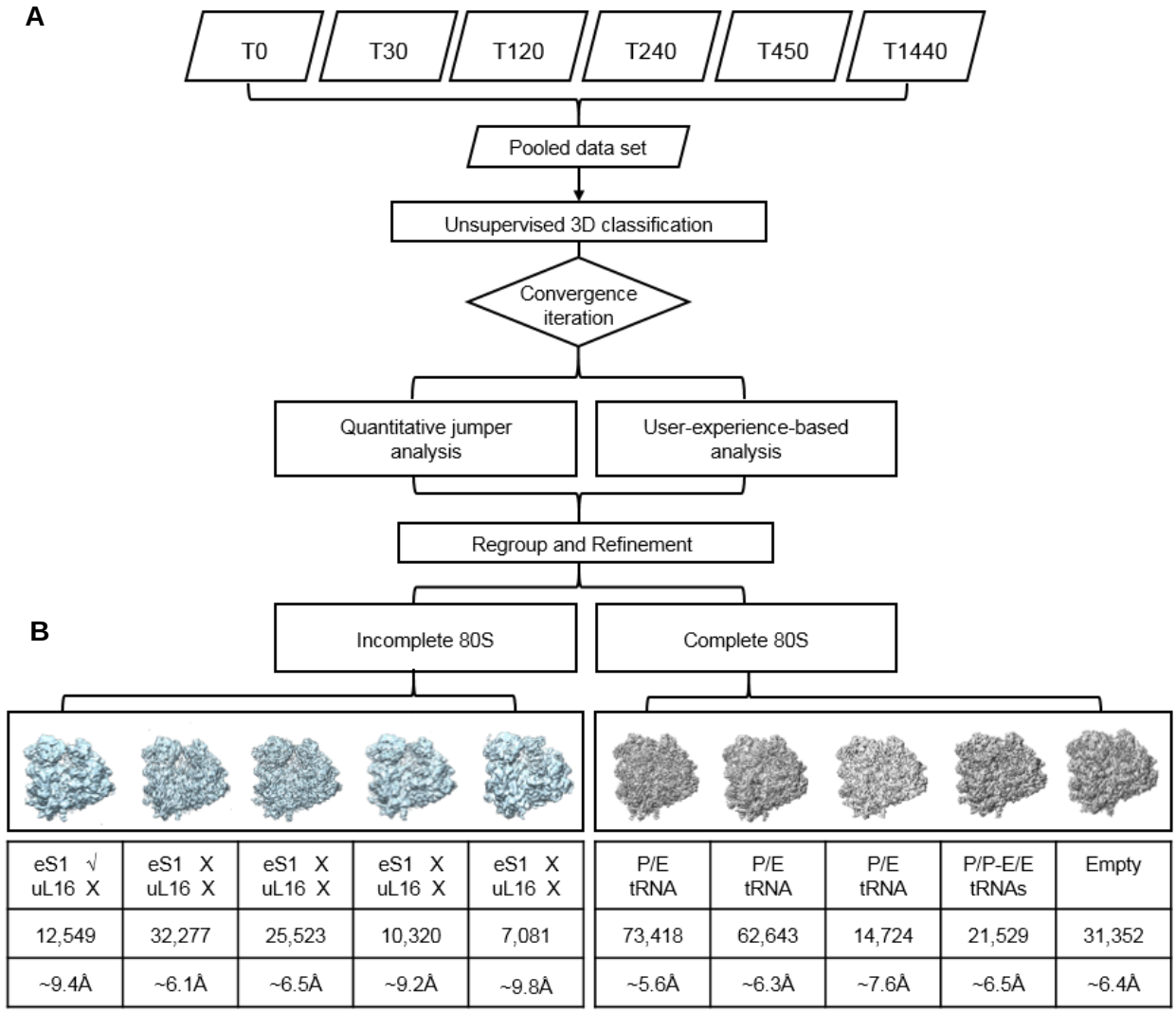

eS1 √ uL16 X	eS1 X uL16 X	eS1 X uL16 X	eS1 X uL16 X	eS1 X uL16 X	P/E tRNA	P/E tRNA	P/E tRNA	P/P-E/E tRNAs	Empty
12,549	32,277	25,523	10,320	7,081	73,418	62,643	14,724	21,529	31,352
~9.4Å	~6.1Å	~6.5Å	~9.2Å	~9.8Å	~5.6Å	~6.3Å	~7.6Å	~6.5Å	~6.4Å

Supplementary Figure S3.1. Full framework of 'pooled' classification strategy and results. (A) Schematic diagram of our 'pooled classification' data processing procedure. Samples purified from six time points were pooled together and classified using the same. Further analysis was based mainly on quantitative jumper analysis (20) with minimum user interference. (B) Summary of the full-scale cryo-EM studies. "√", present; "X", absent. Cryo-EM reconstructions of incomplete 80S ribosomes are presented from front view and colored in light blue (B, left), while complete 80S ribosomes are colored in grey (B, right). Resolutions reported are based throughout on the 'gold standard' protocol along with the FSC = 0.143 criterion, and involved soft masking and high-resolution noise substitution (44).

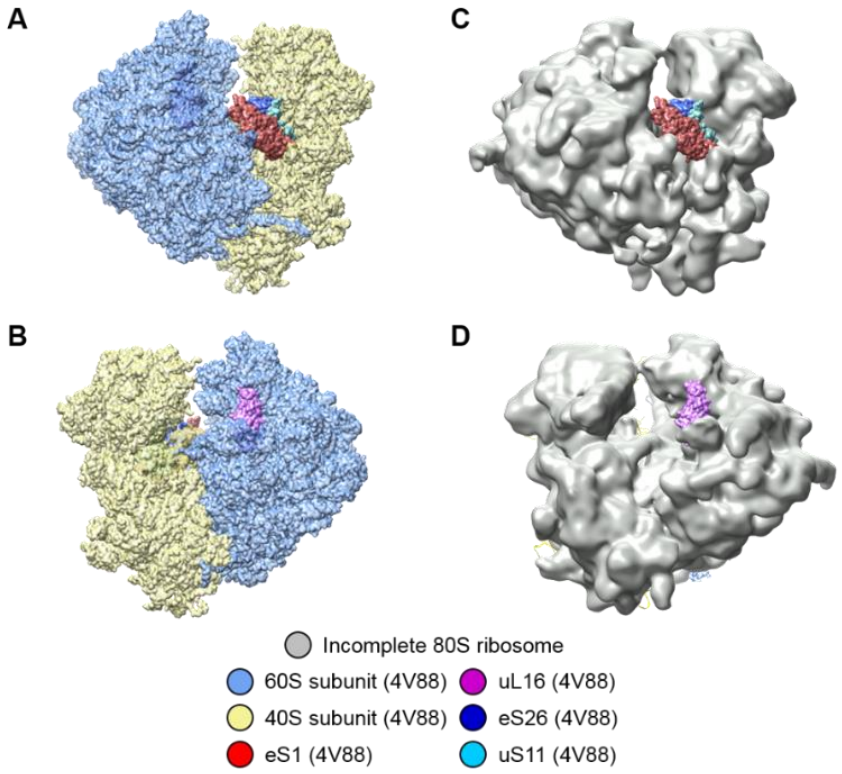

Supplementary Figure S3.2. Initial studies of *S. cerevisiae* ribosome altered in response to glucose-to-glycerol switch. **(A) (B)** Positions of eS1 and uL16 on 80S ribosomes. Maps were simulated from x-ray structure of *S. cerevisiae* 80S ribosome (PDB 4V88) in UCSF Chimera. **(C) (D)** Cryo-EM densities of incomplete 80S ribosomes lack the density for eS1 and uL16 proteins. X-ray structure of *S. cerevisiae* 80S ribosome (PDB 4V88) was rigid body fitted into density maps in UCSF Chimera (21). Structures of eS1 and uL16 proteins are highlighted in red and magenta color respectively.

Class	1	2	3	4	5
tRNA occupancy	Hybrid P/E	Hybrid P/E	Hybrid P/E	P/P-E/E	Empty
Head movement	~14°	~13°	~12°	/	/
Particle No.	73,418	62,643	14,724	21,529	31,352
Resolution	~5.6Å	~6.3Å	~7.6Å	~6.5Å	~6.4Å

Supplementary Table S3.1. Summary of main characteristics of populations of complete 80S ribosomes. The measurements of head movements was calculated in UCSF Chimera based on the helix 34 of 18S rRNA. The crossing angle reported from UCSF Chimera (21) were shown in the above table. Class 4, complete 80S bound with classical configured P/P and E/E tRNAs was used as the reference to study the global movements of ribosomes.

Class	1	2	3	4	5
Particle No.	12,549	32,277	25,523	10,320	7,081
Resolution	~9.4Å	~6.1Å	~6.5Å	~9.2Å	~9.8Å
eS1	√	X	X	X	X
uL16	X	X	X	X	X
H38 (28S)	√	√	√	**	**

Supplementary Table S3.2. Summary of main characteristics of populations of incomplete 80S ribosomes. "√", present; 'X', absent; "**", scattered density.

Author contributions

M.S., B.S., P.S, A.L. and J.F. designed the experiments. P.S, prepared the biological samples and the polysome profiling experiments. M.S. and B.S. performed cryo-EM experiments, classification, 3D reconstructions, and refinement. M.S., B.S., W.L., A.L. and J.F. interpreted the results. M.S., P.S., A.L. and J.F. wrote the manuscript.

3.7 References

1. Samir, P., Rahul, Slaughter, J.C. and Link, A.J. (2015) Environmental Interactions and Epistasis Are Revealed in the Proteomic Responses to Complex Stimuli. *PLoS ONE,* **10**.

2. Gasch, A.P., Spellman, P.T., Kao, C.M., Carmel-Harel, O., Eisen, M.B., Storz, G., Botstein, D. and Brown, P.O. (2000) Genomic expression programs in the response of yeast cells to environmental changes. *Mol Biol Cell,* **11**, 4241-4257.

3. Broach, J.R. (2012) Nutritional Control of Growth and Development in Yeast. *Genetics*, **192**, 73-105.

4. Ashe, M.P., De Long, S.K. and Sachs, A.B. (2000) Glucose depletion rapidly inhibits translation initiation in yeast. *Mol. Biol. Cell,* **11**, 833-848.

5. Conway, M.K., Grunwald, D. and Heideman, W. (2012) Glucose, nitrogen, and phosphate repletion in Saccharomyces cerevisiae: common transcriptional responses to different nutrient signals. *G3 (Bethesda),* **2**, 1003-1017.

6. Martinez, M.J., Roy, S., Archuletta, A.B., Wentzell, P.D., Anna-Arriola, S.S., Rodriguez, A.L., Aragon, A.D., Quinones, G.A., Allen, C. and Werner-Washburne, M. (2004) Genomic analysis of stationary-phase and exit in Saccharomyces cerevisiae: gene expression and identification of novel essential genes. *Mol Biol Cell,* **15**, 5295-5305.

7. Radonjic, M., Andrau, J.C., Lijnzaad, P., Kemmeren, P., Kockelkorn, T.T.J.P., van Leenen, D., van Berkum, N.L. and Holstege, F.C.P. (2005) Genome-wide analyses reveal RNA polymerase II located upstream of genes poised for rapid response upon S-cerevisiae stationary phase exit. *Molecular Cell,* **18**, 171-183.

8. Jona, G., Choder, M. and Gileadi, O. (2000) Glucose starvation induces a drastic reduction in the rates of both transcription and degradation of mRNA in yeast. *Biochim Biophys Acta*, **1491**, 37-48.

9. Ben-Shem, A., de Loubresse, N.G., Melnikov, S., Jenner, L., Yusupova, G. and Yusupov, M. (2011) The Structure of the Eukaryotic Ribosome at 3.0 angstrom Resolution. *Science*, **334**, 1524-1529.

10. Ramagopal, S. (1992) Are eukaryotic ribosomes heterogeneous? Affirmations on the horizon. *Biochem Cell Biol*, **70**, 269-272.

11. Xue, S. and Barna, M. (2012) Specialized ribosomes: a new frontier in gene regulation and organismal biology. *Nature Reviews Molecular Cell Biology*, **13**, 355-369.

12. Sherton, C.C. and Wool, I.G. (1974) A comparison of the proteins of rat skeletal muscle and liver ribosomes by two-dimensional polyacrylamide gel electrophoresis. Observations on the partition of proteins between ribosomal subunits and a description of two acidic proteins in the large subunit. *J Biol Chem*, **249**, 2258-2267.

13. Vesper, O., Amitai, S., Belitsky, M., Byrgazov, K., Kaberdina, A.C., Engelberg-Kulka, H. and Moll, I. (2011) Selective Translation of Leaderless mRNAs by Specialized Ribosomes Generated by MazF in Escherichia coli. *Cell*, **147**, 147-157.

14. Xue, S., Tian, S., Fujii, K., Kladwang, W., Das, R. and Barna, M. (2015) RNA regulons in Hox 5′ UTRs confer ribosome specificity to gene regulation. *Nature*, **517**, 33-38.

15. Kondrashov, N., Pusic, A., Stumpf, C.R., Shimizu, K., Hsieh, A.C., Xue, S., Ishijima, J., Shiroishi, T. and Barna, M. (2011) Ribosome-Mediated Specificity in Hox mRNA Translation and Vertebrate Tissue Patterning. *Cell*, **145**, 383-397.

16. Slavov, N., Semrau, S., Airoldi, E., Budnik, B. and van Oudenaarden, A. (2015) Differential Stoichiometry among Core Ribosomal Proteins. *Cell Reports*, **13**, 865-873.

17. Myasnikov, A.G., Afonina, Z.A., Menetret, J.F., Shirokov, V.A., Spirin, A.S. and Klaholz, B.P. (2014) The molecular structure of the left-handed supra-molecular helix of eukaryotic polyribosomes. *Nat Commun*, **5**, 5294.

18. Sulima, S.O., Gulay, S.P., Anjos, M., Patchett, S., Meskauskas, A., Johnson, A.W. and Dinman, J.D. (2014) Eukaryotic rpL10 drives ribosomal rotation. *Nucl. Acids Res.*, **42**, 2049-2063.

19. Scheres, S.H.W. (2012) RELION: Implementation of a Bayesian approach to cryo-EM structure determination. *Journal of Structural Biology*, **180**, 519-530.

20. Chen, B., Shen, B. and Frank, J. (2014) Particle migration analysis in iterative classification of cryo-EM single-particle data. *J Struct Biol*, **188**, 267-273.

21. Pettersen, E.F., Goddard, T.D., Huang, C.C., Couch, G.S., Greenblatt, D.M., Meng, E.C. and Ferrin, T.E. (2004) UCSF chimera - A visualization system for exploratory research and analysis. *J Comput Chem*, **25**, 1605-1612.

22. Frank, J. and Agrawal, R.K. (2000) A ratchet-like inter-subunit reorganization of the ribosome during translocation. *Nature*, **406**, 318-322.

23. Ratje, A.H., Loerke, J., Mikolajka, A., Brunner, M., Hildebrand, P.W., Starosta, A.L., Donhofer, A., Connell, S.R., Fucini, P., Mielke, T. *et al.* (2010) Head swivel on the ribosome facilitates translocation by means of intra-subunit tRNA hybrid sites. *Nature*, **468**, 713-U143.

24. Spahn, C.M., Gomez-Lorenzo, M.G., Grassucci, R.A., Jorgensen, R., Andersen, G.R., Beckmann, R., Penczek, P.A., Ballesta, J.P. and Frank, J. (2004) Domain movements of elongation factor eEF2 and the eukaryotic 80S ribosome facilitate tRNA translocation. *EMBO J*, **23**, 1008-1019.

25. Budkevich, T.V., Giesebrecht, J., Behrmann, E., Loerke, J., Ramrath, D.J., Mielke, T., Ismer, J., Hildebrand, P.W., Tung, C.S., Nierhaus, K.H. *et al.* (2014) Regulation of the mammalian elongation cycle by subunit rolling: a eukaryotic-specific ribosome rearrangement. *Cell*, **158**, 121-131.

26. Dunkle, J.A., Wang, L., Feldman, M.B., Pulk, A., Chen, V.B., Kapral, G.J., Noeske, J., Richardson, J.S., Blanchard, S.C. and Cate, J.H. (2011) Structures of the bacterial ribosome in classical and hybrid states of tRNA binding. *Science*, **332**, 981-984.

27. Kuhn, K.M., DeRisi, J.L., Brown, P.O. and Sarnow, P. (2001) Global and specific translational regulation in the genomic response of Saccharomyces cerevisiae to a rapid

transfer from a fermentable to a nonfermentable carbon source. *Mol. Cell. Biol.*, **21**, 916-927.

28. Sauert, M., Temmel, H. and Moll, I. (2015) Heterogeneity of the translational machinery: Variations on a common theme. *Biochimie*, **114**, 39-47.

29. Mauro, V.P. and Edelman, G.M. (2002) The ribosome filter hypothesis. *PNAS*, **99**, 12031-12036.

30. Mulder, A.M., Yoshioka, C., Beck, A.H., Bunner, A.E., Milligan, R.A., Potter, C.S., Carragher, B. and Williamson, J.R. (2010) Visualizing Ribosome Biogenesis: Parallel Assembly Pathways for the 30S Subunit. *Science*, **330**, 673-677.

31. Granneman, S. and Tollervey, D. (2007) Building ribosomes: Even more expensive than expected? *Current Biology*, **17**, R415-R417.

32. Steffen, K.K., McCormick, M.A., Pham, K.M., MacKay, V.L., Delaney, J.R., Murakami, C.J., Kaeberlein, M. and Kennedy, B.K. (2012) Ribosome Deficiency Protects Against ER Stress in Saccharomyces cerevisiae. *Genetics*, **191**, 107-118.

33. Petrov, A.N., Meskauskas, A., Roshwalb, S.C. and Dinman, J.D. (2008) Yeast ribosomal protein L10 helps coordinate tRNA movement through the large subunit. *Nucl. Acids Res.*, **36**, 6187-6198.

34. Brachmann, C.B., Davies, A., Cost, G.J., Caputo, E., Li, J., Hieter, P. and Boeke, J.D. (1998) Designer deletion strains derived from Saccharomyces cerevisiae S288C: a useful set of strains and plasmids for PCR-mediated gene disruption and other applications. *Yeast*, **14**, 115-132.

35. Amberg, D.C., Burke, D., Strathern, J.N. and Laboratory, C.S.H. (2005) *Methods in Yeast Genetics: A Cold Spring Harbor Laboratory Course Manual*. Cold Spring Harbor Laboratory Press.

36. Browne, C.M., Samir, P., Fites, J.S., Villarreal, S.A. and Link, A.J. (2013) The yeast eukaryotic translation initiation factor 2B translation initiation complex interacts with the fatty acid synthesis enzyme YBR159W and endoplasmic reticulum membranes. *Mol Cell Biol*, **33**, 1041-1056.

37. Grassucci, R.A., Taylor, D.J. and Frank, J. (2007) Preparation of macromolecular complexes for cryo-electron microscopy. *Nat Protoc*, **2**, 3239-3246.

38. Dubochet, J., Adrian, M., Chang, J.J., Homo, J.C., Lepault, J., McDowall, A.W. and Schultz, P. (1988) Cryo-electron microscopy of vitrified specimens. *Q Rev Biophys*, **21**, 129-228.

39. Suloway, C., Pulokas, J., Fellmann, D., Cheng, A., Guerra, F., Quispe, J., Stagg, S., Potter, C.S. and Carragher, B. (2005) Automated molecular microscopy: the new Leginon system. *J Struct Biol*, **151**, 41-60.

40. Liao, M., Cao, E., Julius, D. and Cheng, Y. (2013) Structure of the TRPV1 ion channel determined by electron cryo-microscopy. *Nature*, **504**, 107-112.

41. Li, X., Mooney, P., Zheng, S., Booth, C.R., Braunfeld, M.B., Gubbens, S., Agard, D.A. and Cheng, Y. (2013) Electron counting and beam-induced motion correction enable near-atomic-resolution single-particle cryo-EM. *Nat Methods*, **10**, 584-590.

42. Langlois, R., Pallesen, J., Ash, J.T., Nam Ho, D., Rubinstein, J.L. and Frank, J. (2014) Automated particle picking for low-contrast macromolecules in cryo-electron microscopy. *J Struct Biol*, **186**, 1-7.

43. Scheres, S.H. (2012) RELION: implementation of a Bayesian approach to cryo-EM structure determination. *J Struct Biol*, **180**, 519-530.

44. Chen, S., McMullan, G., Faruqi, A.R., Murshudov, G.N., Short, J.M., Scheres, S.H. and Henderson, R. (2013) High-resolution noise substitution to measure overfitting and validate resolution in 3D structure determination by single particle electron cryomicroscopy. *Ultramicroscopy*, **135**, 24-35.

Chapter 4 Time-resolved cryo-EM studies of prokaryotic translation on the millisecond time scale

This part is a paper published in Structure, ("Structural dynamics of ribosome subunit association studied by mixing-spraying time-resolved cryo-EM". Structure 23, 1097–1105. PMID: 26004440; PMC: PMC4456197), where we described the optimization and application of time-resolved cryo-EM study to ribosomal subunit association studies.

Article

Structure

Structural Dynamics of Ribosome Subunit Association Studied by Mixing-Spraying Time-Resolved Cryogenic Electron Microscopy

Highlights

- Used time-resolved cryo-EM to image sample after 60 ms and 140 ms reaction times
- Captured pre-equilibrium states of the ribosome subunit association reaction
- Visualized and quantified the occupancies of three ribosome conformations
- At 60 ms all intersubunit bridges are fully formed in the associated 70S ribosome

Authors

Bo Chen, Sandip Kaledhonkar, ..., Ruben L. Gonzalez, Jr., Joachim Frank

Correspondence

jf2192@cumc.columbia.edu

In Brief

A time-resolved cryo-EM method, which Chen et al. show to be able to resolve fast (tens to hundreds of milliseconds) reactions in a two-component mixing experiment, promises to be of general utility in the study of molecular interactions that are too fast for conventional blotting-plunging cryo-EM.

Chen et al., 2015, Structure 23, 1097–1105
June 2, 2015
http://dx.doi.org/10.1016/j.str.2015.04.007

Structural Dynamics of Ribosome Subunit Association Studied by Mixing-Spraying Time-Resolved Cryogenic Electron Microscopy

Bo Chen,[1] Sandip Kaledhonkar,[1] Ming Sun,[2] Bingxin Shen,[3] Zonghuan Lu,[4] David Barnard,[5] Toh-Ming Lu,[4] Ruben L. Gonzalez, Jr.,[6] and Joachim Frank[1,2,3,*]

[1]Department of Biochemistry & Molecular Biophysics, Columbia University, New York, NY 10032, USA
[2]Department of Biological Sciences, Columbia University, New York, NY 10027, USA
[3]Howard Hughes Medical Institute, Columbia University, New York, NY 10032, USA
[4]Center for Integrated Electronics, Rensselaer Polytechnic Institute, Troy, NY 12180, USA
[5]Wadsworth Center, Albany, New York State Department of Health, Albany, NY 12201, USA
[6]Department of Chemistry, Columbia University, New York, NY 10027, USA
*Correspondence: jf2192@cumc.columbia.edu
http://dx.doi.org/10.1016/j.str.2015.04.007

SUMMARY

Ribosomal subunit association is a key checkpoint in translation initiation but its structural dynamics are poorly understood. Here, we used a recently developed mixing-spraying, time-resolved, cryogenic electron microscopy (cryo-EM) method to study ribosomal subunit association in the sub-second time range. We have improved this method and increased the cryo-EM data yield by tenfold. Pre-equilibrium states of the association reaction were captured by reacting the mixture of ribosomal subunits for 60 ms and 140 ms. We also identified three distinct ribosome conformations in the associated ribosomes. The observed proportions of these conformations are the same in these two time points, suggesting that ribosomes equilibrate among the three conformations within less than 60 ms upon formation. Our results demonstrate that the mixing-spraying method can capture multiple states of macromolecules during a sub-second reaction. Other fast processes, such as translation initiation, decoding, and ribosome recycling, are amenable to study with this method.

INTRODUCTION

Many biological processes occur on the millisecond scale. Example processes include tRNA selection on the ribosome during protein synthesis (Blanchard et al., 2004) (reviewed in Johansson et al., 2008; Rodnina et al., 2005), acetylcholine receptor desensitization (Dilger and Brett, 1990; Matsubara et al., 1992), and subunit rotation of F_0F_1-ATP synthase (Diez et al., 2004). Visualizing the biological molecules engaged in these processes under physiologically relevant conditions can greatly help us to understand the underlying molecular mechanisms. We used time-resolved cryogenic electron microscopy (cryo-EM) (Lu et al., 2009) to achieve this goal.

Cryo-EM is able to reveal the structures of biological macromolecules in vitro under close to physiological conditions and free from the intermolecular packing interactions that are inherent to X-ray crystallographic approaches. In cryo-EM, the solution containing the molecules is applied to a grid, then excess liquid is removed by controlled blotting, and the grid is quickly plunged into the cryogen (i.e., liquid ethane at liquid nitrogen temperature) (Lepault et al., 1983). As a result, the molecules are embedded in a thin (~1,000 Å) layer of vitreous ice. Since the fast freezing of the biological specimen takes only a fraction of a millisecond (Cyrklaff et al., 1990), cryo-EM is able, in principle, to capture a pre-equilibrium reaction system as it evolves over a short period of time (e.g., during the span of a second).

The reason why time resolution in the millisecond range is not achievable with the conventional method is that the time for application of the specimen to the grid and the blotting alone takes at least a second. Fast time-resolved cryo-EM techniques (in the range of milliseconds), first developed by Berriman and Unwin (1994), overcome this limitation of conventional methods by spraying one reagent directly onto a grid that has been covered with another reagent and plunging the grid into the cryogen within a short, controlled time. Relatively slow biological processes (over minutes or hours), on the other hand, can be easily studied by conventional EM methods. For example, Mulder et al. (2010) studied assembly of the small ribosomal subunit by negative-staining EM, with time points collected in a range of 1–120 min. Likewise, Fischer et al. (2010) studied reverse translocation of the ribosome by cryo-EM in which specimens with various reaction times from 1 min to 20 min were prepared by the conventional blotting-plunging method.

The purpose of the current study was to explore the performance of a novel method of time-resolved cryo-EM (Lu et al., 2009) in which two components are mixed in a microfluidic device, allowed to react for a defined period of time, and then sprayed onto the EM grid as the latter is being plunged into the cryogen (Figure 1). With this device, reactions within the time frame of a second can be studied at time resolutions reaching 10 ms. The advantage of this mixing-spraying method over the method of Berriman and Unwin (1994) is its capability to study a reaction involving two macromolecules that are completely mixed in solution. The spraying-freezing method of Berriman

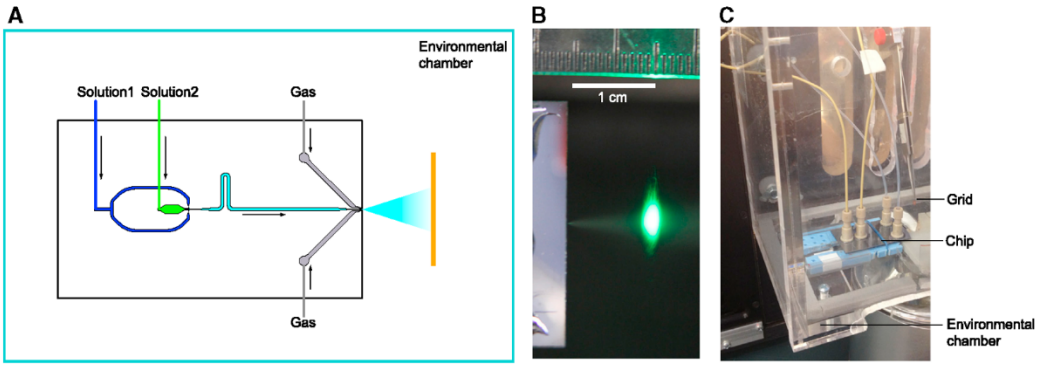

Figure 1. Setup of the Time-Resolved Cryo-EM Apparatus

(A) Schematic view of the mixing-spraying device. The EM grid moves perpendicular to the paper.

(B) Photograph of the spray of droplets illuminated by a green laser at the point just before the grid passes through the spray mist in the direction perpendicular to the paper.

(C) Photograph of the mixing-spraying chip situated inside the environmental chamber.

See also Figure S3.

and Unwin relies on fast diffusion of one of the reagents after spraying to encounter the other reagents already on the grid for starting the reaction. In contrast, the mixing-spraying method that we use in this work allows the reagents to first be completely mixed and the reaction to proceed in a microfluidic channel, where the mixture of reagents is freely drifting and diffusing.

We have applied the mixing-spraying method to study a relatively fast process, the association of the small (30S) and large (50S) ribosomal subunits as they form the 70S ribosome of *Escherichia coli*. This process is a simplified version of the biologically relevant translation initiation process, as it omits mRNA, initiator aminoacyl-tRNA, and all three initiation factors. When the two ribosomal subunits associate, they form several connections, called intersubunit bridges (Frank et al., 1995; Schuwirth et al., 2005; Valle et al., 2003b). The bridges are important for ribosome dynamics and function. For example, some of the bridges break and reform during ribosomal intersubunit rotation, an essential process in the translocation of the mRNA and tRNAs (Valle et al., 2003b). The subunit association process has been characterized by previous biochemical kinetic studies (Antoun et al., 2004; Hennelly et al., 2005; Nguyenle et al., 2006; Wishnia et al., 1975), one of which proposed that the subunits associate via structural intermediates (Hennelly et al., 2005). Nonetheless, the structures of the ribosome that form in the process remain poorly understood.

The kinetics of subunit association has been studied using ensemble chemical protection assays yielding two conflicting interpretations (Hennelly et al., 2005; Nguyenle et al., 2006). Hennelly et al. (2005) proposed that the subunit association is a multistep process. Initially, core bridges B2c and B2a form, followed rapidly by formation of bridge B5, after which the peripheral bridges, such as B7a, are gradually established. According to their model, there should be intermediate conformations of the ribosome in which only subsets of the bridges have formed in the early phase of the reaction. However, Nguyenle et al. (2006) challenged Hennelly and coworkers' interpretation. They asserted that all the eight bridges they studied, including bridges B5 and B7a, exhibit the same rates of formation, implying that subunit association is a simple one-step reaction. It should be noted that both studies are in the time range of between 25 and 50 ms and several seconds. With the capability of capturing time-dependent structural changes and resolving multiple structures of a molecule in one sample, our time-resolved cryo-EM studies of the subunit association reaction can contribute to a resolution of this controversy.

Initial insights into the structural dynamics of subunit association have come from a recent time-resolved cryo-EM study by Shaikh et al. (2014) that favors the interpretation of Hennelly et al. (2005). The authors concluded that bridges B2c, B4, B5, and B6 were missing in the 70S reconstruction from time-resolved cryo-EM data collected at both 9.4 ms and 43 ms. They proposed a kinetic model of subunit association according to which the conserved central bridges (e.g., B2a, B3, and B7b) form first, followed by the formation of non-conserved peripheral bridges (B1a, B1b, and B8), and lastly, by the stabilization of the peripheral end of helix 44. A limitation of this study was the small size of single-particle datasets, resulting in low-resolution reconstructions. In the current work, we have studied this process more extensively, sampling different time points, increasing the resolution by improving the data collection efficiency by a factor of ten, and taking advantage of a new particle classification program (see the section on Strategy for Classification).

In this work, we first improved the mixing-spraying method of Lu et al. (2009) by designing an environmental chamber (Figure 1C) and optimizing the yield of droplets on the EM grid. We also improved the data collection efficiency by using automated data collection with the Leginon software (Suloway et al., 2005), and employed 3D classification and reconstruction of single particles by the Bayesian approach as implemented in the RELION computer program (Scheres, 2011). By mixing the two subunits and reacting for 60 ms and 140 ms, we were able to capture the subunit association reaction in two stages of the reaction before equilibrium and detected three distinct conformations of the 70S

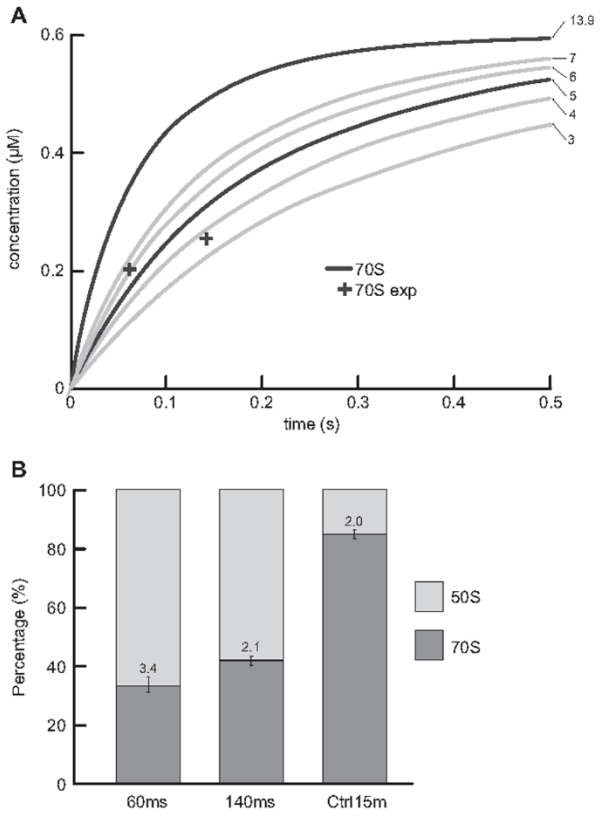

Figure 2. The Proportions of 70S Ribosomes from Various Datasets and a Comparison between the Observed Proportions and the Kinetic Simulations of the Subunit Association Reaction

(A) Comparison between the experimentally observed proportions of 70S ribosomes (cross, 70S exp) and the kinetic simulations of the subunit association reaction (curves). The numbers next to the individual curves indicate the values of the association rate constants (k_a, $\mu M^{-1} s^{-1}$) used in each of the kinetic simulations. k_a was set to 3, 4, 5, 6, and 7 $\mu M^{-1} s^{-1}$ to estimate the value that is most compatible with the experimental results and k_a was set to 13.9 $\mu M^{-1} s^{-1}$ based on previous light-scattering assays (Hennelly et al., 2005).

(B) Proportions of 70S ribosomes and 50S subunits in the 60-ms, 140-ms, and Ctrl 15-min datasets. The errors in the computational classification were estimated from four independent restarts of the RELION 3D classification.

See also Figures S1 and S2.

ribosome. Our results show that all bridges are formed within a 60-ms time frame in the non-rotated form of the ribosome.

Thus, this work demonstrates the capability of the mixing-spraying method to capture the states of macromolecules in a reaction within a sub-second time frame.

RESULTS AND DISCUSSION

Determination of the Reaction Time Window

To choose the proper reaction time for studying ribosome subunit association, we first performed a kinetic simulation of the association reaction 30S + 50S ⇔ 70S. We assumed an association rate constant of k_a = 13.9 $\mu M^{-1} s^{-1}$ based on previous light-scattering assays (Hennelly et al., 2005), and a negligible dissociation rate constant (Wishnia et al., 1975). We chose the concentration of subunits to be 1.2 μM for 30S subunits and 0.6 μM for 50S subunits (after mixing). The choice was made to balance particle density on the grid (favoring a higher concentration for more particles per micrograph and thereby higher data collection efficiency) against sample consumption rate (favoring lower concentration). The simulation results (Figure 2A, k_a = 13.9 $\mu M^{-1} s^{-1}$) indicated that, at the concentration we had chosen, over 90% of the 50S subunits formed 70S ribosome within 200 ms. To capture the reaction in a pre-equilibrium system, and have sufficient data yield for formed 70S particles, we chose the total reaction times of 60 ms and 140 ms (see Supplemental Experimental Procedures, Breakdown of Reaction Time) for our first and second time points in the time-resolved cryo-EM experiment.

We also showed that the purified ribosome subunits are pure and active in peptide synthesis assays (Figures S1 and S2; Supplemental Experimental Procedures, Purity and Activity of Ribosome Subunits).

Optimization of Data Yield and Quality

Low data yield is a major challenge for time-resolved cryo-EM by the mixing-spraying method, because only a small fraction of the EM grid is covered with ice that is thin enough for collecting high-quality images. We were able to improve the data yield by optimizing the protocols for preparing time-resolved cryo-EM specimens and EM data collection. Specifically, we first optimized the size of the droplets and their spreading to increase the area on the EM grid that is suitable for collecting data. We optimized the pressure of the nitrogen gas to yield a dense distribution of small droplets from the spray (Figure 1B). We also plasma cleaned the EM grids immediately before use to ensure that the surface of the carbon-coated grid was hydrophilic, so that the droplets spread thinly on the grid. As a result, the majority of the droplets on the EM grid had a diameter smaller than 50 μm and spread thinly on the EM grids, with a thickness suitable for collecting high-magnification images (Figure S3A). Second, the high yield of suitable droplets enabled us to use the program Leginon (Suloway et al., 2005) for data collection.

The quality of time-resolved cryo-EM high-magnification images is comparable with that of images collected from a control experiment performed by incubating the subunits for 15 min, then preparing the cryo-EM grids using the conventional blotting-plunging method (referred to hereafter as the Ctrl 15-min sample). The time-resolved cryo-EM images are affected negligibly by the ramping effect due to uneven ice thickness, which produces uneven brightness of the images (Figure S3C). As a result, for the 140 ms dataset, we collected 2,586 high-quality micrographs out of a total of 8,797 micrographs from eight time-resolved cryo-EM grids in a total of about 120 hr, and selected 85,880 particles (50S subunits or 70S ribosomes), using the automatic particle selection program Autopicker (Langlois et al., 2014). Similarly, we collected 816 high-quality micrographs for the 60-ms dataset.

Strategy for Classification

At every stage in its time course, a pre-equilibrium system is intrinsically heterogeneous, i.e., it contains molecules differing

in composition and conformation, so there is a need for computational classification to disentangle the different subpopulations, as an essential prerequisite of time-resolved methods of visualization. In order to determine the changes in composition (quantified as 50S subunits versus 70S ribosomes, with 30S subunits in stoichiometric abundance) over time, we pooled the time-resolved 60-ms, time-resolved 140-ms, and Ctrl 15-min datasets into one single dataset (Figure S4A). The purpose of pooling is to ensure that all the data are classified using the same criterion, so that the proportions of subpopulations in the three time points are strictly comparable.

After classification, we tracked the particles corresponding to the associated 70S ribosomes and the 50S subunits back to the individual experiments, and calculated the proportion of the total number of 50S subunits that are found in associated 70S ribosomes (referred to hereafter as the proportion of 70S ribosomes) in each dataset. This proportion is zero at time point 0 and should reach 1 once all 50S subunits are consumed in forming 70S ribosomes.

Time Course of the Subunit Association Reaction

To confirm that the time-resolved cryo-EM method can capture the subunit association reaction in the pre-equilibrium states, we quantified the proportion of 70S ribosomes in the total 50S-containing particles (i.e., 50S subunits and 70S ribosomes) in each dataset. The observed proportions of 70S ribosomes were 33% at 60 ms, 42% at 140 ms, and 85% at 15 min (Ctrl 15 min) (Figure 2B; Table S1). The errors, in the range of 2%–4%, were estimated by comparing the results from four runs of RELION classification and represent the errors in reproducing the proportion of 70S ribosomes with random seeds (i.e., the random assignment of particles into several classes at the start of each classification). Single-tailed t tests show that the increase in the proportion of 70S ribosomes as a function of time is significant ($p = 3 \times 10^{-3}$ for 60-ms versus 140-ms data, $p = 5 \times 10^{-8}$ for 140-ms versus 15-min data, using 0.05 as the level of significance). In comparing the time-resolved datasets with the Ctrl 15-min dataset, however, we must note that the Ctrl 15-min sample was diluted ~20× with buffer after the prolonged 15-min incubation time and prior to grid preparation using the blotting-plunging method. This dilution will shift the 30S + 50S ⇔ 70S equilibrium toward the free 30S and 50S subunits, lowering the equilibrium concentration of the 70S ribosomes. Nonetheless, assuming that all of the subunits are competent to associate into 70S ribosomes and that the Ctrl 15-min sample has reached equilibrium, we can use the proportion of 70S ribosomes in the Ctrl 15-min dataset to estimate the equilibrium dissociation constant (K_D) of the subunit association reaction. Performing this calculation yields a K_D of 6×10^{-9} M, which is within the same order of magnitude as that estimated previously (K_D of ~1×10^{-9} to 4×10^{-9} M at 3–4 mM Mg^{2+}, with K_D presumably leveling off at Mg^{2+} concentrations higher than 4 mM) (Wishnia et al., 1975). Using this estimated K_D and the initial concentrations of 30S and 50S subunits in the 60-ms and 140-ms time-resolved experiments, we could then estimate that, had the time-resolved experiments reached equilibrium, we would expect 99% of the 50S subunits to have associated into 70S ribosomes (see Supplemental Experimental Procedures, Estimation of the Dissociation Constant and the Equilibrium Concentration of 70S Ribosome). Thus, the fact that we observe that only 33% and 42% of the 50S subunits in the 60-ms and 140-ms datasets, respectively, have associated into 70S ribosomes demonstrates that the time-resolved 60-ms and 140-ms samples indeed represent pre-equilibrium states of the subunit association reaction.

Our observed proportions of 70S ribosomes at the three reaction time points follow the same trend with, but are lower than, the values expected from the kinetic simulation (Figure 2A), which are 58% at 60 ms, 83% at 140 ms, and 100% at 15 min. The proportions are more compatible with a k_a value between 4 and 5 $\mu M^{-1} s^{-1}$ than with the previously reported k_a of 13.9 $\mu M^{-1} s^{-1}$ (Hennelly et al., 2005) (Figure 2A), suggesting an approximately 3-fold lower value in the apparent association rate constant estimated from our time-resolved cryo-EM experiments relative to that measured by light-scattering assays (Hennelly et al., 2005).

The difference in the apparent k_a values may be attributable to two possible sources: (1) the existence of a fraction of purified ribosomal subunits that cannot form 70S ribosomes following the kinetics that was characterized by the light-scattering assays in the time range of tens of seconds (Hennelly et al., 2005) but will eventually form 70S ribosomes after a prolonged incubation time of 15 min; (2) the notable differences in the experimental conditions (e.g., buffer composition, temperature), when comparing the light-scattering assays (Hennelly et al., 2005) with our time-resolved cryo-EM experiments. Specifically, the previous light-scattering assays used a Tris-based buffer system at 20°C (Hennelly et al., 2005), while our time-resolved experiments used a HEPES-M12 buffer system at 24°C–26°C (see Supplemental Experimental Procedures, Buffers, Environmental Chamber). Indeed, several research groups have reported different ribosomal subunit association rate constants ranging from 1 to 18 $\mu M^{-1} s^{-1}$, using *E. coli* ribosome subunits in the absence of mRNA and tRNA under a variety of experimental conditions (Antoun et al., 2004; Goerisch et al., 1976; Hennelly et al., 2005; Wishnia et al., 1975). In view of the differences in experimental conditions and the large range of reported values for k_a, the second source of the discrepancy is likely to be more important.

Conformational Differences of 70S Ribosomes

Interestingly, we were able to identify three classes of 70S ribosomes, in addition to a single class of 50S subunit, from the classification (Figure 3). The non-rotated 70S (NR) and rotated 70S (RT) conformations of ribosomes have been observed in previous cryo-EM studies (e.g., Agrawal et al., 1999; Frank and Agrawal, 2000; Valle et al., 2003b). The 30S subunit in the 70S RT conformation has undergone an ~8° counterclockwise rotation compared with the 70S NR conformation, as viewed from the 30S subunit side (Figure 3C, side view). The third class of 70S ribosomes is termed "non-rotated 70S with 30S head swivel" (NRS 70S) because the orientation of the 30S subunit body relative to the 50S subunit is identical to that in the NR 70S conformation, while the 30S subunit head domain is swiveled (~4°) counterclockwise when viewed from the top of the ribosome, compared with its position in the NR 70S (Figure 3B, top view).

All the intersubunit bridges are present in the NR 70S and most of the bridges are present in the NRS 70S and RT 70S (Figure 4;

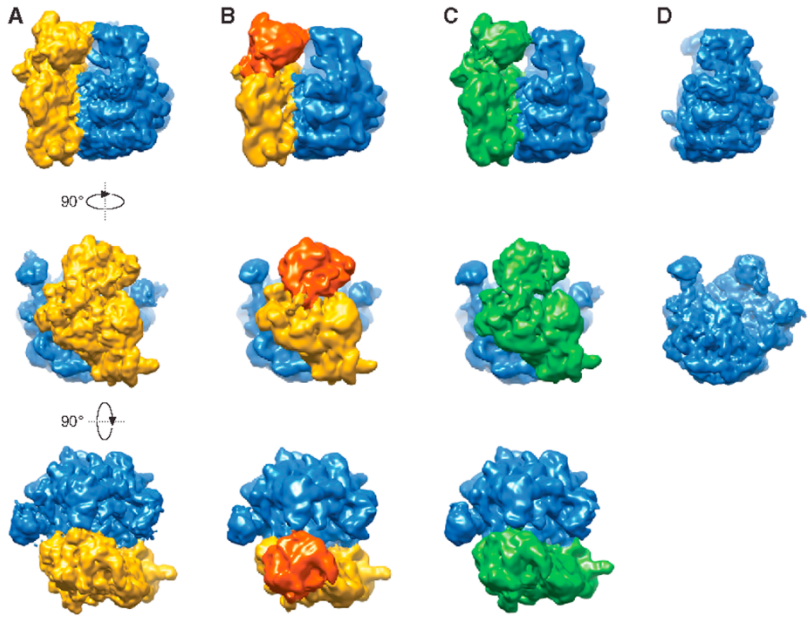

Figure 3. Cryo-EM Maps of 70S in Three Conformations and 50S from the Experiments

(A) Non-rotated 70S ribosome (NR).
(B) Non-rotated 70S ribosome with 30S head swivel (NRS).
(C) Rotated 70S ribosome (RT).
(D) 50S ribosome subunit.
See also Figure S4.

Table 1). To verify that all of the bridges have formed in NR 70S as early as 60 ms, we performed 3D reconstruction on the 70S particles corresponding to the NR 70S conformation from only the time-resolved 60-ms dataset (5,499 particles). This reconstruction shows clear density for helix 44 in the 30S subunit, as well as bridges B2a, B3, B5, B6a, and B6b along helix 44 (Figure S5), indicating that all of the intersubunit bridges are formed in NR 70S by the time 60 ms is reached. The NRS 70S ribosome lacks bridge B1a and has weak density of B1b compared with NR 70S. On the other hand, the RT 70S ribosome lacks bridges B1a and has weak density for B6b. The bridge B1b in the RT 70S ribosome appears rearranged compared with the NR 70S ribosome. Bridge B6b at the distal end of helix 44 of the 30S subunit is likely disrupted and rearranged during the intersubunit rotation in the RT 70S ribosome.

Our observation that the associated 70S ribosomes exist in three conformations suggests that intersubunit rotation and 30S head swiveling represent intrinsic motions of associated 70S ribosomes that lack any bound mRNA and/or tRNAs. In an attempt to elucidate the order in which ribosomal conformational changes take place during subunit association, we compared the proportion of 70S ribosomes in different conformations as a function of the reaction time.

Quantifying the Percentages of Ribosome in Different Conformations

We quantified the proportion of 70S ribosomes in each conformation in the total 70S ribosomes for individual datasets (Figure 5; Table S2). In comparing the proportions of the three conformations in the 60-ms and 140-ms datasets, we find that they are quite similar, with approximately 60% NR 70S, 30% NRS 70S, and 10% RT 70S. Single-tailed t tests yield $p = 0.5$ for NR 70S, $p = 0.2$ for NRS 70S, and $p = 2 \times 10^{-3}$ for RT 70S conformations. In contrast, comparing the proportions in the 140 ms with those in the Ctrl 15-min dataset, we find that they appear to differ for all three conformations, with NR 70S decreasing and the other two conformations increasing with time. Single-tailed t tests yield $p = 5 \times 10^{-3}$ for NR 70S, $p = 6 \times 10^{-3}$ for NRS 70S, and $p = 2 \times 10^{-4}$ for RT 70S conformations. However, we note that the 3D classification process may be less accurate in distinguishing among the three 70S ribosome conformations than in distinguishing between 70S ribosomes and 50S subunits, a fact that is reflected in the larger errors for the former relative to the latter (Figures 2B and 5). This difference in accuracy is most likely attributable to the nature of the differences among the reconstructions; the 70S ribosome and 50S subunit have a massive, easily detectable compositional difference, whereas the various 70S ribosome conformations present more subtle conformational differences that are primarily confined to the peripheral region of the ribosome. Based on this limitation, we regard the change in the proportion of RT 70S from 60 ms to 140 ms as within margins of error, in particular because the proportion is rather small (~10%).

In addition to the potential inaccuracies associated with distinguishing between the three 70S ribosome conformations, the differences in proportions of 70S conformations between the time-resolved and 15-min datasets may be attributable to the different grid preparation procedures for the time-resolved experiments relative to the Ctrl 15-min experiment (see Experimental Procedures). Factors that may affect the kinetics of the transitions among the 70S conformations include the interactions of ribosomes with the carbon support film and/or the air-water interface, as suggested in previous studies (Lu et al., 2009), and the ~20× dilution of the ribosome sample required for the blotting-plunging method. The potential effects of different grid preparation procedures on these possibly grid-specific transition kinetics warrant further study. Regardless, based on the similarity of the proportions of 70S ribosome conformations at 60 ms and 140 ms, we propose that the conformational changes in the 70S ribosome (i.e., intersubunit rotation and 30S head swivel) are likely to have reached equilibrium before the first time point in our experiment (60 ms). Future mixing-spraying time-resolved cryo-EM experiments collected at earlier time points will be needed to test this hypothesis and determine the relative timing with which these conformational changes occur during the formation of 70S ribosomes from 30S and 50S subunits.

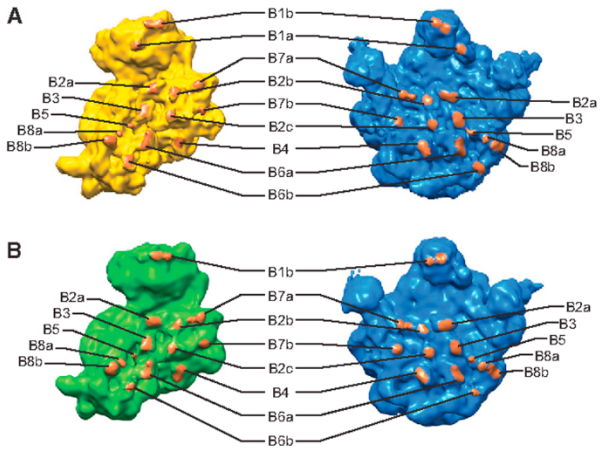

Figure 4. Intersubunit Bridges in the 70S Ribosomes

(A) Segmentation of the 70S NR map showing the bridges that are present in 70S NR map.

(B) Segmentation of the 70S RT map showing the bridges that are present in 70S RT map.

See also Figure S5 and Table 1.

Table 1. Presence of Intersubunit Bridges in Different Conformations of 70S Ribosome; Related to Figure 4

Bridge[a]	NR	NRS	RT
B1a	+	–	–
B1b	+	+	+
B2a	+	+	+
B2b	+	+	+
B2c	+	+	+
B3	+	+	+
B4	+	+	+
B5	+	+	+
B6a	+	+	+
B6b	+	+	–[b]
B7a	+	+	+
B7b	+	+	+
B8a	+	+	+
B8b	+	+	+

[a]Bridge assignment is based on Dunkle et al. (2011), Gabashvili et al. (2000), Schuwirth et al. (2005), and Yusupov et al. (2001).

[b]Bridge B6b has weak density in the 70S RT conformation.

Model of the Structural Dynamics of Ribosome Subunit Association

Our study unveils multiple conformations of the vacant (i.e., lacking bound mRNA and tRNAs) 70S ribosome during the early phase (i.e., pre-equilibrium) of ribosome subunit association and the proportions of ribosomes in these conformations. Based on these structural and quantitative observations, we propose a structural dynamic model of subunit association: (1) upon initial subunit association, the 70S ribosomes can rapidly interconvert among the NR 70S, NRS 70S, and RT 70S conformations and reach equilibrium among these three conformations earlier than the first time point we studied (60 ms). (2) The 30S head is able to swivel in the non-rotated 70S ribosome conformation, which is indicated by the observation that the 30S subunit body domains in the NR 70S and NRS 70S maps overlap but their 30S subunit head domains exhibit different conformations distinguishable at the current resolution (9–12 Å). However, we did not observe different extents of 30S head swiveling in the rotated 70S ribosome. The fact that we had only 11,000 particles corresponding to RT 70S may have limited our ability to distinguish more subtle differences, such as 30S head swiveling, in the RT 70S. Comparison of our observations on the vacant ribosomes with the previous cryo-EM and crystallography studies in the presence of mRNA and tRNAs (Agirrezabala et al., 2012; Ratje et al., 2010; Valle et al., 2003b; Zhou et al., 2013) highlights the importance of mRNA and tRNAs in defining and modulating the dynamics of the 30S head. (3) The rotated conformation of 70S ribosome, RT 70S, is likely less energetically stable than the non-rotated conformations, which is indicated by the low proportion of RT 70S in our studies (10%–20% at each reaction time). Future studies are needed to answer the questions on how the buffer conditions, as well as the presence of mRNA, tRNAs, and initiation factors during translation initiation, affect the distribution of the intermediate conformations of the ribosome and the dynamics of interconversions among these intermediates.

The model presented in the previous paragraph is consistent with observations from single-molecule fluorescence resonance energy transfer (FRET) studies demonstrating that the vacant 70S ribosomes strongly prefer to occupy the non-rotated state and rarely undergo transient excursions to the rotated state (Cornish et al., 2008, 2009; Ning et al., 2014). Indeed, our conclusion that 70S ribosomes rapidly equilibrate between non-rotated and rotated conformations is strongly supported by the fact that the proportion of rotated 70S at 60-ms reaction time in our study (11%) mirrors that in the fully equilibrated smFRET experiments (15%–21%) (Cornish et al., 2008, 2009; Ning et al., 2014). Combining our time-resolved cryo-EM observations and smFRET observations, it is likely that the 70S ribosomes that initially associate in the rotated conformation will rapidly convert to the lower-energy, more stable non-rotated conformation (either NR or NRS) within tens of milliseconds. In contrast, the 70S ribosomes that initially associate in the non-rotated conformation will remain in the non-rotated conformation and rarely convert to the rotated conformation.

Our model is also in good agreement with that proposed from ensemble kinetic studies by the Noller group (Nguyenle et al., 2006) and provides more microscopic details since we were able to resolve multiple conformations. We did not observe that the intersubunit bridges form in a stepwise manner, as proposed by Hennelly et al. (2005). Instead, the 70S NR conformation has all the bridges formed and the missing bridges in NRS and RT conformations are readily explained by the large-scale changes in the subunit-subunit interactions accompanying intersubunit rotation and/or 30S head swiveling.

Our observations and the proposed model exhibit several differences compared with the results of a previous time-resolved cryo-EM study of subunit association (Shaikh et al., 2014), despite the fact that both studies used the same buffer

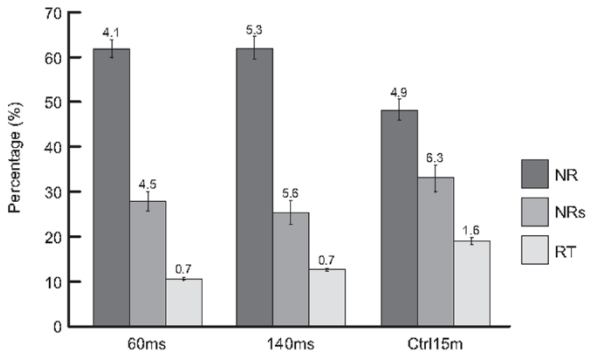

Figure 5. Proportions of 70S Ribosomes in Different Conformations from the Various Datasets

Three conformations of 70S ribosomes were observed: rotated (RT), non-rotated with 30S head swivel (NRS), and non-rotated (NR). The errors in the computational classification were estimated from four independent restarts of the RELION 3D classification.

See also Table S2.

composition, similar ribosomal subunit purification procedures, and the same mixing-spraying chip design (for our 60-ms experiment and their 43-ms experiment). The only difference in the experimental setup is the addition of an environmental chamber in our experiments and, consequently, our plunging time (18 ms) is longer than theirs (5 ms) (see Supplemental Information for additional comparison).

While Shaikh et al. (2014) concluded that bridges B2c, B4, B5, and B6 form later than 43 ms, our 60-ms dataset yielded an NR 70S ribosome containing all the bridges, including these four. One possible reason for the difference between our observations and theirs may be the different activities of the ribosome samples. A second possible reason may be the difference in plunging time. A drastic climate change happens to the ribosome sample during the plunging, from room-temperature humid air to near-liquid-nitrogen-temperature dry air, and the effects of such climate change on the kinetics of 70S ribosome formation from 30S and 50S subunits are not well understood. However, a third possible reason is the difference in the resolution of the maps, with 23–33 Å in their study versus 9–12 Å in ours (Figures S4B–S4D). The higher resolution of our maps stems from our improved data yield and allows us to detect the intersubunit bridges with more confidence. Future time-resolved cryo-EM studies of ribosome subunit association containing additional time points at sufficiently high resolution will be needed to resolve this discrepancy.

To sum up, in this study we used the mixing-spraying method of time-resolved cryo-EM to study ribosomal subunit association within a tens of millisecond timescale and were able to capture pre-equilibrium states of this association reaction. In addition, we revealed three conformations of the 70S ribosome formed in the early phase (i.e., pre-equilibrium) of the association reaction. Quantification of the proportions of 70S ribosomes in these conformations suggested that, upon formation, the 70S ribosomes rapidly equilibrates among these conformations on a timescale faster than 60 ms. The observed large-scale conformational changes of the vacant ribosome (i.e., in the absence of tRNAs and mRNA), namely the rotation of the 30S subunit and the swiveling of the 30S subunit head, likely represent spontaneous thermal motions of the 70S ribosome (Frank and Gonzalez, 2010).

In the future, it will be interesting to study translation initiation using this method of time-resolved cryo-EM to shed light on the role of mRNA, initiator tRNA, and initiation factors on the structural dynamics of the subunit association reaction. The mixing-spraying method can also be applied to a wide variety of reactions involving ribosomes, including aminoacyl-tRNA selection, translocation, termination, and ribosome recycling.

EXPERIMENTAL PROCEDURES

Mixing-Spraying Device

This device, developed by Lu et al. (2009), is a small silicon chip containing nano-fabricated channels, which combines the functionalities of mixing, reacting, and spraying (Figure 1). The two solutions are injected into the chip by syringes and mixed passively by turbulence (within 0.5 ms at a total flow rate of 6 μl/s). The mixture reacts for a certain time while flowing through the channel, then it is made into spray at the outlet nozzle where it meets the compressed nitrogen gas. In this work, we used chips with mean reaction times of 38 and 107 ms.

Environmental Chamber

We designed an environmental chamber to monitor and maintain the temperature and humidity during the time the time-resolved cryo-EM grid is sprayed and plunged (Figure 1C). The environmental chamber is connected to a water tank, which is equipped with a sonicator and an air pump to generate humidified air. During the experiment, the ambient conditions can be maintained at 24°C–26°C and 80%–90% relative humidity (equivalent to 0.016–0.018 g of water per gram of dry air).

Preparation of Time-Resolved Cryo-EM Grids

The ribosome subunit association reaction was performed using the mixing-spraying device as previously described (Lu et al., 2009) with some alterations. Specifically, Quantifoil R2/2 300 mesh Cu EM grids were carbon coated, then glow discharged within 3 hr before grid preparation, using a Gatan Solarus 950 with H_2 at a flow rate of 6.4 standard cubic centimeters per minute (sccm) and O_2 at a flow rate of 27.5 sccm at 25 W for 25 s. Equal volumes of 1.2 μM 30S and 0.6 μM 50S (final concentration after mixing) were injected into the mixing-spraying device each at a flow rate of 3 μl/s. Compressed nitrogen gas was kept at 3.4×10^5 Pa and humidified by passing through two consecutive water tanks. The computer-controlled plunging device was purchased from Dr. Howard White (Eastern Virginia Medical School).

Collection of Time-Resolved Cryo-EM Data Using the Leginon Program

The cryo-EM data were collected, as previously described (Grassucci et al., 2008), in low-dose mode on an FEI Tecnai F20 TEM at 200-kV extraction voltage with the automated image collection program Leginon (Suloway et al., 2005). Micrographs were recorded on a Gatan UltraScan 4000 charge-coupled device (CCD) camera with effective CCD magnification of 66,813× and pixel size of 2.25 Å on the object scale. For the time-resolved cryo-EM specimens, only the holes close to the edge of an ice blot are suitable for collecting high-magnification images.

3D Classification Using RELION

In the classification of single particles to identify 70S ribosomes in different conformations, the datasets of time-resolved 60 ms, time-resolved 140 ms, and Ctrl 15 min were pooled together for classification and 3D reconstructions, so that all the individual datasets were classified using the same criteria, and therefore the classification results (i.e., the relative proportion of each conformation) among the datasets were comparable. The 50S and 70S particles were then traced back to each experiment to quantify the proportion of 70S in 50S-containing particles and the proportion of each 70S conformation in

the total 70S particles. We used the RELION program (Scheres, 2012) in a stepwise hierarchical classification to discard bad particles identified by the automatic particle-picking program, separate the 50S subunit from the 70S ribosome, and sort out the various conformations of the 70S ribosome assisted by visual examination of the reconstructions (Figure S4A). Specifically, the reference volume for the initial alignment of the total set of putative particles was chosen to be a 50S subunit density map (the cryo-EM map of empty 70S ribosome [Valle et al., 2003a] with 30S subunit computationally removed) low-pass filtered to 60 Å. We used the particle data in un-decimated form in the 3D classification as well as in the final steps of 3D reconstruction and refinement.

In step (1), the datasets of time-resolved 60 ms (after discarding bad particles, 38,316 particles), time-resolved 140 ms (82,574 particles), and Ctrl 15 min (55,369 particles) were combined to form the total dataset (176,259 particles) (Figure S4A). In step (2), the total dataset was separated into ten classes using the RELION 3D classification. The classification results were analyzed using a novel quantitative analysis method (Chen et al., 2014; Shen et al., 2014) and the reconstructions from the different classes were visually examined by using the UCSF Chimera program (Pettersen et al., 2004). The classes yielding a reconstruction of 70S ribosome (94,860 particles) were kept for step (3) of the classification. The classes yielding a reconstruction of 50S subunit (81,399 particles) were kept for refinement in step (4). In step (3), the classes yielding 70S reconstructions (94,860 particles) were classified into eight classes. The classes resulting in bad reconstructions, likely due to the remaining unrecognizable particles, were discarded, keeping 75,254 particles of 70S ribosomes. The remaining classes were visually examined by using UCSF Chimera and regrouped based on the conformation of their resulting reconstructions: NR (39,678 particles), NRS (24,447 particles), and RT (11,129 particles). In step (4), each class of 70S ribosomes or 50S subunits was refined using RELION 3D auto-refinement (Scheres, 2012) with data in un-decimated form. In step (5), the particles were traced back to each experiment to quantify the proportion of 70S and the proportion of 70S in each conformation. Steps (2)–(5) were repeated three more times to estimate the error of the 3D classification process.

Resolution Measurement

We assessed the resolutions of the reconstructions of 70S ribosomes in their different conformations and the 50S subunit from step (4) using the gold-standard criterion (Scheres and Chen, 2012). For each of the classes, we first performed RELION 3D auto-refinement separately on two randomly split half datasets following the gold-standard protocol, yielding two unfiltered volumes. Then we multiplied these two unfiltered volumes with a soft Gaussian mask having 0.5 fall-off at 5 pixels (11.2 Å) outside the ribosome, to eliminate peripheral noise. We then calculated the Fourier shell correlation (FSC) between the two masked volumes (Figures S4B–S4D), and used the FSC = 0.143 criterion to determine the gold-standard resolution as 9.7 Å (70S NR), 11.1 Å (70S NRS), 11.6 Å (70S RT), 9.5 Å (50S).

Identification of Intersubunit Bridges in the Cryo-EM Maps of the 70S Ribosome

First, for comparison with each cryo-EM map of the 70S ribosome in this study, a simulated density map of the 70S ribosome was generated from crystallographic structures (PDB: 2AVY, 2AW4, the non-rotated 70S ribosome, for comparison with both 70S NR and 70S NRS; PDB: 2AW7, 2AWB, the rotated 70S ribosome, for comparison with 70S RT) and low-pass filtered to 10-Å resolution. Second, to bring the simulated density map and our cryo-EM map of the 70S ribosome into register, the 50S portions of the two simulated maps were fitted into the corresponding 50S subunit density map in this study using the Fit in Map tool in USCF Chimera (Pettersen et al., 2004), the rationale being that the 50S subunit is larger and more stable than the 30S subunit. Also, the surface regions around ribosomal proteins L4, L15, and L21, which have pronounced features, were visually inspected to check the alignment of the map from fitting results. Third, the threshold of the simulated density map was adjusted to a level such that the contour of the simulated map just enclosed all the atoms in the crystallographic structure, using default values in Chimera of van der Waals radii for atoms of C, O, N, P, and S. Specifically, the threshold level was adjusted such that the surface regions around ribosomal proteins L4, L15, and L21 were enclosed within the contour. Fourth, the cryo-EM map was segmented into 30S and 50S subunit density maps. The segmentation reveals the boundaries of the subunits, and hence facilitates locating the bridging contacts on the intersubunit interface. The locations of bridges identified in cryo-EM (Gabashvili et al., 2000) and crystallographic structures (Dunkle et al., 2011; Schuwirth et al., 2005; Yusupov et al., 2001) were marked in our segmented density maps using the Volume Tracer tool in Chimera and the connectivity of densities linking 30S and 50S subunits was inspected at each point.

ACCESSION NUMBERS

The electron microscopy maps have been deposited in the EMBL-European Bioinformatics Institute EM Data Bank under accession codes EMD: 2976, 2977, and 2978 (70S NR, NRS, RT maps, respectively).

SUPPLEMENTAL INFORMATION

Supplemental Information includes Supplemental Experimental Procedures, five figures, and two tables and can be found with this article online at http://dx.doi.org/10.1016/j.str.2015.04.007.

AUTHOR CONTRIBUTIONS

B.C., R.L.G., and J.F. designed the experiments. Z.L., D.B., and T.-M. L. provided the mixing-spraying chips and training to B.C. on the time-resolved cryo-EM method. B.C. performed the kinetic simulation and biochemical experiments and improved the time-resolved cryo-EM method. B.C., S.K., M.S., and B.S. collected time-resolved cryo-EM data. B.C., M.S., and B.S. analyzed the initial cryo-EM datasets. S.K. and B.C. analyzed the final cryo-EM datasets. B.C., S.K., R.L.G., and J.F. wrote the manuscript. All authors approved the final manuscript.

ACKNOWLEDGMENTS

We thank R. Grassucci for assistance with cryo-EM data collection, Dr. H. White for help with installing the plunging device and with the design of the environmental chamber, K.M. Headley for assistance with the initial stage of methodology improvement, and M. Thomas-Baum for assistance with the preparation of the figures. This work was supported by the Howard Hughes Medical Institute and NIH grants R01 GM55440 and GM29169 to J.F. and by NIH grant R01GM084288 to R.L.G.

Received: December 6, 2014
Revised: March 16, 2015
Accepted: April 5, 2015
Published: May 21, 2015

REFERENCES

Agirrezabala, X., Liao, H.Y., Schreiner, E., Fu, J., Ortiz-Meoz, R.F., Schulten, K., Green, R., and Frank, J. (2012). Structural characterization of mRNA-tRNA translocation intermediates. Proc. Natl. Acad. Sci. USA *109*, 6094–6099.

Agrawal, R.K., Heagle, A.B., Penczek, P., Grassucci, R.A., and Frank, J. (1999). EF-G-dependent GTP hydrolysis induces translocation accompanied by large conformational changes in the 70S ribosome. Nat. Struct. Biol. *6*, 643–647.

Antoun, A., Pavlov, M.Y., Tenson, T., and Ehrenberg, M. (2004). Ribosome formation from subunits studied by stopped-flow and Rayleigh light scattering. Biol. Proced. Online *6*, 35–54.

Berriman, J., and Unwin, N. (1994). Analysis of transient structures by cryo-microscopy combined with rapid mixing of spray droplets. Ultramicroscopy *56*, 241–252.

Blanchard, S.C., Gonzalez, R.L., Kim, H.D., Chu, S., and Puglisi, J.D. (2004). tRNA selection and kinetic proofreading in translation. Nat. Struct. Mol. Biol. *11*, 1008–1014.

Chen, B., Shen, B., and Frank, J. (2014). Particle migration analysis in iterative classification of cryo-EM single-particle data. J. Struct. Biol. *188*, 267–273.

Cornish, P.V., Ermolenko, D.N., Noller, H.F., and Ha, T. (2008). Spontaneous intersubunit rotation in single ribosomes. Mol. Cell *30*, 578–588.

Cornish, P.V., Ermolenko, D.N., Staple, D.W., Hoang, L., Hickerson, R.P., Noller, H.F., and Ha, T. (2009). Following movement of the L1 stalk between three functional states in single ribosomes. Proc. Natl. Acad. Sci. USA *106*, 2571–2576.

Cyrklaff, M., Adrian, M., and Dubochet, J. (1990). Evaporation during preparation of unsupported thin vitrified aqueous layers for cryo-electron microscopy. J. Electron. Microsc. Tech. *16*, 351–355.

Diez, M., Zimmermann, B., Borsch, M., Konig, M., Schweinberger, E., Steigmiller, S., Reuter, R., Felekyan, S., Kudryavtsev, V., Seidel, C.A., et al. (2004). Proton-powered subunit rotation in single membrane-bound F_0F_1-ATP synthase. Nat. Struct. Mol. Biol. *11*, 135–141.

Dilger, J.P., and Brett, R.S. (1990). Direct measurement of the concentration- and time-dependent open probability of the nicotinic acetylcholine receptor channel. Biophys. J. *57*, 723–731.

Dunkle, J.A., Wang, L., Feldman, M.B., Pulk, A., Chen, V.B., Kapral, G.J., Noeske, J., Richardson, J.S., Blanchard, S.C., and Cate, J.H.D. (2011). Structures of the bacterial ribosome in classical and hybrid states of tRNA binding. Science *332*, 981–984.

Fischer, N., Konevega, A.L., Wintermeyer, W., Rodnina, M.V., and Stark, H. (2010). Ribosome dynamics and tRNA movement by time-resolved electron cryomicroscopy. Nature *466*, 329–333.

Frank, J., and Agrawal, R.K. (2000). A ratchet-like inter-subunit reorganization of the ribosome during translocation. Nature *406*, 318–322.

Frank, J., and Gonzalez, J.R.L. (2010). Structure and dynamics of a processive Brownian motor: the translating ribosome. Annu. Rev. Biochem. *79*, 381–412.

Frank, J., Verschoor, A., Li, Y., Zhu, J., Lata, R.K., Radermacher, M., Penczek, P., Grassucci, R., Agrawal, R.K., and Srivastava, S. (1995). A model of the translational apparatus based on a three-dimensional reconstruction of the *Escherichia coli* ribosome. Biochem. Cell Biol. *73*, 757–765.

Gabashvili, I.S., Agrawal, R.K., Spahn, C.M.T., Grassucci, R.A., Svergun, D.I., Frank, J., and Penczek, P. (2000). Solution structure of the *E. coli* 70S ribosome at 11.5 Å resolution. Cell *100*, 537–549.

Goerisch, H., Goss, D.J., and Parkhurst, L.J. (1976). Kinetics of ribosome dissociation and subunit association studied in a light-scattering stopped-flow apparatus. Biochemistry *15*, 5743–5753.

Grassucci, R.A., Taylor, D., and Frank, J. (2008). Visualization of macromolecular complexes using cryo-electron microscopy with FEI Tecnai transmission electron microscopes. Nat. Protoc. *3*, 330–339.

Hennelly, S.P., Antoun, A., Ehrenberg, M., Gualerzi, C.O., Knight, W., Lodmell, J.S., and Hill, W.E. (2005). A time-resolved investigation of ribosomal subunit association. J. Mol. Biol. *346*, 1243–1258.

Johansson, M., Lovmar, M., and Ehrenberg, M. (2008). Rate and accuracy of bacterial protein synthesis revisited. Curr. Opin. Microbiol. *11*, 141–147.

Langlois, R., Pallesen, J., Ash, J.T., Nam Ho, D., Rubinstein, J.L., and Frank, J. (2014). Automated particle picking for low-contrast macromolecules in cryo-electron microscopy. J. Struct. Biol. *186*, 1–7.

Lepault, J., Booy, F.P., and Dubochet, J. (1983). Electron microscopy of frozen biological suspensions. J. Microsc. *129*, 89–102.

Lu, Z., Shaikh, T.R., Barnard, D., Meng, X., Mohamed, H., Yassin, A., Mannella, C.A., Agrawal, R.K., Lu, T.-M., and Wagenknecht, T. (2009). Monolithic microfluidic mixing-spraying devices for time-resolved cryo-electron microscopy. J. Struct. Biol. *168*, 388–395.

Matsubara, N., Billington, A.P., and Hess, G.P. (1992). How fast does an acetylcholine receptor channel open? Laser-pulse photolysis of an inactive precursor of carbamoylcholine in the microsecond time region with BC3H1 cells. Biochemistry *31*, 5507–5514.

Mulder, A.M., Yoshioka, C., Beck, A.H., Bunner, A.E., Milligan, R.A., Potter, C.S., Carragher, B., and Williamson, J.R. (2010). Visualizing ribosome biogenesis: parallel assembly pathways for the 30S subunit. Science *330*, 673–677.

Nguyenle, T., Laurberg, M., Brenowitz, M., and Noller, H.F. (2006). Following the dynamics of changes in solvent accessibility of 16 S and 23 S rRNA during ribosomal subunit association using synchrotron-generated hydroxyl radicals. J. Mol. Biol. *359*, 1235–1248.

Ning, W., Fei, J., and Gonzalez, R.L., Jr. (2014). The ribosome uses cooperative conformational changes to maximize and regulate the efficiency of translation. Proc. Natl. Acad. Sci. USA *111*, 12073–12078.

Pettersen, E.F., Goddard, T.D., Huang, C.C., Couch, G.S., Greenblatt, D.M., Meng, E.C., and Ferrin, T.E. (2004). UCSF Chimera—a visualization system for exploratory research and analysis. J. Comput. Chem. *25*, 1605–1612.

Ratje, A.H., Loerke, J., Mikolajka, A., Brunner, M., Hildebrand, P.W., Starosta, A.L., Donhofer, A., Connell, S.R., Fucini, P., Mielke, T., et al. (2010). Head swivel on the ribosome facilitates translocation by means of intra-subunit tRNA hybrid sites. Nature *468*, 713–716.

Rodnina, M.V., Gromadski, K.B., Kothe, U., and Wieden, H.J. (2005). Recognition and selection of tRNA in translation. FEBS Lett. *579*, 938–942.

Scheres, S.H.W. (2011). A Bayesian view on cryo-EM structure determination. J. Mol. Biol. *415*, 406–418.

Scheres, S.H. (2012). RELION: implementation of a Bayesian approach to cryo-EM structure determination. J. Struct. Biol. *180*, 519–530.

Scheres, S.H., and Chen, S. (2012). Prevention of overfitting in cryo-EM structure determination. Nat. Methods *9*, 853–854.

Schuwirth, B.S., Borovinskaya, M.A., Hau, C.W., Zhang, W., Vila-Sanjurjo, A., Holton, J.M., and Cate, J.H.D. (2005). Structures of the bacterial ribosome at 3.5 Å resolution. Science *310*, 827–834.

Shaikh, T.R., Yassin, A.S., Lu, Z., Barnard, D., Meng, X., Lu, T.-M., Wagenknecht, T., and Agrawal, R.K. (2014). Initial bridges between two ribosomal subunits are formed within 9.4 milliseconds, as studied by time-resolved cryo-EM. Proc. Natl. Acad. Sci. USA *111*, 9822–9827.

Shen, B., Chen, B., Liao, H., and Frank, J. (2014). Quantitative analysis in iterative classification schemes for cryo-EM applications. In Computational Methods for Three-Dimensional Microscopy Reconstruction, G.T. Herman and J. Frank, eds. (Birkhauser).

Suloway, C., Pulokas, J., Fellmann, D., Cheng, A., Guerra, F., Quispe, J., Stagg, S., Potter, C.S., and Carragher, B. (2005). Automated molecular microscopy: the new Leginon system. J. Struct. Biol. *151*, 41–60.

Valle, M., Zavialov, A., Li, W., Stagg, S.M., Sengupta, J., Nielsen, R.C., Nissen, P., Harvey, S.C., Ehrenberg, M., and Frank, J. (2003a). Incorporation of aminoacyl-tRNA into the ribosome as seen by cryo-electron microscopy. Nat. Struct. Mol. Biol. *10*, 899–906.

Valle, M., Zavialov, A., Sengupta, J., Rawat, U., Ehrenberg, M., and Frank, J. (2003b). Locking and unlocking of ribosomal motions. Cell *114*, 123–134.

Wishnia, A., Boussert, A., Graffe, M., Dessen, P., and Grunberg-Manago, M. (1975). Kinetics of the reversible association of ribosomal subunits: stopped-flow studies of the rate law and of the effect of Mg^{2+}. J. Mol. Biol. *93*, 499–515.

Yusupov, M.M., Yusupova, G.Z., Baucom, A., Lieberman, K., Earnest, T.N., Cate, J.H., and Noller, H.F. (2001). Crystal structure of the ribosome at 5.5 Å resolution. Science *292*, 883–896.

Zhou, J., Lancaster, L., Donohue, J.P., and Noller, H.F. (2013). Crystal structures of EF-G–ribosome complexes trapped in intermediate states of translocation. Science *340*, 1236086.

Structure, Volume *23*

Supplemental Information

Structural Dynamics of Ribosome Subunit Association Studied by Mixing-Spraying Time-Resolved Cryogenic Electron Microscopy

Bo Chen, Sandip Kaledhonkar, Ming Sun, Bingxin Shen, Zonghuan Lu, David Barnard, Toh-Ming Lu, Ruben L. Gonzalez, and Joachim Frank

SUPPLEMENTAL INFORMATION

SUPPLEMENTAL FIGURES and LEGENDS

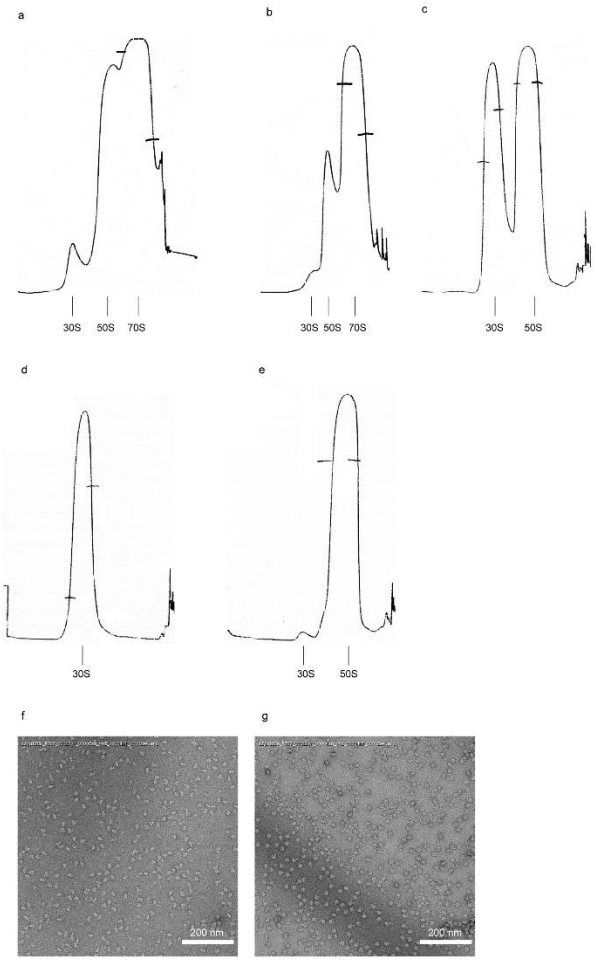

Figure S1. Ribosome subunit purification. Related to **Figure 2**. (a, b) Profiles of the first and second round of sucrose gradient in the presence of 7.5 mM Mg^{2+} to isolate tight-coupled 70S ribosome. (c) Profile of the third round of sucrose gradient in the presence of

1.0 mM Mg^{2+} to split tight-coupled 70S ribosome into 30S and 50S subunits. (d, e) Profiles of the fourth round of sucrose gradient in the presence of 1.0 mM Mg^{2+} to isolate 30S subunit and 50S subunit, respectively. (f, g) EM images of negatively stained samples of 30S subunits and 50S subunits, respectively.

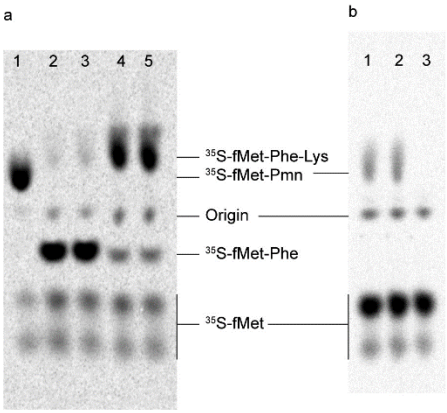

Figure S2. Translation activity assays for the associated ribosome complex. Related to **Figure 2**. (a) Tripeptide formation assay for the associated ribosome formed from the purified 30S and 50S subunits (see Experimental Procedures for details). Lane 1: added puromycin (Pmn) to the 70S initiation complex (IC), and incubated at 37°C for 1 min. Lanes 2 and lane 3: added ternary complexes of $tRNA^{Phe}$ and $tRNA^{Lys}$ in the absence of EF-G, and incubated at 37°C for 1 min and 2 min, respectively. Lanes 4 and lane 5: added ternary complexes in the presence of EF-G, and incubated at 37°C for 1 min and 2 min, respectively. (b) Comparison of activity of ribosomes mixed in time-resolved mixing-spraying device versus mixed by pipetting (see Experimental Procedures for details). Lane 1: used 30S/50S mixture collected from the mixing-spraying device to form the 70S translation initiation complex, then added puromycin and incubated at 37°C for 1 min. Lane 2: used the 30S/50S mixture resulting from gently pipetting to form the 70S translation initiation complex, then added puromycin and incubated at 37°C for 1 min. Lane 3: same as lane 1 except done in the absence of puromycin.

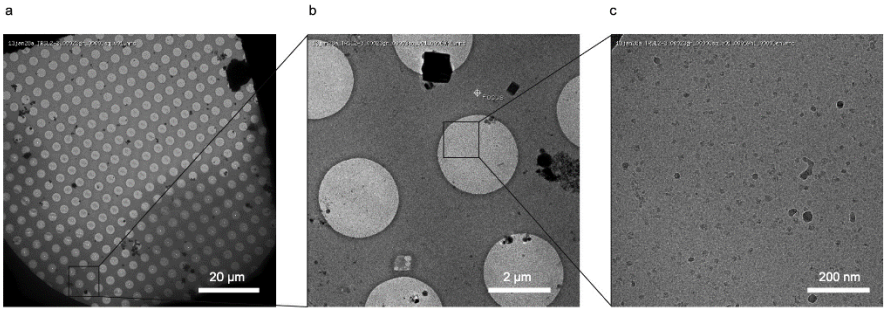

Figure S3. Example of time-resolved cryo-EM images collected using Leginon program. Related to **Figure 1**. (a, b, c) Successive zoom-ins of boxed region in the previous EM image. The ramping effect due to uneven ice thickness, which results in uneven brightness of the image, is negligible in hole (b) and high-magnification (c) images.

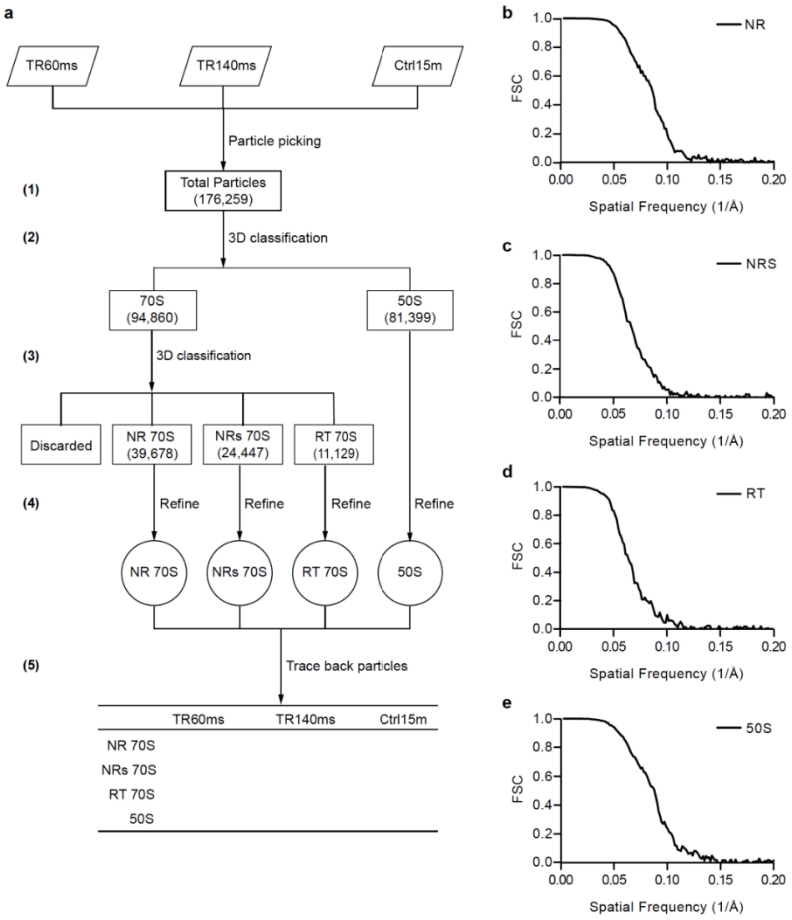

Figure S4. Schematic of single-particle analysis and classification, and the FSC curve for each class. Related to **Figure 3**. (a) Schematic of single-particle analysis and classification. The micrographs of time-resolved and control datasets (top row) were combined for automatic particle-picking. Multiple, step-wise classifications then separated the combined single particles into different classes representing 70S ribosome, the 50S subunit, or bad particles stemmed from noise or contamination on the grid. The

classified particles were then traced back to each dataset to calculate the proportion of 70S ribosomes and 50S subunits (see **Experimental Procedures** – 3D classification). (b-e) The FSC curve for each class of reconstruction: nonrotate (NR) (b), nonrotated with 30S head swivel (NRS) (c), rotated (RT) (d), and 50S subunit (e).

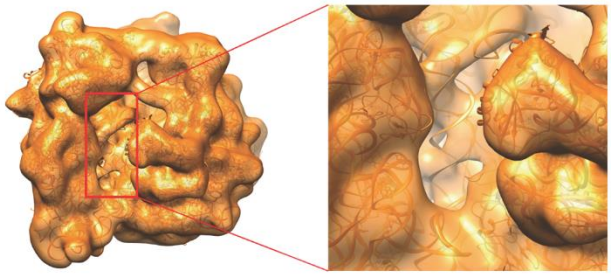

Figure S5. The 3D reconstruction of 70S NR conformation from 5,499 particles in the time-resolved 60 ms dataset. Related to **Figure 4**. Crystallographic structure of 70S ribosome (PDB ID: 2AVY, 2AW4) is rigid-body fitted into the density map for visual aid. The zoom-in image on the right shows a clear density of helix 44 of 30S subunit. Bridges B2a, B3, and B5 are visible in this reconstruction, indicating that these bridges have formed within 60 ms of the ribosome subunit association reaction.

SUPPLEMENTAL TABLES

Table S1. Percentage of 70S ribosome in total 50S-containing particles in each dataset. Related to **Figure 2**.

Percentage (%) [a]	60ms	140 ms	15 minute
50S	66.8 ± 3.4	58.2 ± 2.1	15.3 ± 2.0
70S	33.2 ± 3.4	41.8 ± 2.1	84.8 ± 2.0

[a] The percentage value is shown as average ± standard deviation. Standard deviation is calculated from four runs of RELION 3D classification.

Table S2. Percentage of 70S ribosome in each conformation in total 70S particles in each dataset. Related to **Figure 5**.

Percentage (%) [a]	60 ms	140 ms	15 min
70S NR	61.6 ± 4.1	61.8 ± 5.3	48.0 ± 4.9
70S NRS	27.8 ± 4.5	25.4 ± 5.6	33.1 ± 6.3
70S RT	10.7 ± 0.7	12.8 ± 0.7	18.9 ± 1.6

[a] The percentage value is shown as average ± standard deviation. Standard deviation is calculated from four runs of RELION 3D classification.

SUPPLEMENTAL EXPERIMENTAL PROCEDURES

Kinetic simulation. We simulated the concentration change in the 30S + 50S <=> 70S reaction. The concentration of the 70S ribosome was solved numerically in MATLAB by using $\Delta c(70S) / \Delta t = k_a \times c(30S) \times c(50S) - k_d \times c(70S)$, with an incremental time $\Delta t = 0.5$ ms. We assumed an association rate constant k_a of 13.9 $\mu M^{-1} s^{-1}$, based on previous light-scattering assays (Hennelly et al., 2005), and a dissociation rate constant k_d of 0.002 s^{-1} based on the estimation by Wishnia and coworkers (Wishnia et al., 1975). In the sub-second time range, the dissociation of 70S ribosome is negligible in the kinetic simulation. The simulation starts (t = 0 s) when 1.2 μM 30S and 0.6 μM 50S (both final concentration after mixing) are mixed thoroughly.

Buffers. For ribosome storage, we used Tris-M3.5 buffer (25 mM Tris-HCl, pH 7.6, 60 mM NH_4Cl, 5 mM 2-mercaptoethanol, 3.5 mM $MgCl_2$). For negative staining EM experiments, we used Tris-M10 buffer (25 mM Tris-HCl, pH 7.6, 60 mM NH_4Cl, 5 mM 2-mercaptoethanol, 10 mM $MgCl_2$). For peptide synthesis assay, we used PolyMix-M7 buffer (50 mM Tris acetate, pH 7.0 at 25 °C, 100 mM KCl, 5 mM NH_4OAc, 7 mM $Mg(OAc)_2$, 0.5 mM $Ca(OAc)_2$, 0.1 mM EDTA, 10 mM 2-mercaptoethanol, 5 mM putrescine dihydrochloride, 1 mM spermidine free base). For preparing time-resolved cryo-EM grids, we used HEPES-M12 buffer (20 mM HEPES-KOH, 30 mM NH_4Cl, 5 mM 2-mercaptoethanol, 12 mM $MgCl_2$) to induce spontaneous ribosome subunit association, in the absence of mRNA, initiator tRNA and initiation factors.

Ribosome subunit purification. Ribosome subunits of the tight-coupled 70S ribosomes were purified using sucrose density gradient as describe previously (Fei et al., 2010). Specifically, tight-coupled 70S ribosome from *E. coli* strain MRE600 was isolated

from the rest of the cell components at 7.5 mM Mg^{2+} concentration, and then split to the subunits via dialysis against the buffer containing 1.0 mM Mg^{2+}.

Check for purity of ribosome subunits by negative staining EM. Samples of 30S and 50S subunits each was diluted to 1.2 μM using Tris-M10 buffer, and incubated at 37 ˚C for 15 min, then diluted to 30 nM using Tris-M10 buffer just before application to the EM grid. 5 μL of each specimen was applied on the EM grid for 30 sec, then wicked off by filter paper. 3 μL 2% uranium acetate was then applied to the EM grid for 30 sec, wicked off by filter paper. The staining process was repeated for three times total. The resulting negative staining EM grids were stored at room temperature and examined on the F20 TEM.

Assay of peptide synthesis activity of the associated ribosomes using electrophoretic thin-layer chromatography (eTLC). The polypeptide synthesis assay was performed as previously described (Fei et al., 2010), with minor alterations. Specifically, to test the translation activity of the purified ribosome subunits, we used the f-[^{35}S]Met-Phe-Lys tripeptide assay. The initiation complex mix contained (final concentration of each component in the peptide synthesis reaction, in the order of adding reagents, the same below), in PolyMix-M7 buffer: 0.6 μM IF1, 0.6 μM IF2, 0.6 μM IF3, 1 mM GTP, 0.4 μM 30S (or 50S, or both purified subunits mixed by gentle pipetting, the concentration determined by light absorption at 260 nm), 0.8 μM mRNA (pT7gp32 mRNA coding for Met-Phe-Lys-Glu), and 0.2 μM f-[^{35}S]Met-tRNA^{fMet}. The ternary complex mix contained 8 μM EF-Tu, 1 μM EF-Ts, 1 mM GTP, 0.8 μM Lys-tRNA^{Lys}, 0.8 μM Phe-tRNA^{Phe}. The EF-G mix contained 1 mM GTP, 1.6 μM EF-G. Each peptide synthesis reaction was performed by mixing 2 μL initiation complex with 1.6 μL ternary

complex mix, then with 0.4 μL EF-G mix (or buffer), and incubating at 37 °C for 2 min (unless otherwise indicated), then quenching with 0.5 mM KOH to 160 mM final concentration. The eTLC is performed as previously described (Fei et al., 2010; Youngman et al., 2004). The reactants and products on the resulting eTLC were quantified using the phosphor imager. The peptide formation efficiency (E_{pep}) was calculated by using: $E_{pep} = I_{tripeptide} / (I_{tripeptide} + I_{dipeptide})$, where $I_{dipeptide}$, $I_{tripeptide}$ represents the integrated intensity of the spot on the phosphor image corresponding to f-[^{35}S]Met-Phe, f-[^{35}S]Met-Phe-Lys, respectively. When incubated without EF-G mix, E_{pep} = 10% (1 min) and 13% (2 min); when incubated with EF-G mix, E_{pep} = 81% (1 min) and 82% (2 min).

Assay by puromycin reaction. Furthermore, to compare the translation activity of ribosome subunit mixed in the time-resolved device *vs.* mixed by pipetting, we used the f-[^{35}S]Met-puromycin (Pmn) formation assay. The puromycin reaction reports the total amount of ribosome-bound P-site f-[^{35}S]Met-tRNA^{fMet} that is competent for the peptide transfer reaction. The initiation complex mix contained (final concentration): 0.5 mM GTP, 0.45 μM IF1, 0.45 μM IF2, 0.45 μM IF3, 0.3 μM f-[^{35}S]Met-tRNA^{fMet}, 0.9 μM mRNA, and ribosome subunit mixture (0.39 μM 30S and 0.19 μM 50S, concentration determined by light absorption at 260 nm). The puromycin mix contained 1 mM Pmn. The puromycin reaction was performed by mixing 2 μL initiation complex mix with 2 μL Pmn mix (or buffer, if indicated), and incubating at 37 °C for 1 min, then quenching with 1 M KOH to 330 mM final concentration. The eTLC was performed as previously described (Fei et al., 2010; Youngman et al., 2004). The f-[^{35}S]Met-Pmn formation efficiency (E) was calculated by using: $E = I_{fMet\text{-}Pmn} / (I_{fMet\text{-}Pmn} + I_{fMet})$, where $I_{fMet\text{-}Pmn}$,

I_{fMet} represents the integrated intensity of the spot on the phosphor image corresponding to f-[^{35}S]Met-Pmn, f-[^{35}S]Met, respectively. When mixed in the time-resolved device, E = 8.0%; when mixed by pipetting, E = 8.5%.

Purity and activity of ribosome subunits. We purified the ribosome subunits from *E coli* MRE600 strain using sucrose density gradient ultracentrifugation (**Figure S1a–S1e**). The first and second round of ultracentrifugation used a Tris-polymix buffer system containing 7.5 mM Mg^{2+} to isolate tight-coupled 70S ribosomes. The third and fourth round of ultracentrifugation used a Tris-polymix buffer system containing 1 mM Mg^{2+} to dissociate the tight-coupled 70S ribosomes into their component 30S and 50S subunits. The ribosome profile of the fourth round of sucrose density gradients showed clear separation of the 30S and 50S subunits (**Figure S1d–S1e**). We also performed negative-staining EM on the purified subunits to further confirm their purity. The micrographs of the 30S and 50S subunit fractions showed particles exclusively in the elongated shape (characteristic for the 30S subunit) and in the crown view (characteristic for the 50S subunit), respectively (**Figure S1f–S1G**), confirming that the ribosomal subunits prepared for the time-resolved cryo-EM experiment are indeed pure.

We then tested the translation activity of associated 70S ribosomes formed from the purified ribosomal subunits using a peptide synthesis assay. The results showed that the associated 70S ribosomes are able to convert 81% of radioactively labeled f[^{35}S]Met-tRNA^{fMet} into a tripeptide in the peptide synthesis reaction performed in the presence of elongation factor G (EF-G), compared to only 10% conversion in the absence of EF-G, thereby confirming the high functional activity of the associated 70S ribosomes (**Figure S2a**). Moreover, we also demonstrated that mixing the subunits in the mixing-spraying

device, followed by spraying the resulting 70S ribosomes, does not affect the translation activity of the associated 70S ribosomes, as it is comparable to the translation activity of ribosomes obtained by mixing the subunits *outside* the device by gently pipetting (**Figure S2b**).

Breakdown of reaction time in time-resolved cryo-EM experiment. (1) The reaction time has a finite distribution, which was estimated by fluid dynamic simulation. For the chip having a mean reaction time of 38 ms (calculated by dividing the total volume of the reaction channel by the total flow rate), the most populated reaction time (peak time) is about 27-31 ms. The cumulative fractions of the solution having a reaction time no more than a cut-off time (in parentheses) are: 20% (29 ms), 40% (31 ms), 60% (38 ms), 80% (57 ms). For the chip having a mean reaction time of 107 ms, the peak time is about 67-73 ms. The cumulative fractions of the solution and the cut-off times (in parentheses) are: 20% (69 ms), 40% (76 ms), 60% (88 ms), and 80% (126 ms). (2) Droplets take less than (10 mm / (6 μl/s / 30 μm / 40 μm) =) 2 ms to fly to the EM grid. (3) After the droplets have hit the EM grid, it takes (35 mm / 1.0 m/s =) 35 ms to plunge the EM grid into liquid ethane at 1.0 m/s plunging velocity (calibrated speed of stepping motor) when performing the experiments using the 107 ms chip. It takes 18 ms at 2.0 m/s when using the 60 ms chip. (4) Once grid is immersed in cryogen, freezing takes ~ 0.1 ms (Cyrklaff et al., 1990). Therefore, the total mean reaction time is 107 ms + 2 ms + 35 ms + 0.1 ms ~ 144 ms for the 107 ms chip (i.e., approximately 140 ms), and 38 ms + 2 ms + 18 ms + 0.1 ms ~ 58 ms for the 38 ms chip (approximately 60 ms).

Preparation of control cryo-EM grids using the blotting method. In control experiments, we used the same batch of purified ribosome subunits as used in time-

resolved cryo-EM experiment, and prepared cryo-EM specimens using the standard blotting method. The 30S and 50S subunits were mixed by gentle pipetting at the same concentration as the time-resolved experiment (1.2 μM 30S and 0.6 μM 50S), incubated at 37°C for indicated time (15 min or 75 min), then diluted using HEPES-M12 buffer (or Tris-M10 buffer, if indicated) to about 30 nM 50S concentration within 5 min before preparing the cryo-EM specimens using Vitrobot Mark IV (FEI, Hillsboro, Oregon).

Automatic particle-picking. We kept 2,586 good micrographs for the time-resolved cryo-EM 140 ms dataset, characterized as having visible ribosome particles and round Thon rings extended to about 15-12 Å by visual examination. These good micrographs were comparable in quality with cryo-EM images obtained in the control experiments with the blotting method. We also kept 453, 264, and 1019 good micrographs from the Ctrl 15 min, Ctrl 75 min, and Ctrl 15 min Tris datasets, respectively. We then pooled all the good micrographs from all four experiments together, and used an automatic particle-picking program Autopicker (Langlois et al., 2014) to select a total of 906,896 putative particles (i.e., 50S subunits, 70S ribosomes, ice blobs, and any other particles). 70S ribosome and 50S subunit are both selected by the program because they are similar in size and shape (as compared to the 30S subunit). Using the same parameters as the abovementioned pooled dataset, putative particles were also picked from 816 micrographs of the 60 ms dataset. Although some dimers of 50S:50S and trimers of 50S:30S:30S were observed on the micrographs (see Shaikh et al., 2014 (Shaikh et al., 2014)), they were excluded from downstream processing through control of the selection window size in Autopicker (Langlois et al., 2014).

Initial 3D classification by using RELION. In the first classification to ascertain that the time-resolved method can capture a pre-equilibrium state of the subunit association reaction, we pooled the 140 ms dataset with three control datasets (Ctrl 15 min, Ctrl 75 min, and Ctrl Tris 15 min), classified the dataset computationally using the program RELION (Scheres, 2012; Scheres, 2011), and then traced back each particle to its original dataset. The purpose of pooling the datasets into a single dataset is to classify all the data using the same criterion, so that the proportions of subpopulations in the datasets are comparable. The 50S and 70S particles were traced back to quantify the proportion of 70S in 50S-containing particles and the proportion of each 70S conformation in the total 70S particles in each experiment. However, it is important to note that if the proportion of 70S ribosomes in intermediate conformations is small in the time-resolved 140 ms dataset, pooling it with the three control datasets will further decrease the proportion of such intermediates, resulting in higher risk of missing the discovery of such intermediate conformations. To overcome this shortcoming, we removed two control datasets (Ctrl 75 min and Ctrl Tris 15 min) and included the 60 ms time-resolved dataset to perform the second classification described in the main text.

In the first classification of the combined dataset including 140 ms, 15 min, 75 min and Tris 15 min data, we used the RELION program in a stepwise hierarchical classification to discard bad particles identified by the automatic particle-picking program, to separate the 50S subunit from the 70S ribosome, and to sort out the various conformations of the 70S ribosome. The reference volume for the initial alignment of the total dataset of putative particles was chosen to be a 50S subunit density map (the cryo-EM map of empty 70S ribosome (Valle et al., 2003) with 30S subunit computationally

removed), low-pass filtered to 60 Å. To speed up the classification, we used the particle data in twofold decimated form for classification, and used the data in un-decimated form only in the final steps of 3D reconstruction and refinement.

In step (1), the total dataset (906,896 particles) was separated into 12 classes using RELION 3D classification with a 7.5° angular sampling interval. The classification results were analyzed using a quantitative analysis method (Shen et al., 2014), and the reconstructions from the different classes were examined by using UCSF Chimera (Pettersen et al., 2004) program. The classes resulting in bad reconstructions (i.e., particles fragmented or unrecognizable; 210,848 particles in total) were discarded. The classes yielding a reconstruction of either 70S ribosome or 50S were kept for step (2) of the classification. In step (2), the remaining particles (696,048 particles) were classified into 12 classes. Classes yielding reconstructions of 70S ribosomes (478,383 particles) were separated from the classes yielding 50S subunits (217,665 particles). In step (3), the classes from the second step yielding 70S reconstructions (478,383 particles) were classified into 10 classes, and the classes resulting in bad reconstructions, likely due to remaining unrecognizable particles, were discarded, keeping 272,717 particles of 70S ribosomes. In step (4), the classes from step (2) yielding 50S reconstructions (217,665 particles) were classified into 8 classes, and the classes yielding reconstructions of 50S subunits were kept (97,338 particles). In step (5), the computationally cleaned 70S particles from step (3) (272,717 particles) were pooled together for 3D auto-refinement, to align the particles to a common reference volume of the 70S ribosome from step (2). Then the aligned particles were classified into 12 classes using a 1.8° angular sampling interval. The classes were regrouped based on their resulting reconstructions: non-rotated

70S (NR) (83,877 particles), non-rotated 70S with 30S-head swivel (NRS) (87,169 particles), and rotated 70S (RT) (81,449 particles). In step (6), each class of 70S ribosomes or 50S subunits was refined using 3D auto-refinement with data in un-decimated form. In step (7), the particles were tracked back to each experiment, to quantify the percentage of 70S and the proportion of 70S in each conformation.

The proportions of 70S in 50S-containing particles are: 45% (140 ms), 89% (Ctrl 15 min), 95% (Ctrl 75 min), 86% (Ctrl 15 min Tris). The proportion of 70S ribosomes in the 140 ms data set is much lower than that in the Ctrl 15 min experiment, indicating that the time-resolved 140 ms experiment captured a pre-equilibrium state of the ribosome subunit association reaction. The proportions of 70S in different conformations are omitted to avoid confusion, because they are not directly comparable with those in the second classification combining 60 ms, 140 ms and Ctrl 15 min data.

A comparison of the two control datasets appears to suggest that the proportion of 70S ribosomes increases with longer incubation time, incompatible with our plausible assumption that both Ctrl 15 min and Ctrl 75 min datasets represent the equilibrium state of the subunit association reaction. Although some technical limitations may affect the accuracy of the proportions of 70S particles (see **Strategy for classification**), it is possible that the 70S formation reaction has a slow phase (for some or all the ribosomal subunits) that proceeds even after 15 min incubation at 37°C, since the previous kinetic studies focused on only the first tens of seconds of the reaction (Antoun et al., 2004; Goerisch et al., 1976; Hennelly et al., 2005; Wishnia et al., 1975). Nonetheless, we consider the Ctrl 15 min experiment the equilibrium state of the subunit association

reaction, which has been characterized previously (Antoun et al., 2004; Hennelly et al., 2005).

Technical limitations that may affect the accuracy of estimating the proportions. We note that the accuracy of estimating the proportions may be affected by two technical limitations. First, in the particle selection step, not all the 70S ribosomes and 50S subunits present in a micrograph will be selected by the particle-picking program, because particles that are too close to each other are excluded. Second, in the classification procedure, some otherwise acceptable particles may be incorrectly classified to a class mainly containing unacceptable particles (e.g., ice splotches or some other form of contamination) with an inferior average image (during 2D classification) or an inferior 3D reconstruction (during 3D classification) and consequently discarded before the final 3D reconstruction. Due to such limitations, the attrition rates of acceptable 70S ribosomes and 50S subunits may be different, affecting the calculation of proportions. Nonetheless, these systematic errors affect the population counts at the three time points equally, and they will not interfere with the observation of time dependence.

Estimation of the dissociation constant and the equilibrium concentration of 70S ribosome. Consider the reaction 30S + 50S <=> 70S. The dissociation constant $K_D = k_d / k_a$ = [30S] [50S] / [70S], where k_d and k_a are the dissociation and association rate constants, [x] denotes the equilibrium concentration of x. Assume (1) the measured starting concentrations of the ribosomal subunits are accurate; (2) all subunits are active for the association reaction; (3) K_D is independent on the starting concentrations of ribosome subunits, given the ambient temperature and buffer conditions.

Starting concentrations of the subunits (after mixing, the same below) in the time-resolved experiments without dilution are $c_0(30S)$ = 1.2 μM, $c_0(50S)$ = 0.6 μM. At equilibrium,

$$K_D = [30S]\,[50S] / [70S] \quad (1)$$

$$[50S] + [70S] = c_0(50S) \quad (2)$$

$$[30S] + [70S] = c_0(30S) \quad (3)$$

Starting concentrations of the subunits in the blotting experiments with 20× dilution are $c_{d0}(30S)$ = 0.06 μM, $c_{d0}(50S)$ = 0.03 μM. At equilibrium,

$$K_D = [30S]_d\,[50S]_d / [70S]_d \quad (4)$$

$$[50S]_d + [70S]_d = c_{d0}(50S) \quad (5)$$

$$[30S]_d + [70S]_d = c_{d0}(30S) \quad (6)$$

From the Ctrl 15 min experiment, we observed $[70S]_d / c_{d0}(50S) = 0.85$.

To solve for [70S], we first calculate $K_D = 6.1\times10^{-9}$ M^{-1} using equations (4) – (6).

Second, using equations (1) – (3), we solve for [70S] the quadratic equation:

$$K_D = (c_0(30S) - [70S])\,(c_0(50S) - [70S]) / [70S].$$

Because $0 \le [70S] \le c_0(50S)$, there is a unique analytic solution:

$$[70S] = c_0(50S) \times [(m+1+r) - \mathrm{sqrt}\,((m+1+r)^2 - 4\times m)] / 2,$$

where $m = c_0(30S) / c_0(50S)$, $r = (m - p)\,(1 - p) / p \times c_{d0}(50S) / c_0(50S)$, $p = [70S]_d / c_{d0}(50S)$, and sqrt denotes the square root operation.

The numerical solution is $[70S] = 0.990 \times c_0(50S)$.

Segmentation of the maps. We first performed amplitude-correction by using the EM-bfactor program (Fernández et al., 2008; Rosenthal and Henderson, 2003) and low-pass filtered the reconstruction of each class from step (4) of computational classification,

yielding the "final" maps. We then segmented each final map in UCSF Chimera (Pettersen et al., 2004) with the aid of known crystallographic structures of 70S ribosomes (PDB ID: 2AVY, 2AW4, 2AW7, 2AWB) (Schuwirth et al., 2005).

Measurement of 30S subunit rotation. The difference in rotation of the 30S ribosomal subunit between two different 70S ribosomes was measured in UCSF Chimera using inertial axes (Pettersen et al., 2004). We first fitted the two 70S maps on a common 50S subunit reference map, and then fitted a common crystallographic structure of 30S subunit into each 70S map. We then calculated inertial axes of all the phosphate atoms in the two fitted 30S structures, respectively, and measured the rotation angle between the two inertial axes.

Additional comparison between our results and the previous time-resolved cryo-EM study by Shaikh et al. (2014). The first difference between the results presented here and those reported previously by Shaikh and coworkers is that those authors observed a number of 50S dimers and 50S·30S·30S heterotrimer complexes in their 9.4 ms reaction time data. Although inspection of our micrographs showed some instances of such complexes, we chose to concentrate on 50S and 70S particles only, by setting the parameter in the particle-picking program Autopicker (Langlois et al., 2014) to discard particles bigger than the 70S ribosome.

Second, the proportions of 70S ribosome observed by Shaikh and coworkers are higher than those expected from the kinetic simulation with a k_a of 14 $\mu M^{-1} s^{-1}$ (Shaikh et al., 2014). Specifically, the observed proportions of 70S ribosomes in their experiments were 24.7% at 9.4 ms and 48.7% at 43 ms, compared with 11.6% and 37.5% expected from the kinetic simulation, respectively. In contrast, our observed proportions of 70S

ribosome at 60ms and 140 ms are lower than those expected from the kinetic simulation with a k_a of 13.9 $\mu M^{-1} s^{-1}$ (see **Results – Time course of the subunit association reaction**). Some differences in the experimental conditions may contribute to this discrepancy, such as different activities of the ribosome sample, different ratios of 30S:50S subunits (they used 1:1, we used 2:1 ratio), and the absence or presence of the environmental chamber.

SUPPLEMENTAL REFERENCES

Antoun, A., Pavlov, M.Y., Tenson, T., and Ehrenberg, M. (2004). Ribosome formation from subunits studied by stopped-flow and rayleigh light scattering. Biol. Proced. Online *6*, 35-54.

Cyrklaff, M., Adrian, M., and Dubochet, J. (1990). Evaporation during preparation of unsupported thin vitrified aqueous layers for cryo-electron microscopy. J. Electron. Microsc. Tech. *16*, 351-355.

Fei, J., Wang, J., Sternberg, S.H., MacDougall, D.D., Elvekrog, M.M., Pulukkunat, D.K., Englander, M.T., and Gonzalez Jr, R.L. (2010). Chapter 12 - A highly purified, fluorescently labeled *in vitro* translation system for single-molecule studies of protein synthesis. In Methods Enzymol., G.W. Nils, ed. (Academic Press), pp. 221-259.

Fernández, J.J., Luque, D., Castón, J.R., and Carrascosa, J.L. (2008). Sharpening high resolution information in single particle electron cryomicroscopy. J. Struct. Biol. *164*, 170-175.

Goerisch, H., Goss, D.J., and Parkhurst, L.J. (1976). Kinetics of ribosome dissociation and subunit association studied in a light-scattering stopped-flow apparatus. Biochemistry *15*, 5743-5753.

Hennelly, S.P., Antoun, A., Ehrenberg, M., Gualerzi, C.O., Knight, W., Lodmell, J.S., and Hill, W.E. (2005). A time-resolved investigation of ribosomal subunit association. J. Mol. Biol. *346*, 1243-1258.

Langlois, R., Pallesen, J., Ash, J.T., Nam Ho, D., Rubinstein, J.L., and Frank, J. (2014). Automated particle picking for low-contrast macromolecules in cryo-electron microscopy. J. Struct. Biol. *186*, 1-7.

Pettersen, E.F., Goddard, T.D., Huang, C.C., Couch, G.S., Greenblatt, D.M., Meng, E.C., and Ferrin, T.E. (2004). UCSF Chimera—A visualization system for exploratory research and analysis. J. Comput. Chem. *25*, 1605-1612.

Rosenthal, P.B., and Henderson, R. (2003). Optimal determination of particle orientation, absolute hand, and contrast loss in single-particle electron cryomicroscopy. J. Mol. Biol. *333*, 721-745.

Scheres, S.H. (2012). RELION: implementation of a Bayesian approach to cryo-EM structure determination. J. Struct. Biol. *180*, 519-530.

Scheres, S.H.W. (2011). A Bayesian view on cryo-EM structure determination. J. Mol. Biol. *415*, 406-418.

Schuwirth, B.S., Borovinskaya, M.A., Hau, C.W., Zhang, W., Vila-Sanjurjo, A., Holton, J.M., and Cate, J.H.D. (2005). Structures of the bacterial ribosome at 3.5 Å resolution. Science *310*, 827-834.

Shaikh, T.R., Yassin, A.S., Lu, Z., Barnard, D., Meng, X., Lu, T.-M., Wagenknecht, T., and Agrawal, R.K. (2014). Initial bridges between two ribosomal subunits are formed within 9.4 milliseconds, as studied by time-resolved cryo-EM. Proc. Natl. Acad. Sci. *111*, 9822-9827.

Shen, B., Chen, B., Liao, H., and Frank, J. (2014). Quantitative analysis in iterative classification schemes for cryo-EM applications. In Computational Methods for Three-Dimensional Microscopy Reconstruction, G.T. Herman, and J. Frank, eds. (Birkhauser Basel).

Valle, M., Zavialov, A., Li, W., Stagg, S.M., Sengupta, J., Nielsen, R.C., Nissen, P., Harvey, S.C., Ehrenberg, M., and Frank, J. (2003). Incorporation of aminoacyl-tRNA into the ribosome as seen by cryo-electron microscopy. Nat. Struct. Mol. Biol. *10*, 899-906.

Wishnia, A., Boussert, A., Graffe, M., Dessen, P., and Grunberg-Manago, M. (1975). Kinetics of the reversible association of ribosomal subunits: Stopped-flow studies of the rate law and of the effect of Mg2+. J. Mol. Biol. *93*, 499-515.

Youngman, E.M., Brunelle, J.L., Kochaniak, A.B., and Green, R. (2004). The active site of the ribosome is composed of two layers of conserved nucleotides with distinct roles in peptide bond formation and peptide release. Cell *117*, 589-599.

Chapter 5 Conclusions

My doctoral research studies have focused on the structural characterization of protein biosynthesis using cryo-electron microscopy (EM) and single-particle reconstruction, a method of structure research developed in the Frank lab. With this method one can produce a three-dimensional density map at (near-) atomic resolution, making it possible to analyze the dynamic changes of 'molecular machines', such as ribosomes performing protein synthesis during their functional cycle.

5.1 Ribosome of eukaryotic parasites

A challenge in developing antibiotics effective in combatting human malaria disease is the similarity of the translational machinery between parasite and human hosts. In collaboration with Dr. Jeffery Dvorin at Harvard Medical School, we characterized the structures of *P. falciparum* ribosome complexes at various states of the translation elongation cycle, and revealed dynamical features that differentiate *P. falciparum* ribosomes from those of human host.

I started working on this *P. falciparum* project in 2012 and obtained the first structure of *P. falciparum* ribosome at ~8Å resolution within a year. Thanks to the introduction of the new image recording and processing methods, the applicability and resolution of single-particle cryo-EM have increased dramatically. Our lab stepped with these developments, and benefitted from early acquisition of the new DDD camera, GATAN K2 Summit. As one of the first users of the new camera, I collected another cryo-EM data set in 2013. For image processing, RELION, a quite

powerful 3D classification and high-resolution reconstruction software, was used. RELION is based on a regularized likelihood approach, and classifies images into different homogenous subsets, each of which may be amenable to refinement into reconstruction with higher resolution than the one obtained from the global ensemble. Due to the above advancements, I could subsequently push the resolution from ~8Å to ~4Å, and characterize different ribosome complexes that coexist in the same sample, which reflect various states in the translation process.

In addition to the *P. falciparum* project, I was also actively working on the structural characterization of kinetoplastics parasites ribosomes, *T. cruzi*. In collaboration with Dr. Susan Madison-Antenucci at the Wadsworth Center in Albany, we obtained a 2.5Å resolution map, which enables us to *ab initio* model the r-proteins and rRNA, and even identify ions and water molecules. Together with my colleagues in the Frank lab and Tong lab at Columbia University, we obtained atomic models for each ribosomal subunit as well as the complete atomic model of *T. cruzi* 80S ribosomes, by adopting the X-ray crystallography methods of modeling and refinement methods into cryo-EM.

In the future, our lab intends to continue the collaboration with Dr. Jeffery Dvorin and proceed to study *P. falciparum* gametocytes, the sexual forms of the parasites that form in the blood and are crucial for transmission. Characterization of protein synthesis at this particular stage and its potential vulnerability is particularly important for the development of anti-malarial drugs.

5.2 Time-resolved cryo-EM

The set-up of mixing-spraying method is not easy. A team of people were involved in this project. Bo Chen, a former graduate student at Frank lab, with the help of Zonghuan Lu, David Barnard, and Tanvir Shaikh at Wadsworth Center, Albany, did the initial set-up at Columbia University. Dr. Howard White at Eastern Virginia Medical School provided the computer-controlled plunging device and has collaborated with us on the improvements.

I joined the time-resolved project team in the fall of 2011 and worked together with Bo Chen on the optimization and application of this technique. We made improvements in mainly three aspects, plunging velocity, buffer system, and size distribution of sprayed droplets. Moreover, in collaboration with Dr. Ruben L. Gonzalez at Columbia University, we successfully applied the method to the study of *E. coli* ribosome subunit association (Chapter 4). We were able to capture the subunit association reaction in a pre-equilibrium state, by mixing the subunits and reacting for 60 ms and 140 ms.

This success with the mixing-spraying device invited the design of experiments that explore more challenging biology processes, such as ribosome recycling in protein synthesis, and the development of a more advanced mixing-spraying device that is more convenient, accessible and results in more robust high quality image data.

5.2.1 Mixing-spraying chip manufacture

Our current mixing-spraying chip is made from silicon and glass, designed to withstand high liquid pressure drop in the chip, mainly in the mixing channel. However, manufacturing such chips is not only time-consuming -- usually several weeks -- but also very expensive, on average hundreds of dollars per one chip.

To circumvent this problems, we initiated a collaboration with Dr. Qiao Lin lab at the Department of Mechanical Engineering, Columbia University. Two teams, Xiangsong Feng and Yuan Jia from the Lin lab, Ziao Fu, Sandip Kaledhonkar, Bo Chen and I from the Frank Lab, are working jointly on the development of a new polydimethylsiloxane -- made microfluidic sprayer device. We switched from silicon to polydimethylsiloxane for faster and cheaper manufacture of the chips. Moreover, we designed a new internal-mixing round-jet air blast micro-sprayer. It has been proven to provide more collectable particles per grid (>2000), thinner ice thickness (~490 Å) and result in better image contrast. As proof of concept we recently obtained a ~3Å high-resolution structure of apoferritin using this spraying-plunging method (3). We envision that with all these efforts on further improvement, the mixing-spraying method will become a routine method for time-resolved cryo-EM in the near future.

5.2.2 Time-resolved cryo-EM study of ribosome recycling process

Our first proof-of-principle experiments with the mixing-spraying device invites the design of experiments that explore biological function on the millisecond scale, such as translation initiation and ribosome recycling in the protein synthesis process.

In collaboration with Dr. Mans Ehrenberg's group at Uppsala University, Sweden, we applied this technique to the study *E. coli* ribosome recycling, a process which dissociates the post-termination complexes (post-TC) consisting of mRNA-bound ribosomes bound with deacylated tRNA(s). The separation of the post-TC into subunits is promoted by elongation factor G (EF-G) and ribosome recycling factor (RRF) in a GTP hydrolysis dependent manner. Our collaborators' kinetic experiments (1) have shown that this process occurs in the sub-second time range, which

offered hope that reaction intermediates can be captured by time-resolved cryo-EM, which operates in the same time frame.

We have used time-resolved cryo-EM method to study the ribosome recycling process at three different time point, 60 ms, 140 ms and 560 ms. Combined with the recently developed maximum-likelihood based classification method, we were able to capture several transient structures of an *E. coli* post-termination ribosome on the pathway to splitting into its subunits by *E. coli* RRF and EF-G in the presence of GTP. The present observations of the native form of such complexes demonstrate the strong potential of time-resolved cryo-EM not only for visualizing previously unobservable transient structures but also for precise modeling of the kinetic processes that define their functions. In the near-future, we are hoping characterize the atomic information of each transient states and provide more insights into the mechanisms of protein synthesis.

5.3 Concluding thoughts

In the past five years, the field of single-particle cryo-EM has been experiencing a quantum leap in its applicability and achievable resolution. Indeed, these five years were the time during which I was doing my graduate research in the Frank lab. Our lab has kept in step with the implementation of all the hardware and software advancements: (i) the early acquisition of a new-generation DDD camera, (ii) the maximum-likelihood based classification and refinements software, RELION, (iii) the automated data collection software Leginon, and (iv) the addition of high-performance computing clusters and GPU machines.

More recently, researchers on the NIH campus demonstrated single-particle cryo-EM can (i) go beyond 2Å resolution for a 334 kDa soluble enzyme and (ii) reached near-atomic resolution structures of an enzyme with sizes of 93 kDa (2). I am deeply impressed by the rapid evolution of single-particle cryo-EM. In my opinion, extending achievable resolution of single-particle cryo-

EM to beyond 3Å routinely is one thing we need to work on right now. Incorporation of advanced technology, such as new XP sensor of GATAN K2 Summit camera, and software, such as GPU optimized classification and refinements software, and hybrid modeling methodologies, will all help in the pursuit of higher resolution. Ultimately, the structural information of molecules in their native states at close-to-atomic resolution will greatly facilitate structure-based drug design.

Besides the current need for going smaller, going "larger" could be another attractive way to go in the future. The correlative super-resolution fluorescence light microscopy and cryo-EM technology is an exciting methodology, which can identify structures of larger cellular component complexes *in vivo*, and, notably, without fixation artifacts. I believe that in the future, we might be able to pinpoint the precise location of almost any macromolecule within the cell, as well as resolve its atomic structures.

5.4 References

1. Borg, A., Pavlov, M. and Ehrenberg, M. (2016) Mechanism of fusidic acid inhibition of RRF- and EF-G-dependent splitting of the bacterial post-termination ribosome. *Nucleic Acids Research*, **44**, 3264-3275.

2. Merk, A., Bartesaghi, A., Banerjee, S., Falconieri, V., Rao, P., Davis, M.I., Pragani, R., Boxer, M.B., Earl, Lesley A., Milne, Jacqueline L.S. *et al.* (2016) Breaking Cryo-EM Resolution Barriers to Facilitate Drug Discovery. *Cell*.

3. Fu, Z., Feng, X., Lin, Q. and Frank J., (2016) A microfludic spraying-plunging method for high-resolution single particle cryo-EM (in-preparation)

Vita and Publications

2011	Bachelor of Science, Tsinghua University, Beijing, China
2013	Master of Arts, Columbia University, New York
2014	Master of Philosophy, Columbia University, New York
2016	Doctor of Philosophy, Columbia University, New York

Publications

Sun, M., Li, W., Blomqvist, K., Das, S., Hashem, Y., Dvorin, J. D. and Frank, J. (2015). "Dynamical features of the *Plasmodium falciparum* ribosome during translation." *Nucleic Acids Res*: gkv991, **Featured** on department and lab website

Chen, B., Kaledhonkar, S., **Sun, M.,** Shen, B., Lu, Z., Barnard, D., Lu, T.-M., Gonzalez, R.L., Jr., and Frank, J. (2015). "Structural dynamics of ribosome subunit association studied by mixing-spraying time-solved cryo-EM." *Structure* 23, 1097-1105, **Featured** as a Preview in Structure, 23, 977-978

Guo, Q., Yuan, Y., Xu,Y., Feng, B., Liu, L., Chen, K., **Sun, M**., Yang, Z., Lei, J., and Gao, N. (2011). "Structural basis for the function of a small GTPase RsgA on the 30S ribosomal subunit maturation revealed by cryo-electron microscopy." *Proc Natl Acad Sci U S A*, 108 13100-5

Publications (submitted or in-preparation)

Liu, Z., Wei, J., Vargas, C., **Sun, M.,** Espina, N., Madison-Antenucci, S., Tong, L. and Frank, J. (2016). "Structure and assembly model for the *Trypanosoma cruzi* 60S ribosomal subunit" (submitted)

Washburn, R.S., Hashem, Y., **Sun, M.,** Shen, B., Harvey, S., Frank, J. and Gottesman, M.E., (2016) "NusG and RelA couple and tmRNA uncouples transcription with translation in *E. coli*" (submitted)

Fu, Z., Kaledhonkar, S., Borg, A., **Sun, M.,** Chen, B., Grassucci, R., Ehrenberg, M. and Frank, J. (2016). "Key intermediates in ribosome recycling visualized by time-resolved cryo-electron microscopy" (submitted)

Sun, M., Shen, B., Li, W., Samir, P., Link, A. and Frank, J. (2016). "Cryo-EM study of *S. cerevisiae* ribosomes in response to change in carbon source" (in-preparation)